Electron Capture Dissociation of Peptides Adducted with Transition Metal Ions

CHEN, Xiangfeng

A Thesis submitted in Partial Fulfillment
of the Requirements of the Degree of
Doctor of Philosophy
in
Chemistry

The Chinese University of Hong Kong
June. 2011

ProQuest LLC.
789 East Eisenhower Parkway
P.O. Box 1346
Ann Arbor, MI 48106 - 1346

Thesis/Assessment Committee

Professor C.-F. Steve Au-Yeung (Chair)

Professor T.-W. Dominic Chan (Thesis Supervisor)

Professor S.-L. Lam (Committee Member)

Professor Richard A. J. O'Hair (External Examiner)

Professor Z.-W. Cai (Second External Examiner)

ABSTRACT

In order to improve the performance of the electron capture dissociation (ECD) mass spectrometry for structural analysis of peptides/proteins, ECD of peptides cationized with various transition metal ions was investigated. It was found that peptides adducted with different divalent transition metal ions generated different ECD tandem mass spectra. For Mn^{2+} and Zn^{2+}, the incoming low-energy electron would not favor being trapped by the metal ions and instead trigger the usual ECD dissociation channel(s) via "hot-hydrogen" or "superbase" intermediates to form a series of *c-/z*$^{\bullet}$-fragments. For other first row transition metal ions, including Fe^{2+}, Co^{2+}, Ni^{2+} and Cu^{2+}, reduction of the metal ions occurs preferentially during the electron capture event and lead to the formation of usual "slow-heating" type of fragment ions, i.e. metalated *a-/y-* fragments & metalated *b-/y-* fragments.

To further compare the behavior of metal ions with the same electronic configuration, ECD of Group IIB metal ions adducted peptides were investigated. In contrast to the ECD behavior of Zn^{2+} adducted peptides, peptide radical cations ($M^{+\bullet}$) and fragment ions corresponding to losses of neutral side chain from $M^{+\bullet}$ were observed in the ECD spectra of Hg^{2+} and Cd^{2+} adducted peptides. The experimental observations appeared to depend on the balance of the ionization energy of peptide and the solvation modulated ionization energies of the metal atom. The reduction of divalent metal ions by the electron capture event could induce spontaneous electron transfer from the peptide moiety to the monovalent metal centre and generate hydrogen-deficient $M^{+\bullet}$ species.

As an additional study, effect of tyrosine nitration on the ECD of protonated and metalated peptides was investigated. Some fragment ions that were inhibited in the ECD of protonated peptides were liberated in the ECD of metalated peptides. By theoretical calculation of the cation-π and cation-nitro group coordination using the metal ions nitrated phenol complex as a model, it is found that the metal ions might favor coordinating with the nitro group of the nitrated tyrosine residue in the peptides.

摘 要

爲探究電子捕獲裂解 (ECD) 的機理以提高該技術在分析多肽/蛋白質結構方麵的功能，本文主要研究過渡金屬離子作爲電荷載體對多肽 ECD 產生碎片類型的影響。實驗研究發現不同的二價過渡金屬離子做電荷載體的多肽 ECD 譜圖具有很大的相異性。對於錳(II)和鋅(II)離子作爲電荷載體的多肽，由於該類金屬離子具有半滿或滿殼層的電子結構而不傾嚮於囚禁低能量電子，通過其作爲電荷載體的多肽在電子捕獲后會觸發典型的 ECD 裂解途徑，形成一系列經由「熱氫原子」和/或「超級鹼性」中間體的所產生的c-/z-型碎片離子。對於第一週期的其他過渡金屬離子，包括鐵(II)、鈷(II)、鎳(II)和銅(II)離子，其作爲電荷載體的多肽，在 ECD 中，則有與錳(II)和鋅(II)離子不同的反應，這些金屬離子會優先發生還原反應，囚禁低能電子，釋放能量，從而形成典型的「慢熱」型的碎片離子－含金屬離子的a-/b-/y-型碎片離子。

本文中還研究了擁有相同電子組態的第十二族 (Group IIB) 金屬離子作爲電荷載體的多肽 ECD 實驗反應。實驗發現，與含鋅(II)離子的多肽 ECD 反應相異，使用汞(II)和鎘(II)離子作爲電荷載體的多肽，其 ECD 會產生貧氫肽離子 ($M^{+\bullet}$) 以及其支鏈斷裂的碎片離子。由此推論出肽的電離能和溶劑配位后金屬一級電離能兩者之間的平衡會影響反應行進方嚮。以汞(II)和鎘(II)作爲電荷載體的多肽在 ECD 中會發生電子捕獲誘導電子轉移反應，即：在捕獲低能電子后，配位在多肽上金屬離子首先還原爲一價。然后，由于電離能的差異，電子會自發地由肽分子轉移至一價金屬離子，最終斷裂形成貧氫肽離子 ($M^{+\bullet}$) 和金屬原子。

此外，本文也研究包含硝化酪氨酸殘基的多肽在不同電荷載體(質子和過渡金屬離子)的 ECD 實驗反應。實驗結果顯示，在以質子作爲電荷載體的多肽 ECD 中被抑止的部分碎片離子，在過渡金屬離子作爲電荷載體的多肽 ECD 中會被釋放。採用金屬離子和硝基化苯酚做爲模型，通過理論計算對比苯環配位和硝基配位兩種配位方式，結果錶明金屬離子傾嚮配位與硝化酪氨酸殘基硝基位。

ACKNOWLEDGEMENTS

During the past years, I have benefited tremendously from the guidance, support, encouragement and friendship of many professors and colleagues. I would like to take this opportunity to express my sincere gratitude to them all.

- ✧ I would like to thank my supervisor, Prof. Dominic Chan, for his invaluable advices, guidance and continuous support. I have learned to think critically, systematically and pay more attention to details of a problem. I feel fortunate that I had the opportunity to work with him and I am grateful to him for everything he has taught me;
- ✧ I would like to thank Mr. Chi Chiu Chan and Mr. Ka Fai Woo, for their assistance in rendering instrumental services and resolving computer-related problems;
- ✧ I would like to thank my group members and colleagues, including Dr. Eva Yi Man Fung, Dr. Kelly Wai Yi Chan, Ms. Fan Chen, Ms. Joyce Pui Shuen Wong, Ms. Hoi Sze Yeung, Mr. Gang Li and Mr. Guoqiang Liu. Thanks for all your friendship and help;
- ✧ I would like to thank my wife and parents for their continuous support. My wife Ding Ning always inspires me to conquer difficulties I have met in my studies and in my life. This dissertation is dedicated to them.
- ✧ I am grateful to the Research Grants Council of the Hong Kong Special Administrative Region, China (No. 400209) and the University Postgraduate Studentship from Graduate School, for their financial support.

TABLE OF CONTENTS

LIST OF TABLES

LIST OF FIGURES

LIST OF SCHEMES

SYMBOLS AND ABBREVIATIONS

AI-ECD	Activated ion electron capture dissociation
B	Magnetic field strength
B3LYP	Becke-3-Lee Yang-Parr
CI	Chemical ionization
CID	Collision induced dissociation
DFT	Density functional theory
EA	Electron affinity
ECD	Electron capture dissociation
EI	Electron impact ionization
ESI	Electrospray ionization
ETD	Electron transfer dissociation
FAB	Fast atom bombardment
FTICR	Fourier transform ion cyclotron resonance
FD	Field desorption
HA	Hydrogen affinity
HECD	Hot electron capture dissociation
HPLC	High performance liquid chromatography
ICR	Ion cyclotron resonrance
IRMPD	Infrared multiphoton dissociation
MALDI	Matrix-assisted laser desorption ionization
$M^{+\bullet}$	Peptide radical cation
MIF	Multiple ion filling
m/z	Mass to charge ratio
PA	Proton affinity
PTM	Post-translational modifications
SID	Surface induced dissociation
SORI	Sustained off-resonance irradiation
TS	Transition state

Dedication

To

My Family

Chapter 1

Introduction

1.1 Background

To explore the functions of peptides/proteins, it is very important to know their structural features [1]. The primary (amino acid sequence), secondary (local three-dimensional form), tertiary (full three-dimensional shape) and quaternary (arrangement of multiple folded proteins to form a complete unit) structures of proteins all need to be characterized. The first step is to determine the primary structure, i.e. the amino acid sequence of the peptides/proteins. There are several methods to sequence the peptides/proteins [2-5]. Edman degradation [6-8] reaction and mass spectrometry (MS) [9-11] are the two major methods of direct protein sequencing. The Edman degradation is the classical method of protein sequencing. It proceeds from the N-terminus of the proteins. After the protein reacts with Edman's reagent (phenylisothiocyanate), the first amino acid is cleaved off via the use of trifluoroacetic acid and the resultant amino acid derivative is extracted and treated with acid for chromatography analysis. The new amino acid terminus is left for the next degradation cycle and is identified by repeating the reaction procedure. In some modified Edman degradation procedures, the chromatographic analysis was replaced by mass spectrometry to measure the mass of the cleaved amino acid, or the mass of the remaining underivatized peptide. However, the Edman degradation has several limitations. It will not work if the N-terminal amino acid has been chemically modified, via for example N-acetylate and N-formylate, or if N-terminal amino acid is concealed within the body of the protein. Moreover, it poses a significant problem for the identification and characterization of peptides with post translational modifications (PTMs). Another major drawback of Edman

degradation is the limited applicability to the peptides/proteins at low concentration. In addition, the sample must be purified for Edman degradation and the size of protein should be no longer than 50~70 amino acid residue due to the efficiency (~98%) of each cycle. Thus, given these limitations, Edman degradation is not the preferred method for protein sequencing in modern proteomic approaches.

Compared to Edman degradation, MS based approaches overcome these limitations and have been established as the preferred techniques for primary structural analysis of peptides/proteins [12-14]. A feature of MS based method is high sensitivity, wide dynamic range, high mass accuracy and high sample throughput. In addition, MS is able to analyze complex protein mixtures and identify PTMs. There are mainly three MS based strategies for sequencing of peptides/proteins, the top-down (analysis of intact proteins), middle-down (analysis of larger polypeptides, >3000 Da) and bottom-up (analysis of small polypeptides) strategies [15]. For Top-down MS [16-18], the proteins mixture is either directly infused statically by electrospray (ESI) into the mass spectrometer, or further fractionated by on-line liquid chromatography (LC) followed by ESI. After measuring the accurate mass of the intact protein, tandem MS is then performed in a targeted protein and data is then analyzed manually or with some specialized software. The middle-down MS [19] requires the proteolysis of proteins with enzymes that target less abundant amino acids than trypsin, such as GluC or AspN, before a similar path as top-down MS is taken. For bottom-up MS [20-22], the large proteins are first proteolysis or digested into small peptides, and then the peptide mixture is fractionated by liquid separation techniques, subjected to tandem MS analysis. Finally, the information obtained from the spectra is submitted to the internet or library searching software for peptide identification and protein mapping. The bottom-up strategy offers several advantages compared to the top-down strategy. For example, the efficiency of fragmentation in tandem MS of peptides is usually higher than that of intact proteins, and mass spectrometers are more sensitive in the detection

of smaller peptides. It is important to note that comparing sequences derived from MS/MS spectra with protein databases only works for known proteins. *De novo* sequencing requires compete coverage of sequence ions of all tryptic peptides.

Beside the two methods, the sequence of proteins can also be generated from the DNA or mRNA sequence encoding the protein, if this is known [23]. However, it is necessary to take into account the possibility of amino acids being removed after the mRNA has been translated.

1.2 Mass spectrometry

In the past decades, mass spectrometry based techniques have established an important role in biological research. In the following section, MS including ionization methods and tandem MS will be introduced. Electrospray ionization (ESI) and electron capture dissociation (ECD), will be described in detail as most of the work in this thesis were performed using these two techniques.

1.2.1 Ionization

Ionization of analytes, a prerequisite for MS analysis, is a crucial factor for the application of MS based techniques. Several ionization methods have been developed to generate the molecular ions from solid, liquid, or gas phase samples. In the early years of MS, molecular ions were produced by electron impact (EI) [24] and chemical ionization (CI) [25]. EI and CI are gas phase processes, and the main drawback of these ionization methods is that only volatile, low molecular weight molecules can be generated. Molecular ions of thermally unstable molecules, such as most of the peptides/proteins, cannot be produced using these ionization methods. In the early 1980s of last century, with the development of fast-atom bombardment (FAB) [26], field desorption (FD) [27] and plasma desorption (PD) ionization [28] technologies allowed the ionization of large biomolecules becomes realized. For example, with FAB,

alkaline metal-peptide complexes were generated by bombarding the FAB probe chip coated with a mixture of metal salts, peptide and matrix [29]. However, a drawback of these ionization methods is that they mainly produce primary singly charged ions and are thus limited to biomolecules with molecular weight less than 10,000 Dalton. The real breakthrough in biological MS was the inventions of matrix-assisted laser desorption/ionization (MALDI) [30] and ESI [31,32] in the late 1980s of last century. Nowadays, most gas phase studies related to bimolecular complexes are based on one of these two ionization methods. For MALDI, the sample is first mixed with the matrix, and then desorbed and ionized from the dry crystalline sample by laser pulse irradiation. MALDI usually produces singly charged ions. Recently study indicated that multiply charged ions can be selectively produced by atmospheric (AP) using standard MALDI conditions of laser fluence and reflective geometry [33]. Metal ion-bound peptide ions have also been produced previously by MALDI through doping a certain amount of metal salt solution in the peptide/matrix solution in the sample preparation.

Nowadays, ESI is the most prevailing ionization technique in MS of biomolecules. The coupling of ESI to MS was first pioneered by Fenn and coworkers in 1984 [31]. In contrast to MALDI, which operates in a pulse mode, ESI produces ions in continuous mode via spraying the sample solution through a capillary kept at typically 1-3 kV. In a typical ESI experiment, the sample solution is introduced into the electronpray ion source through a hypodermic needle connected to a syringe pump. The performance of ESI can be improved by tuning the flow rate of syringe pump and the voltage between the capillary and electrode, and sometimes using a coaxial gas flow (e.g. N_2) to facilitate the nebulization process. There are two mechanistic models of ESI, the "charge residue model" [34] and "ion evaporation model" [35]. Based on the "charge residue model", the sample ions are formed through gradual solvation evaporation and Coulombic explosions. While in the "ion evaporation model", the ions are proposed to

be directly ejected from the charged droplets.

ESI has several advantages as compared with other ionization methods. The most prominent one is its ability to handle large samples without mass range limitation. Another advantage is that since ESI usually produces ions with a mixed (multiple) charge states, it lowers the m/z range demands of detecting high-mass bimolecules. Moreover, multiply charging of analytes facilitates the gas phase study of electron capture and electron transfer reactions via MS based methods. As a "soft" ionization process, ESI enables non-covalently bound biomolecular species to be ionized intactly. The sensitivity of ESI is higher than other ionization methods, and therefore can be useful in accurate quantitative and qualitative analysis. Finally, ESI is able to couple with liquid chromatography, thus facilitating the rapid and thorough investigation of biomolecular mixtures.

1.2.2 Tandem mass spectrometry

To obtain additional structural information after ionization of the peptides/proteins, tandem MS technology is required. Generally, in tandem MS, the ions of interest are isolated by mass selection, followed by its activation to dissociation and finally the fragments are detected. For peptides/proteins, tandem MS usually gives the primary structural information in the form of fragment ion series, that is the amino acid residue composition of the sequences.

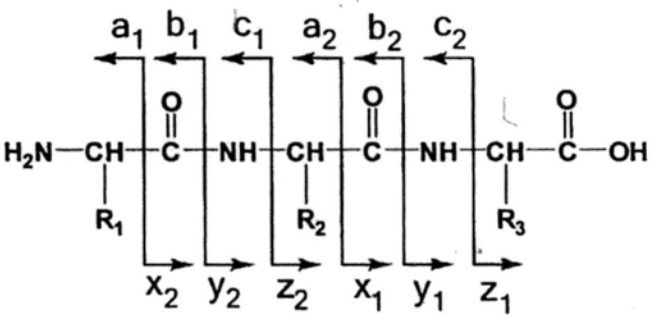

Scheme 1.1

The nomenclature for peptides/proteins sequence ions is shown in scheme 1.1

[36,37]. The sequence ion notation used in this thesis are based on this nomenclature with a slightly adaption, which will be described in the following chapters. There are several methods to activate ions of interest in tandem MS experiments [38-63]. Based on the mode of activation, these methods can be mainly divided into "vibrational excitation based activation" and "electron –ion reaction based activation".

1.2.2.1 Vibrational excitation based ion activation

Collision induced dissociation (CID) [38,39], infrared multiphoton dissociation (IRMPD) [40], blackbody infrared radiative dissociation (BIRD) [41], and surface induced dissociation (SID) [42] are catalogued as vibrational excited based activation method. For these methods, the adsorbed energy redistributes over all the degrees of freedom of the molecular ions and the fragments from these "slow-heating" techniques are formed via the lowest energy dissociation pathways. There are several common features of activation methods based on vibrational excition for peptides/proteins sequencing. First, they have high dissociation efficiency; secondly, the amino acid sequence and composition has strong effect on the fragmentation pattern; thirdly, these excitation methods often lead to low sequence coverage information, loss of small neutral molecules and labile PTM(s). For peptides, in the absence of post translational modification (PTM), the weakest bond is the C-N peptide bond. "Slow-heating" techniques result in the formation of *b*-/*y*-type fragment ions. For peptides with PTM, "slow-heating" techniques usually result in cleavage of part of the posttranslational modified amino acid residue. For example in phosphorylation, HPO_3 and H_3PO_4 often lost [43]. In addition, selective/enhanced cleavages of the amide linkage at the C(O)-N bond C-terminal to an acidic residue (e.g., at Asp-Xxx), or at the C(O)-N bond N-terminal to a proline residue have been observed [44].

In SID, the precursor ions are made to collide with a surface and the ionic products scattered from the surface are mass analyzed. In IRMPD, an infrared laser is

directed through a window into the analyzer cell. Then, the trapped ions absorb multiple infrared photons before dissociation occurs. IRMPD is one of the most often used dissociation method in Fourier transfer ion cyclotron resonance mass spectrometry (FT-ICR MS). The BIRD method is very similar to the IRMPD except that the source of radiation is black body radiation rather than the laser.

CID is the most commonly used and important ion activation method in tandem MS. It was first demonstrated in 1968 [38]. During CID, the precursor ions are activated by inelastic collisions with neutral gas molecules, such as Argon. The translational energy of the ion is coverted into internal energy, then randomizes among all the degree of freedoms. If the adsorbed energy exceeds the threshold energy, the weakest bond would cleave preferentially. According to the power of excitation, CID methods have been classified into high energy CID (keV range) and low energy CID (tens of eV range) [45]. In FTMS, according to the frequency of excited waveforms, the CID methods are classified into on-resonance CID (up to keV range) and sustained off resonance irradiation (SORI-CID) (tens of eV range) [46]. In SORI-CID, during the fragmentation process, an excitation frequency which is slightly off-resonrance from the precursor ion's cyclotron frequency is applied. The alternately excited and de-excited results in an alternating increase and decrease in ion cyclotron radius as precursor ions collide with inert gas molecules that was pulsed into the cell.

With regarding to the mechanisms of vibrational excitation induced cleavage, there are several models including the "amino-O" pathway [47-48], "diketopiperazine" pathway [49-51], "oxazolone" pathway [52-54] and "aziridinone" pathway [49] to produce b and y sequence ions. For CID of peptides/proteins, the "mobile proton model" is widely accepted to explain the fragmentation patterns. In this model, it is proposed that the migration of proton along the amide backbone facilitates induce the cleavages of C-N linkages [55]. It is important to note that not all CID and SID methods solely involve vibrational excitation. Several of the radical bases cleavage

reaction observed by Biemann and coworkers were ascribed to the electronic excitation [56]. In addition, Laskin has described the phenomenon of "shattering" to explain fragmentation processes occurring under high energy SID conditions [57].

1.2.2.2 Electron-ion reaction based ion activation

Electron based ion activation methods, including electron capture dissociation (ECD) [58], electron transfer dissociation (ETD) [59], electron induced dissociation (EID) [60,61] and electron detachment dissociation (EDD) [62], are relatively new ion activation methods compared with the conventional vibrational ion activation method. The cleavage sites of the peptides/proteins and thus the fragmentation patterns generated in these ion activation methods are different from those generated in the "slow heating" methods.

Electron capture dissociation (ECD) was firstly demonstrated by McLafferty and coworkers in 1998. It has drawn much attention in the past decade because of its wide application for structural characterization of biomolecules [64-70]. In a typical ECD experiment, the multiply charged peptides/proteins ($[M+nH]^{n+}$, $n \geq 2$) ions that trapped in the ion-cyclotron resonance cell under radical initiated dissociation by irradiating with low-energy electrons. The main product ions are often *c*-/$z^{\bullet}$-type fragment ions for ECD of protonated peptides. Usually, a small amount (<10%) of *a*-/*y*-type fragment ions are also observed in the ECD spectra.

$$[M + nH]^{n+} + e \rightarrow [M + nH]^{(n-1)+\bullet} \rightarrow c\text{-}/z^{\bullet}\text{- Ions (major)} \qquad (1.1)$$

$$\rightarrow a^{\bullet}\text{-}/y\text{- Ions (minor)} \qquad (1.2)$$

In contrast to CID, the amino acid sequence and composition has little effect on the fragmentation pattern of ECD. Generally, ECD exhibits less selective backbone cleavages and yield more extensive sequence information than CID spectra. The major

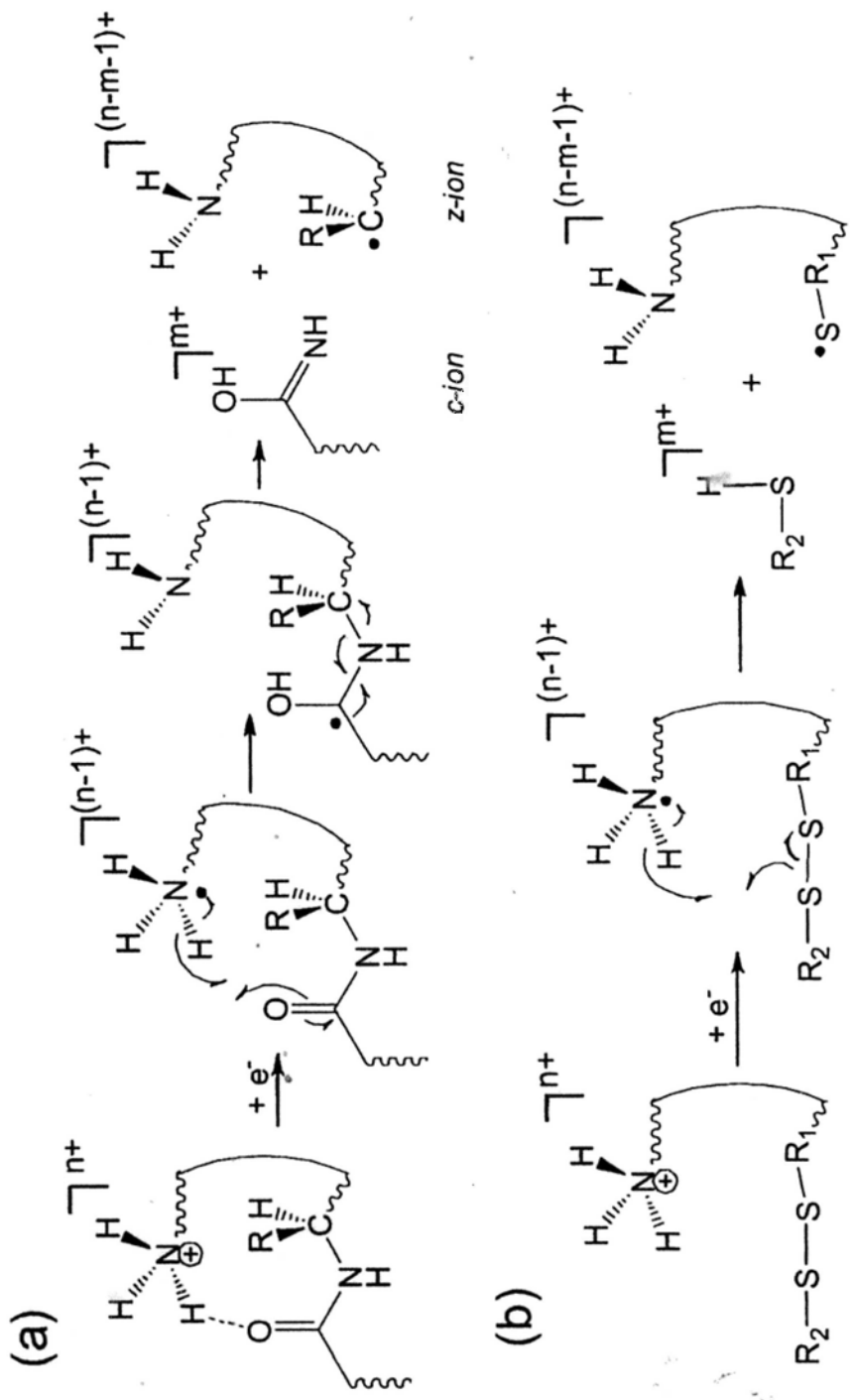

Scheme 1.2

products of ECD for peptide are formed via the cleavages of N-C_α bonds along the peptide backbone [58]. In contrast to the usual "slow-heating" dissociation methods, which cleave the weakest bond firstly, ECD does not affect noncovalent linkages and post-translational modifications (PTMs). In addition, ECD preferentially cleaves the disulfide and thioether bond. As a complimentary tool of conventional MS/MS methods, ECD has been demonstrated for *de Novo* Sequencing, PTMs localization, and tertiary structure analysis of gas phase peptide/proteins [71]. Beside peptides/proteins, ECD has also been used to analysis the structures of nucleic acid, oligosaccharides [72], dendrimers [73], polyester amide oligomers [74], peptide nucleic acids [75], and polyglycols [76].

There are two prevailing mechanistic models for ECD. The earlier model named "hot hydrogen atom" (also named "Cornell mechanism") model [58] was proposed by McLafferty and co-workers. Scheme 1.2 shows the mechanisms of (a) N-C_α bonds and (b) disulfide bond cleavages. In this model, the electron-ion recombination occurs at one of the positively charged sites, leading to the formation of a hypervalent radical species in the ground electronic state. Transfer of a hot hydrogen atom to the backbone carbonyl group generates a labile ketylamino radical intermediate. Decomposition of the ketylamino radical leads to the formation of c-/$z^{\bullet}$- fragment ions. For disulfide bond containing peptides, owing to the higher hydrogen affinity, the hot hydrogen atom would be captured by the disulfide bond and induce the cleavage of S-S bond [77].

The "superbase" model (also named Utah-Washington mechanism) was proposed independently by Simons [78-80] and Turecek [81-83]. A major difference between the two mechanistic models is the "site of capture" of the incoming electrons. Scheme 1.3 shows the mechanisms of N-C_α bonds and disulfide bond cleavages based on this model. In this model, a remote charge increases the electron affinity (EA) of backbone amide π^* orbital through Coulomb interaction. Electron captured by the amide π^* orbital leads

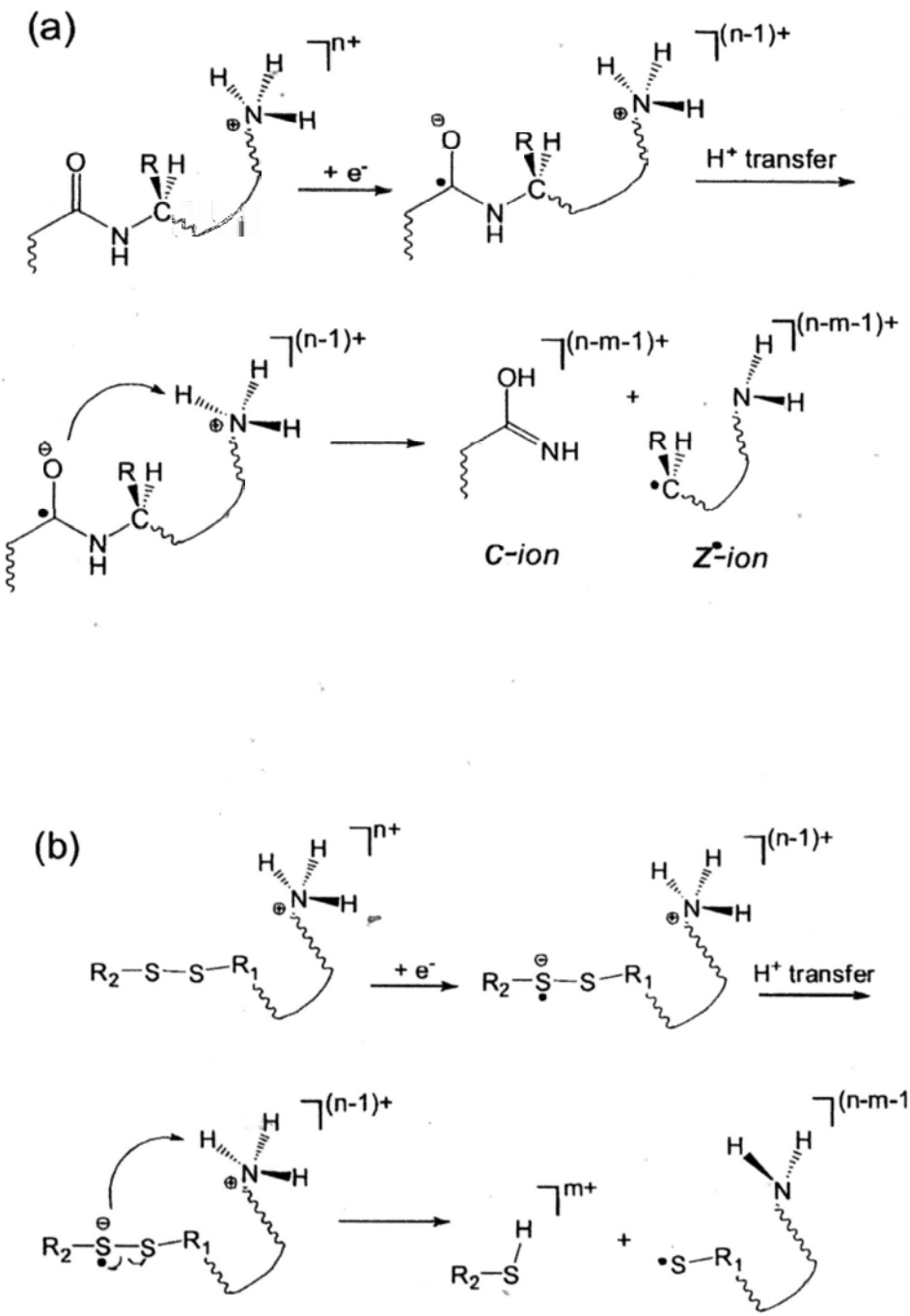

Scheme 1.3

to the formation of localized anionic radical, being a highly basic functional group, the amide anion radical would abstract a proton from the vicinity, (even from protonated arginine) to form the labile ketylamino radical. Decomposition of the ketylamino radical would lead to the backbone N-C_α bonds cleavages.

Similar to ECD, ETD [59] induces fragmentation of peptides/proteins by transferring electron to the positive charged precursor ions. Rather than free electrons, ETD employs radical anions (typically anthracene or azobenzne) as the source of electrons. The electron transfer also leads to the direct generation of *c*-/*z*-type fragment ions. In contrast to ECD and ETD, EDD [62] is applicable to multiply negative charged ions ($\leq 2^-$). In an EDD experiment, the precursor ions are irradiated with higher energy electrons (> 10 eV). An additional electron will be ejected from the precursor ions. The charge reduced precursor ions will undergo dissociation mainly at the C_α-C bond to generate *a*- and *x*-type fragment ions, while the PTM can also be retained in EDD. However, the efficiency of EDD is even lower than that of ECD. In contrast to ECD/ETD and EDD, EID [61] can be used to induce fragmentation in singly protonated or deprotonated analytes. In EID, the singly charged precursor ions are irradiated with high energy electrons (> 10 eV). EID typically results in C-N, N-C_α and sometimes C_α-C cleavages of the peptide.

In addition to the two main ion activation modes, another ion activation mode named laser based electronic excitation via absorption of UV-Vis photons (UVPD) has draw great current interest recently [63]. The control and speed afforded by UVPD has made this method to be unique for application in proteomics.

1.3 Gas phase chemistry of metal ion-biomolecular complexes

It is well known that metal ions play key roles in various biological processes, including oxidation [84], gene regulation [85], and free-radical homeostasis [86]. About one-third of all proteins and enzymes require metal ions as cofactors for biological

function and structural stability [87]. Thus, investigation of metal ion-containing biological systems at the molecular level is of fundamental and applicable importance.

Over the past decades, many techniques have become well-established to study the metal ions-biomolecular complexes in solution or solid phase, including absorption spectrometry, vibrational circular dichroism (VCD) [88], nuclear magnetic resonance spectrometry (NMR) [89] and X-ray crystallography [90]. The major drawback of these methods is that they are hardly suitable for analysis of complex mixtures especially when limited amounts of sample are available. Additional separation and pre-concentration techniques are necessary to purify and enrich the sample before the experiments. As an alternative, gas phase mass spectrometry (MS) based techniques provide a "unique" environment to probe the intrinsic properties of metal ions-biomolecules system. Because of the high sensitivity of mass spectrometry based techniques, disadvantages of solution and solid phase can be overcome. Especially, with the development of tandem MS techniques, abundant structural information can be obtained from small amounts of metal ion-biomolecule complexes.

For the generation of metal ion-biomolecule complexes, beside the direct solid phase based (MALDI) and solution phase based methods (ESI), there are other gas phase approaches: (i) reaction of a metal cation with a neutral biomolecules [91]; (ii) ion-ion reactions between a metal ion or complex and the oppositely charged biomolecule ion [92]. The gas phase chemistry of metal ion-biomolecular species has been widely explored, such as structural analysis of metal ions charged peptides/proteins [93], fatty acids [94], and sugars [95]. Generally, there are three areas to investigate the gas phase chemistry of metal ions peptides/proteins complex. The first area involves probing the intrinsic interactions between metal ions and the peptides/proteins at the molecular level [96]. By understanding of the nature of the metallation of peptides/proteins, it would open the possibility to establish the relationship between metal ions and their biological functions in metalloproteins. For

example, by sequential addition of different metal ions, the enzyme activities of Cu, Zn-superoxide dismutase versus the metalation states has been probed by ESI mass spectrometry [96]. It is important to note that the interactions of metal ions with biomolecules in solution phase are much more complicated because of the various disturbing factors induced by the solvent molecules, such as associations by ion pairing, solvent-metal interactions, intermolecular processes. The conclusions from such studies can be, sometimes, ambiguous and often further studies are required to reconfirm the mechanism. Since gas phase studies are usually involve isolated systems, the perturbations on the structures/conformations of the complexes that prevail in solution phase are eliminated. In other words, gas phase investigations simplify the interactions at play. As a complementary strategy for investigating the metal ion-peptides/proteins interactions, gas phase study of smaller model system that only includes the metal ions and the protein active sites can mimic the structure and function of the active site, and thereby provide mechanistic insights.

The second area involves the use of metal ion as reagents or charge carriers in the ion activation process to provide additional sequence/structural information of peptides/proteins [97-100]. In MS based peptides/proteins sequencing, the usual charge carriers of the peptides/proteins are protons, which mainly locate on the basic functional groups of the amino acid residues. Because the interaction between metal ions and peptides/proteins are generally specific and greatly influenced by the amino acid composition of the metal-binding domains, using metal ions as charge carriers in tandem MS may provide additional structural information of peptides/proteins as compared with the protonated analogues. Take the identification of disulfide bond in peptide as an example; several studies have achieved selective cleavages of the S-S and S-C bond at the disulfide linkages through tandem MS of metal ions complexes of peptides[99, 100].

The third area of gas phase metalated biomolecules is the use of ternary metal ion

complexes to generate radical cations of peptides [101-105]. The investigation of the reactivities of peptide radical cation $M^{+\bullet}$ is fundamentally important for further understanding of the basic biological process induced by protein oxidation. Nowadays, one of the mostly often used methods for the generation of gas phase peptides radical cation is CID of ternary metal-ligand-peptide complex, especially the $[Cu^{II}(L)M]^{2+\bullet}$ (L, ligand and M, peptide). In order to promote the ET reaction pathway in the CID of ternary metal peptide complex and explore the factors that govern the formation of peptide radical cations, various metal ions and auxiliary ligands with different structures were investigated [103,104]. The competitive dissociation channels, including ET, PT and fragmentation, can be controlled and tuned by judicious choice of the auxiliary ligand for ternary metal peptide complex. For example, proton transfer from the ligand to the peptide is suppressed when ligands devoid of acidic hydrogens are employed [103]. Beside the Cu^{2+}-ligand-peptides complexes, O'Hair and coworkers [105] have used the trivalent metal ions (Cr^{3+}, Fe^{3+}, Mn^{3+} and Co^{3+})-ligand-peptide complex to generate peptide radical cations ($M^{+\bullet}$) by using salicylaldehyde (a dianionic ligand) as the auxiliary ligand.

1.4 Dissertation Overview

The research presented in this thesis focuses on the ECD of model peptides adducted with various transition metal ions as charge carriers and its application for PTM identification. Fragmentation pathways and the mechanistic aspect are discussed as well. In this introduction chapter, the basic knowledge of mass spectrometry in peptides/proteins sequencing was described, and subsequently the gas phase chemistry of metal ion-bimolecule complexes. Chapter 2 describes the theory of FTICR-MS used in this study. The experimental conditions and typical experimental procedures for acquisition of tandem mass spectra were also outlined. Chapter 3 compares the ECD behavior of model peptides adducted with first row divalent transition metal ions

(Mn^{2+}, Fe^{2+}, Co^{2+}, Ni^{2+}, Cu^{2+} and Zn^{2+}) and proposes that ECD behavior of metalated peptides is governed by the electron configuration of metal ions. Chapter 4 explores the use of group IIB metal ions (Zn^{2+}, Cd^{2+} and Hg^{2+}) as charge carriers for ECD of peptides and provides the first experimental evidence for metal-ion reduction by the captured electron through the discovery of the electron capture induced spontaneously electron transfer (ECISET) process. Chapter 5 investigates the effects of tyrosine nitration on the ECD of protonated and metalated peptides. In addition, the structural features of peptides with nitrated tyrosine were also investigated by theoretical methods. A summary of the results obtained in the thesis are presented in Chapter 6. The appendix includes pulse programs of the MS and MS/MS experiments.

Chapter 2

Instrumentation, Experimental and Calculations

2.1 Fourier transforms ion cyclotron resonance mass spectrometry

The first Fourier Transforms ion cyclotron resonance mass spectrometer was built by Comisarow and Marshall in 1974 [106]. The used of FTICR-MS in biomolecular research is widespread; this is due to distinct advantages in accuracy and resolution. Using a FT-ICR MS, mass measurements can be done with higher accuracy than with any other mass analyzer, with errors typical at the sub-ppm level. In addition, FT-ICR MS is capable of trapping ions in the cell for a long period of time, thus facilitating the use of ion-molecule/ion-electron reactions for biomolecular structural characterization. There are several common components of FT-ICR MS, including an ultrahigh vacuum system, ionization source, ion transport system, superconducting magnet, an analyzer cell located in the center of the magnetic field, and data acquisition system [107,108]. In the following sections, the basic principle of FT-ICR MS and the experimental conditions and typical experimental procedures for acquisition of tandem mass spectra will be described in detail.

2.1.1 Ion motion in the analyzer cell

In a typical FTICR mass spectrometer, the trapping, manipulating and detecting of ions is achieved in the cell. Figure 2.1 shows a typical ICR cell. It consists of six electrodes that perform different functions. The cell is oriented along the magnetic field so that one opposing pair of electrodes (VP1 and VP2) is orthogonal to the direction of the magnetic field lines and the other two pairs lie parallel to the field lines. An ion with charge q and speed v in the cell experiences the combined force of the magnetic field B and the electrostatic trapping field E. The corresponding force called the Lorentz force

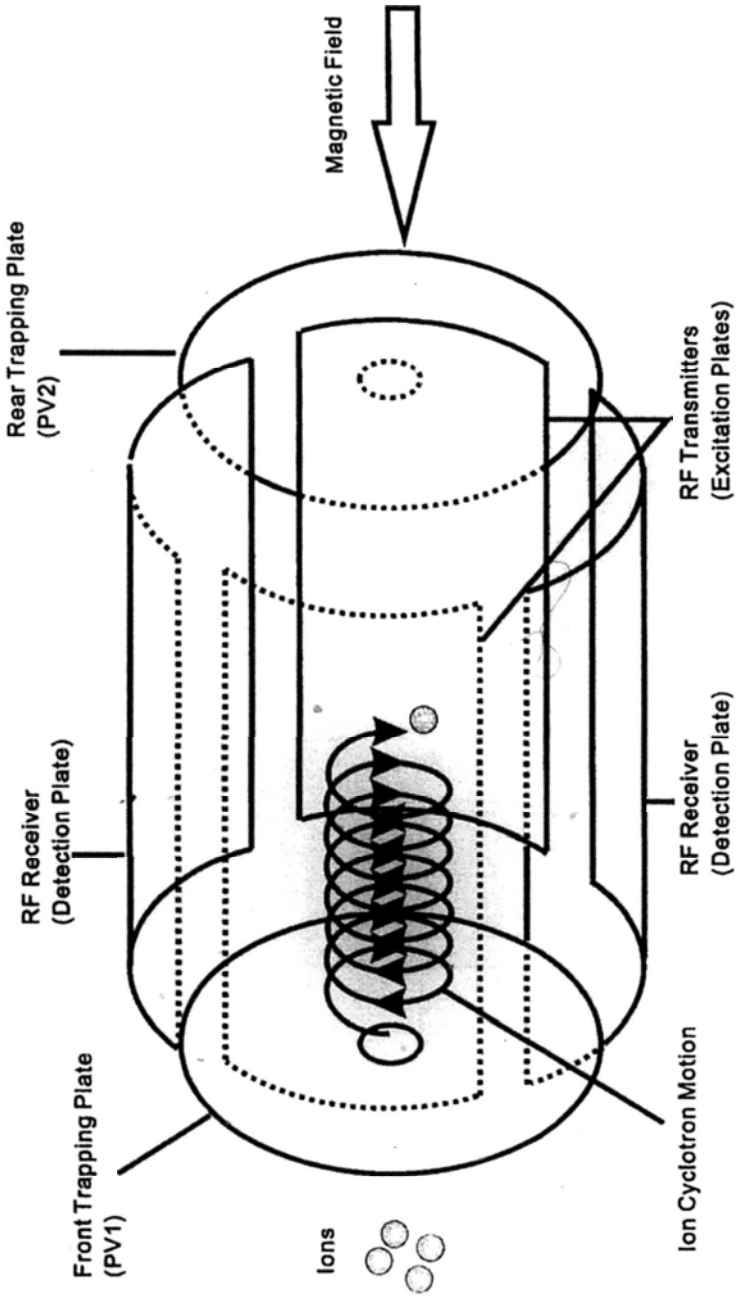

Figure 2.1 A schematic diagram of a typical ICR trapped ion cell

is given by eq. 2.1.

$$\vec{F} = q\vec{E} + q(\vec{v} \otimes \vec{B}) \tag{2.1}$$

The adopted force bends the ions into a circular orbit which is perpendicular to the magnetic field axis. v_{xy} denotes ion velocity of ions in the *xy* plane (perpendicular to the magnetic field axis) and since angular acceleration is v^2_{xy}/r, equation 2.1 can be re-written as:

$$\frac{mv_{xy}^2}{r} = qv_{xy}B \tag{2.2}$$

where m is the mass of the ion and r is the radius of the circular orbit. Considering the high vacuum of system, if there is no collision, the change of speed of the ions is negligible. Hence, the angular velocity is given by:

$$\omega_c = \frac{v_{xy}}{r} = \frac{qB}{m} \tag{2.3}$$

And the cyclotron frequency is:

$$\upsilon = \frac{\omega_c}{2\pi} = \frac{qB}{2\pi m} \tag{2.4}$$

The most important observation is that the cyclotron frequency is independent of the velocity of the ions and thus independent of the kinetic energy of the ions and the cyclotron radius.

Consider the velocity along the magnetic field lines. The potential well generated by the two trapping plates keeps the ions in a harmonic oscillating motion, back and forth, along the z-axis. The trapping frequency, which depends on the trapping potential (V_T), the dimension of the analyzer cell (a), the geometry factor of the cell (α), the mass and the charge of the ions, can be written as:

$$\omega_t = \sqrt{\frac{2qV_T\alpha}{ma^2}} \tag{2.5}$$

The combination of the magnetic and electric fields together introduces the third fundamental motion of ions called magnetron motion. Owing to the nonlinear gradient

of the electric field, the trapping potentials exert a radical force of magnitude ($\frac{qV_T\alpha}{a^2}r$) onto the orbiting ions. The analytical solution of the ion motion is modified from equation 2.1 to equation 2.6 as follows:

$$m\omega^2 r = qB\omega r - q(\frac{V_T r}{a^2}) \tag{2.6}$$

The two solutions of 2.6 are:

$$\omega_R = \omega_+ = \frac{\omega_c}{2} + \sqrt{\left(\frac{\omega_c}{2}\right)^2 - \frac{\omega_T^2}{2}} \tag{2.7}$$

$$\omega_M = \omega_- = \frac{\omega_c}{2} - \sqrt{\left(\frac{\omega_c}{2}\right)^2 - \frac{\omega_T^2}{2}} \tag{2.8}$$

Here, ω_R is the reduced cyclotron frequency, which falls in the range 5 kHz-5 MHz. ω_M is the magnetron motion frequency, which is of the order of 1-100 Hz.

2.1.2 Ion excitation and detection

In FTICR-MS, the mass determination of an ion is based on the relationship between the *m/z* ration of the ion and its cyclotron frequency. However, if the ions move on the cyclotron orbits, the signal corresponding to the ion will not generate on the ICR detection plates, because the radius of the motion is very small and the ions move incoherently. For example, at room temperature, a singly charged ion of mass 10,000u in a magnetic field of 3 tesla, has an ICR orbital radius of only ~0.8mm [108]. To collect the signal of the ions, it is necessary to promote the ion cloud into a larger orbit that is closer to the detection plates in order to induce an imagine current. In addition, the ions must be excited to a coherent motion to obtain a measurable signal which is then is recorded and digitized.

Hence a radio frequency (*rf*) electric field is applied to the ion by adding a sinusoidal voltage to the excitation plates. The ion spirals outwards if its cyclotron frequency is in resonance with the frequency of the applied *rf* electric field. The ions

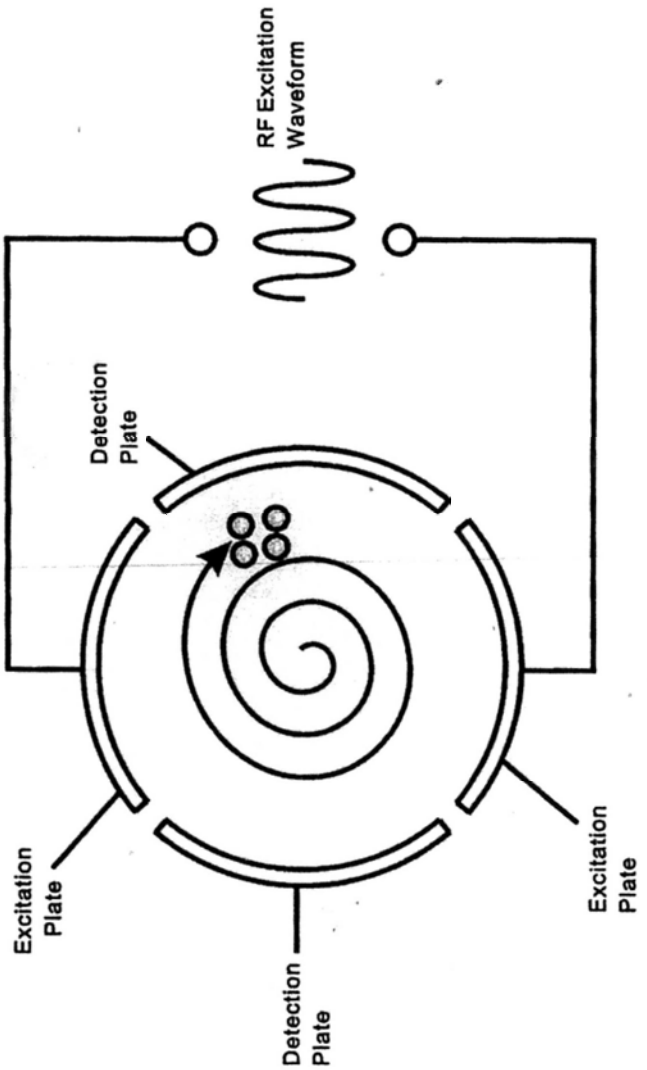

Figure 2.2 A schematic diagram of an ion excited by a radiofrequency (rf) waveform inside an ICR cell.

that do not match the frequency will not absorb energy and remain at the center of the cell. Figure 2.2 shows a schematic diagram of an ion excited by *rf*-waveform inside an ICR cell.

After the excitation pulse, the ions of the same *m/z* ratio are grouped tightly, and undergo cyclotron motion as a package. In the positive mode, as the ions pass the cell's electrodes, the coherently position ion packet attracts electrons to first one and then the other of the two detection plates. The periodic cyclotron motion of the ions produces a sinusoidal imagine signal which can be amplified, digitized, stored and processed. Imagine current detection is non-destructive; therefore the ions remain in the analyzer cell after detection process. The time domain signal will be transformed to the frequency domain by applying a Flourier transform. Then, the frequency spectrum will be converted into a mass spectrum by a calibration using a formula derived from the cyclotron equation.

2.2 The 4.7 Tesla FT-ICR mass spectrometer

All the experiments described in this thesis were performed by using a 4.7 Tesla Fourier-transform ion cyclotron resonance mass spectrometer (APEX III, Bruker Daltonics Inc., Boston, MA). A schematic diagram of the instrument is shown in Figure 2.3. The instrument consists of several main parts, including a 65 mm wide-bore 4.7 Tesla horizontal superconducting magnet, a vacuum system, a homemade nanospray ion source, an electrostatic ion focusing system, an ICR analyzer cell and a standard electrically heated filament electron source. The superconducting magnet was mounted on the floor. In the following sections, the constitution and functions of these integral parts will be described in detail.

2.2.1 Vacuum system

According to the pressure and function, the vacuum assembly can be sub-divided into three parts, including the ion source region, electrostatic ion focusing region and

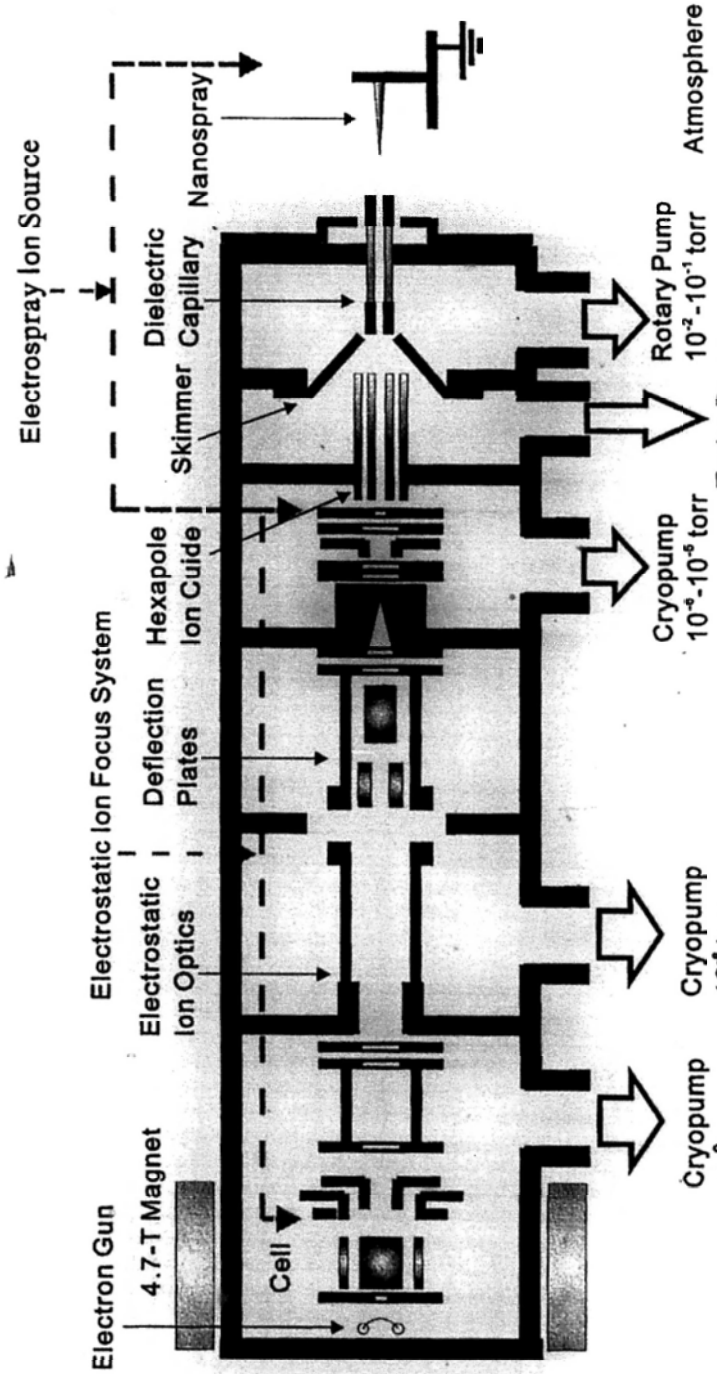

Figure 2.3 A schematic diagram of the Bruker APEX47e FTICR-MS equipped with a homemade nanospray ion source.

ion trapping cell region. Because the mass analysis was performed in the cell region, the ultrahigh vacuum conditions are required to eliminate residual molecules in the cell, thus to minimize the ion-molecule collisions. Since an opening exists in the nanospray source region for ions, a differential pumping system was adopted to achieve and maintain the ultrahigh vacuum condition for the cell region.

At the ion source region, an auxiliary rotary pump (E2M28, Edwards Corporation, UK) and a turbo pump (EXT250HI, Edwards Corporation, UK) were installed. The turbo is backed with the same rotary pump. At the electrostatic ion focusing region, a Coolstar cryopump 800L/min (Edwards Corporation, UK) and a Coolstar cryopump 400L/min (Edwards Corporation, UK) were installed. At the ion trapping cell region, a Coolstar cryopump 800L/min (Edwards Corporation, UK) was installed. All of the cryopumps are controlled by a Cryodrive 3.0 (Edwards Corporation, UK), which is further computer-controlled through the Ricor PLC Communication program.

For all the cryopump, compressed liquid helium used for cool trap was circulated by the cryodrive. The cryodrive was cooled by a refrigerated recirculator (CFT-150, Neslab. US). The temperature of the cold head and hence the vacuum pumping performance of the cryopump were monitored by a hydrogen gas thermometer. Normally, the pressures at the location of the dielectric capillary and the hexapole ion guide are around 10^{-2} to 10^{-1} Torr and 10^{-4} to 10^{-3} Torr, respectively. The pressure at the front of the electrostatic ion focusing region and the rear of the electrostatic ion focusing region were around 10^{-6} to 10^{-5} Torr and 10^{-8} Torr, respectively. At the cell region, the pressure is about 10^{-9} Torr.

To pump down the vacuum system from atmosphere pressure to the working conditions, the opening in front of the capillary in the ion source region was firstly blocked with a small piece of parafilm, and then the whole vacuum system was initially pumped down to 10^{-2} Torr by two rotary pumps. The one directed connect to the ion source region is the auxilliary rotary pump (E2M18, Edwards Corporation, UK). The

other is a roughing rotary pump (E2M28, Edwards Corporation, UK), which is connected to the front of the electrostatic ion focusing region. The turbo pump was turned on when the pressure of the system is lower than 1.0×10^{-2} Torr. When the pressure of the whole system was pumped down to 5.0×10^{-3} Torr, the first cryopump at the electrostatic ion focusing region (Coolstar cryopump 800L/min) was turned on. Finally, when the pressure at the front of the electrostatic ion focusing region fell below 3×10^{-4} Torr, the other two cryopumps were turned on. The pressure of the whole system was continuously pumped down to about 1.0×10^{-9} Torr. It is necessary to regeneration of the whole system when the temperature of the cold head raised to a certain level.

The front and rear part of the electrostatic ion focusing region can be isolated from each other by a mini UHV-Schiebar gate valve (DN50, VAT Vakuumventile AG, Haag). A Vatterfly valve (DN160 Vatterfly Valve Series 20, Vat Vakuumventile AG, Haag) was designed to separate the front Coolstar cryopump and the electrostatic ion focusing region in case of necessary. The valve was used to preserve the vacuum conditions of the ion trapping cell region and the pumping status of the source cryopump when the source is vented for exchange of ion sources or to wash the capillary.

In addition to the two separation valve, a leak valve and an electromagnetic pulse valve were installed near the cell region. The leak valve was usually used to introduce volatile samples into the cell through manually adjusting the nob of the leak valve. The electromagnetic pulse valve (controlled by the console through a TTL pulse) was used for introducing buffer or collision gas, such as argon, into the ICR trapping cell. In order to control the pressure of gas carefully, a small gas cylinder was used for buffer storage before the gas was introduced into the cell.

2.2.2. Nanospray ion source

As shown in Figure 2.4, the spray chamber of commercially available ESI source (Analytical, Bradford, CT, USA) was modified to adopt the home-made

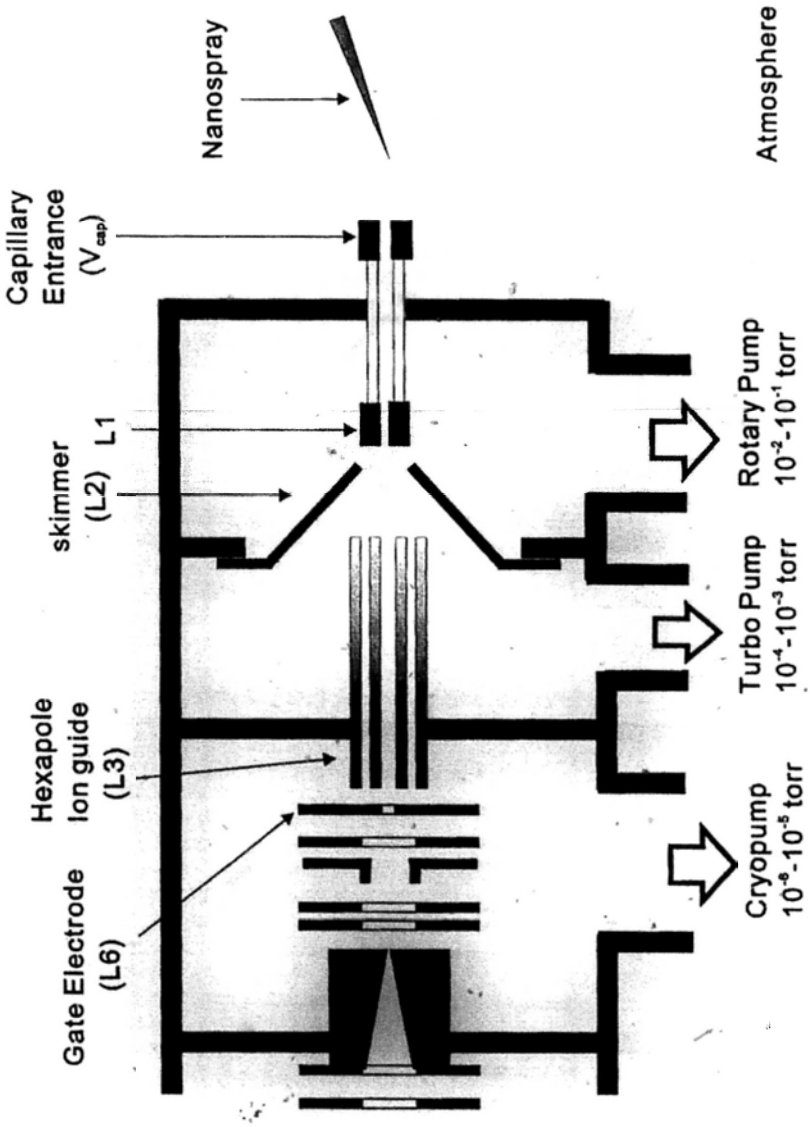

Figure 2.4 A schematic diagram of homemade nanospray source.

nanospray assembly. For generation of ions in the positive mode, the analyte solution was first imported in a homemade glass tip through a syringe. Then the tapered capillary was secured on a platform, which can be adjusted along the x, y and z directions. A platinum wire (∅ =0.3mm) spot-welded with a thin gold-plated tungsten wire (∅=15.0 μm) on the end was placed inside the tapered capillary to establish electrical contact. The platform was parked in front of the opening of dielectric capillary. Finally, applying a negative potential (V_{cap}: ~1000 V) to the dielectric capillary entrance cap, a stable spray of the sample solution could be established. Usually, a flow of heated dry N_2 gas (~275 °C) was used to assist with solvent evaporation from the sprayed droplets.

The dielectric capillary (length=18.0 cm) was made of glass with stainless steel caps in both ends. The gas phase ions generated by nanospray were sampled through the dielectric capillary into the high vacuum part of the mass spectrometer. Beside the entrance electrodes V_{cap}, the end of the capillary acted as the other electrodes (L1). The ion focus optics, including a skimmer (L2), an Iris™ hexapole ion guide (L3) and a gated electrode (L6), was located in the low vacuum region. The orifice of the dielectric capillary and the skimmer were used to restrict the gas flow from the atmospheric region into the vacuum region. The other function of skimmer is to select ions with a given velocity components. The hexapole ion guide was used to trap and accumulate ions prior to extraction. After a fixed period of ion accumulation, the ions were then pulsed into the mass spectrometer. Ion accumulation in a heaxpole ion trap increases the duty cycle and the sensitivity of the mass spectrometer. As shown in Figure 2.4, the region between the capillary and skimmer was pumped to a pressure of about 10^{-2} to 10^{-3} Torr. The region between the skimmer and hexapole ion guide was pumped to a pressure of about 10^{-3} to 10^{-4} Torr. The potential of L1 was typically around 100V. The pressure gradient between the atmospheric region and the capillary skimmer region acts as the driving force for the analyte ions to overcome the potential barrier between L1 and V_{cap}.

In order to enhance the signal intensity, the analyte ions were usually accumulated in the hexapole ion guide for a pre-fixed period of time. A radio frequency voltage (typically 5 MHz, 600 V_{P-P}) kept ions in the radical direction and the potential well created by the skimmer and the gate electrode (L6) did not allow ions to escape from the hexapole ion guide. A pulse of negative potential was applied to the gate electrode when the ions were be extracted into the ion transfer system.

2.2.3 Ion transfer system

The ions extracted from the ion source were transported to the ICR trapping cell by an electrostatic ion transfer system. Figure 2.5 shows a schematic diagram of the different ion optical components together with the typical potential gradient curve. Ion transfer optics provides a focused on-axis ion beam with energy high enough to pass the magnetic field gradient. It was composed of electrostatic lenses (PL1, PL9, FOCL1 and FOCL2) and beam steering electrodes (XDFL, YDFL, PL2/DPL2, PL4/DPL4). The potentials applied to the beam steering electrodes were used to guide the ions into the cell and to deflect the ions away from the ion optical axis.

To increase the ion transmission efficiency, a high potential electrode (HVO, 2.5kV) was used to accelerate ions to a higher velocity. DPL2 and DPL4 are low energy beam steering electrodes; and XDFL and YDFL were used to adjust the trajectory of the high velocity ion beam in the x- and y-direction, respectively. An entrance electrode (EV1) was installed with a pre-set slightly negative potential (for positive-ion operation mode) to attract the decelerated ions into the ICR cell. Behind the EV1, there are two spitted electrodes, EV2 and DEV2. The first one is used to define the center potential at the cell entrance; and the second one controlled the voltage gradient across the cell entrance.

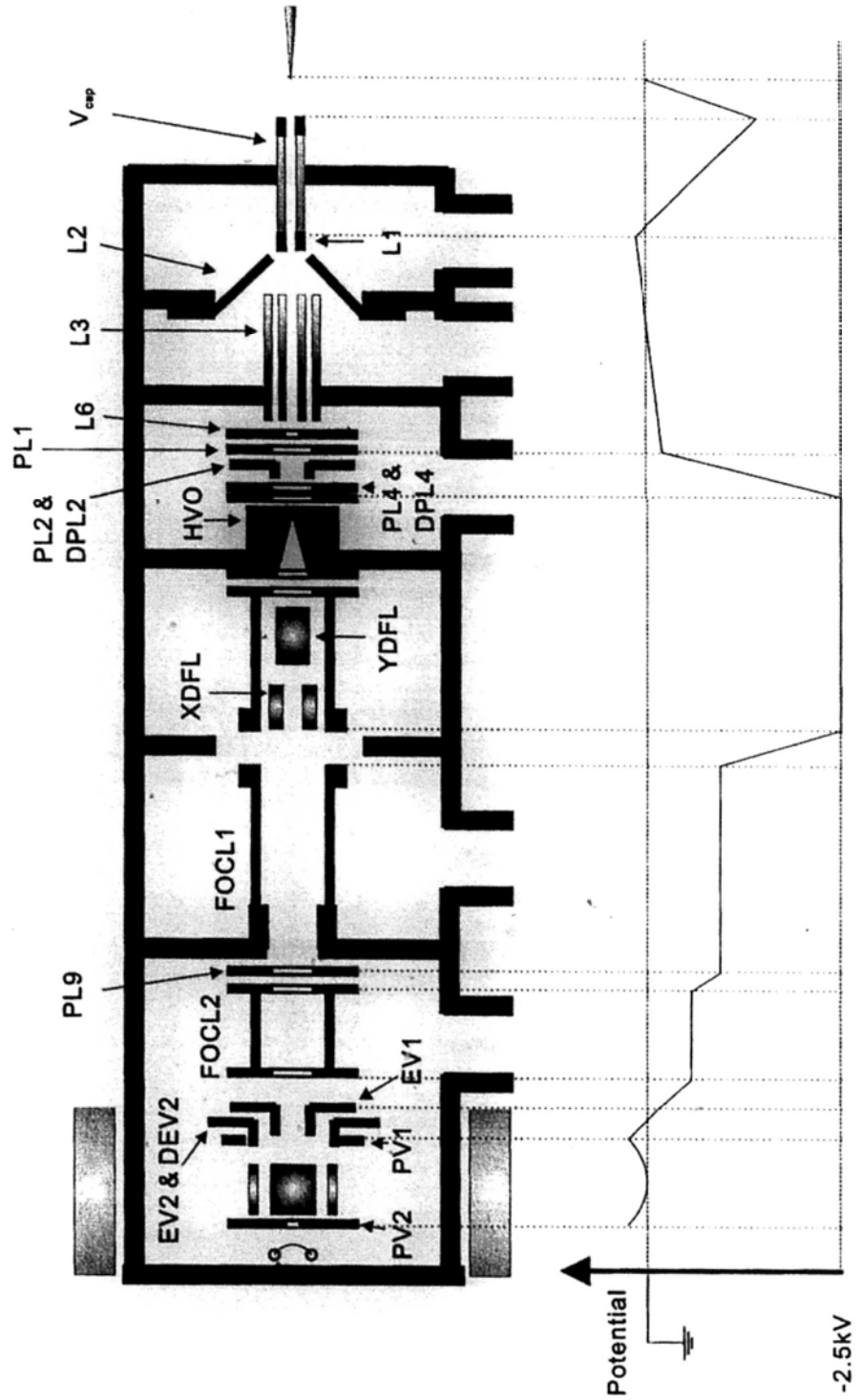

Figure 2.5 A scheme diagram of potential gradient along the ion source, the electrostatic focusing system and the infinity™ cell .

2.2.4 Ion trapping cell and the electron emission source

In this study, the ion trapping cell installed in the 4.7 Tesla FTICR-MS was an Infinity™ Cell [109] (Bruker-spectrospin, Fällanden, Switzerland), which was a cylindrical cell with dimensions of 60 mm in diameter and 60 mm in length. A schematic diagram showing all the cell electrode potentials used throughout the experiment is shown in Figure 2.6. Both ends of the Infinity™ Cell were mounted by circular plates (PV1 and PV2) for ion trapping. A circular aperture of 6.0 mm in diameter was dug at the center of each trapping plate for entrance and exit of ions and/or electrons. The PV2 was also used to quench the cell to eject the residual ions by applying a potential (-10V for positive ions mode). Two pairs of curved electrodes were installed orthogonally with respect to the trapping plates. The shorter pair are the excitation plates that were used to excite the trapping ions by adding *rf*-excitation pulses onto these plates. The remaining pair of electrodes are the detection plates, which were used to generate the imaging current.

A standard electrically heated filament source was installed on the Infinity™ Cell for electron emission. The filament was made of Rhenium ribbon with a width about of 0.5 mm. It was spot-welded onto the metal posts, Pin 1 and Pin 2 with a distance of about 6 mm. The filament position (f_p) was located at a distance of 108 mm from the rear end of the Infinity™ Cell using a home-made adapter flange. A repeller electrode was placed at the back of the filament to provide a repulsive potential for electron ejection into the cell. It was electrically connected to the pin 2. Usually, equal potentials of +13.2 V were applied to the pin 1 and pin 2, thus no filament heat current and electron irradiation occur. When a filament heat current was set for electron generation, different potentials were loaded onto the pin 1 and pin 2 with the potential of pin 1 higher than the potential of pin 2. To repel electrons to the ion trapping cell for ion electron reaction, both the potential of pin 1 and pin 2 were ramped down from positive to negative. Because the potential of pin 2 was lower, the repeller electrode repelled the

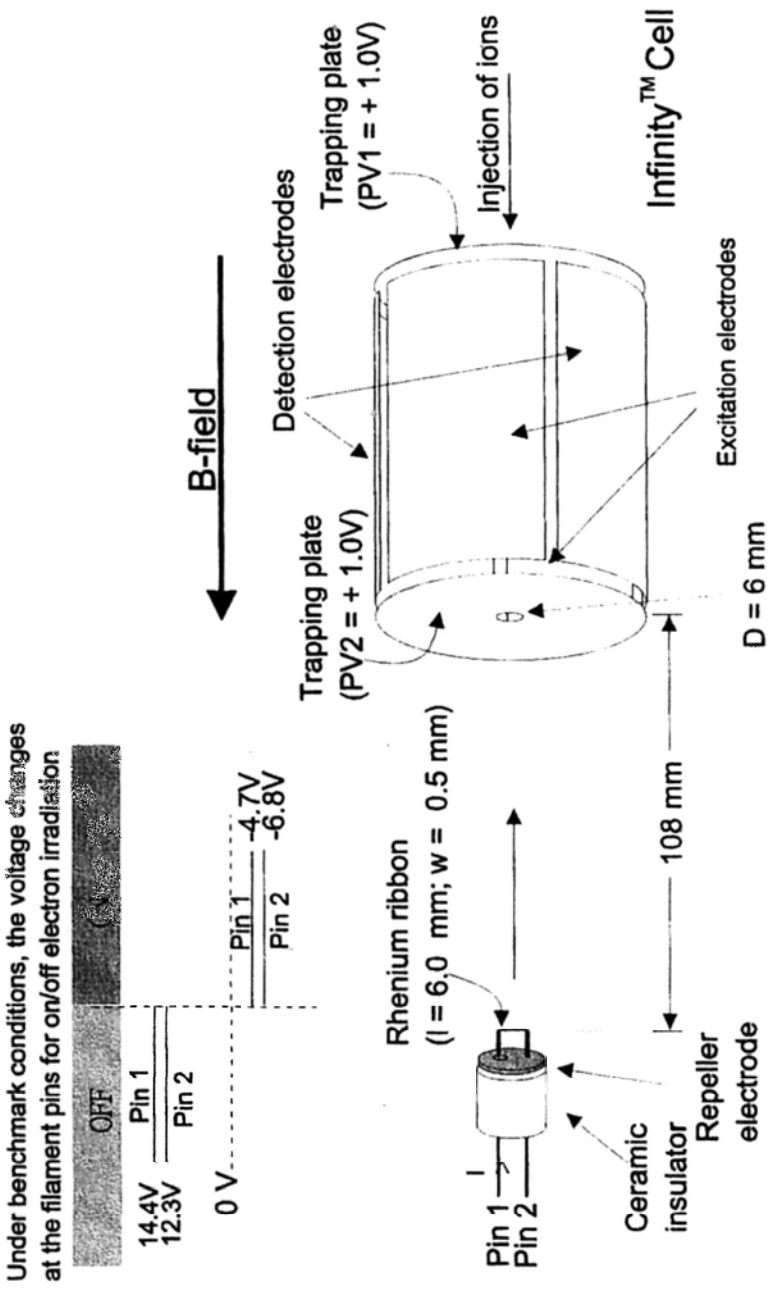

Figure 2.6 A schematic diagram of the heated filament electron source and the ICR trapped ion cell

electrons towards the cell.

2.2.5 Data acquisition system

The console of the 4.7 FTICR-MS used here was connected to a Dell Window-based workstation PWS530 (Dell Computer Corporation, Texas, US). The Dell workstation was equipped with an Inter (R) XEO microprocessor and 32 megabytes (Mb) of base memory and operated under Microsoft Windows 2000 system. The control of the experimental parameters, data acquisition and data manipulation was carried out using the user-interface program XMASS version 6.1.0 (Burker Daltonics, Billerica, US) running on the workstation. For broad-band mode, the free induction decay (FID) signal received was amplified by either FADC 12-bit digitizer; for narrow-band mode, the FID signal is amplified by the SADC 16-bit digitizer. The maximum size of the time-domain signal was 1 Mb. After completion of data acquisition, the FID signal was transferred to the Dell workstation. It was first zero-filled and subsequently converted to frequency-domain signal (mass spectrum) by the Fast Fourier transform (FFT) algorithm and magnitude calculation method.

2.3 Experimental

The MS data acquisition procedure of a FTICR-MS experiment was controlled by a pulse program, which is a sequence of pulses that are sent to operate the different units of the FTICR-MS during the acquisition. In the following sections, the simple ESI, ESI-ECD and ESI-SORI-CID pulse programs will be described in detail.

2.3.1 ESI pulse program

A schematic diagram of sequence events in the pulse program for a simple ESI experiment is shown in Figure 2.7 (for the source code of the pulse program, please refer to Appendix I). Generally, it involves four steps: ion quench, ion accumulation,

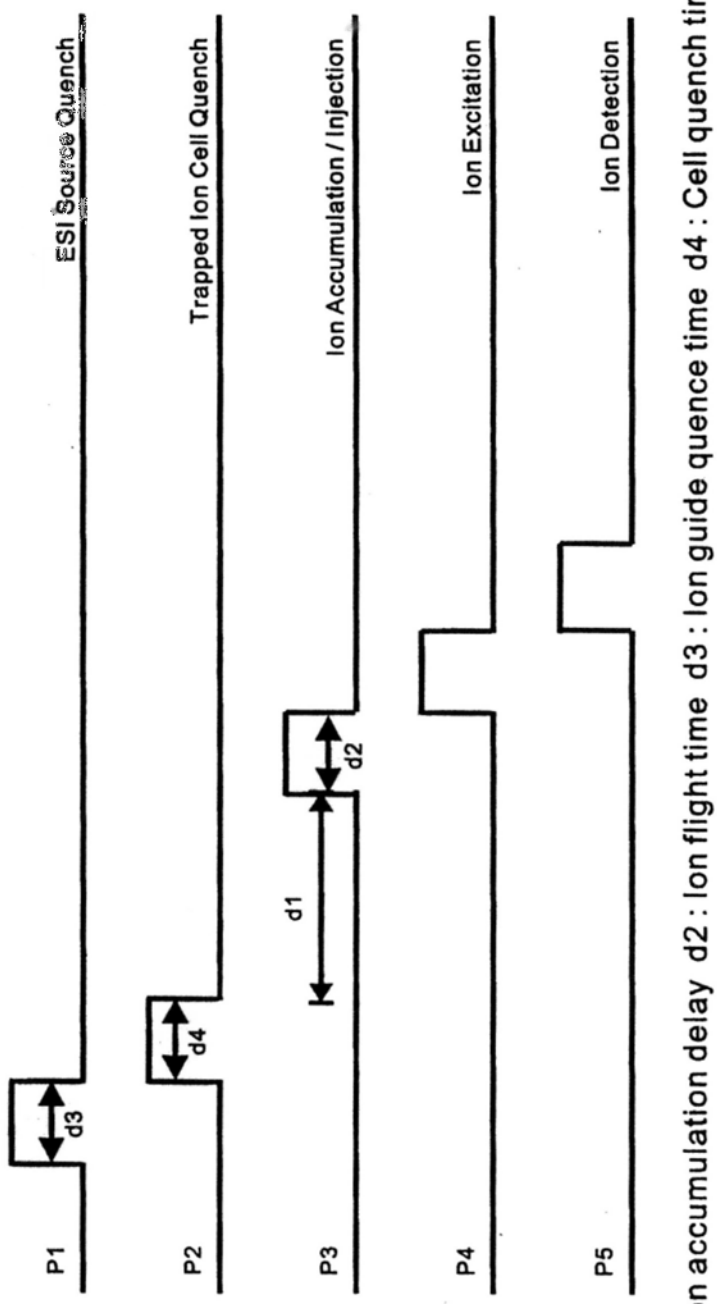

d1 : Ion accumulation delay d2 : Ion flight time d3 : Ion guide quence time d4 : Cell quench time

Figure 2.7 A simple pulse sequence program for ESI FTICR-MS experiments.

ion excitation and ion detection.

The first step for each acquisition cycle is ion quench. There are usually two quench pulses. The first one is source quench, in which a pulse is sent to the voltage control board to change the potential of the gate electrode inside the ESI source to negative voltage for positive ion operation mode and vise versa. Any residue positive ions in the hexapole ion guide were removed. The other one is analyzer cell quench, in which a pulse is sent to the voltage control board to change the potential of the rear trapping plate (PV2) to negative voltage (-10V) for positive ion operation mode and vise versa. Thus, the residual ions inside the trapping ion cell are also removed. After the quench pulses, a short delay is used to restore the potential of the rear trapping electrode (PV2) and gated electrode back to the preset values.

After the short delay, ions generated by the nanospray ionization will accumulate in the hexapole ion for a prefixed time. The ion accumulation in the hexapole also serves to convert the continuous ion flow from the ESI ion source into a pulsed extraction of the ion package. Then, an "ion injection" pulse will be executed to extract the ion package from the hexapole ion guide to the electrostatic ion focusing region. This is realized by adjusting the gate electrode to the preset extraction potential. Then, the direction of ion package in the electrostatic ion focusing region is carefully tuned by adjusting the potentials of deflectors and the entrance electrodes of the cell to maximize the number of ions entering into the cell. After the ions accumulate for a predefined period of time, the deflector voltages are restored to ground voltages and the voltages of the entrance electrodes reset to the same potential as PV1.

After the ion injection event, the ion excitation pulse and ion detection pulse are executed sequentially. During the ion excitation event, a chirp of *rf*-waveform scanning from the cyclotron frequency of the lowest detection mass (highest frequency) to the highest detection mass (lowest frequency) is transmitted through the excitation electrodes of the analyzer cell. Finally, the cyclotron motions of the excited ions are

imaged by the *rf*-receiver plates of the analyzer cell and eventually an FID signal is generated. These pulse sequences are usually repeated for a number of times; and the signals obtained in each scan are summed up to enhance the signal to noise ratio.

To increase the intensity of ions of interest, some of the experiments in this study were performed by using multiple-ion filling (MIF) approach. A detail description of MIF was previously reported [141]. Briefly, the generated ion is directly transferred into the cell within a short-time accumulation in the hexapole ion guide. Then, cooling gas is pulsed into the Cell to "freeze" the ions by removing the excessive z-axial kinetic energy of the ions and preventing substantial loss of trapped ions during the admission of another pulse of ions. The ion injection and cooling gas pulsing is usually repeat for at least 10 times. Figure 2.8 shows the schematic diagram of sequence events in the pulse program for a MIF-ESI experiment.

2.3.2 ESI-ECD and ESI-SORI-CID pulse program

The pulse program of tandem mass spectrometry includes two additional pulses, the ion isolation pulse and ion activation pulse, in between the ion injection and ion excitation events. After the ions entre into the ion trapping cell, the ions of interest is first isolated by an ion selection pulse to ejected unwanted ions through over-excitation. In this pulse, the amplitude, duration and "ejection safety belt" of the *rf*-wave for ion over-excitation is carefully adjusted to minimize the excitation of precursor ions and to maximize the efficiency of ejection unwanted ions.

For the ESI-ECD pulse program, following the ion selection, an electron irradiation pulse is executed. An electron beam is directed into the trapped ion cell to react with the precursor ions for a predefined duration. To maximum the ECD efficiency, the electron flux and electron energy is carefully adjusted by tuning the filament heating current and the average filament bias voltage, respectively. Figure 2.9 shows a typical

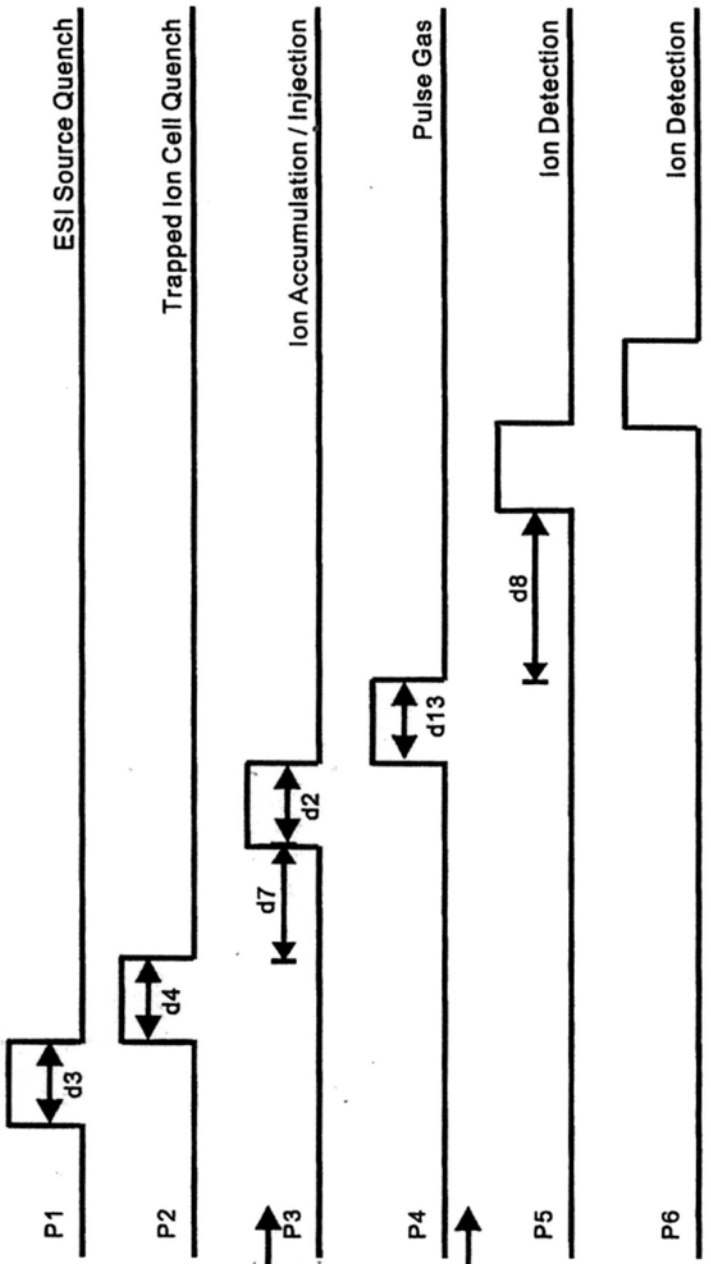

Figure 2.8 The pulse sequence program for MIF-ESI FTICR-MS experiments.

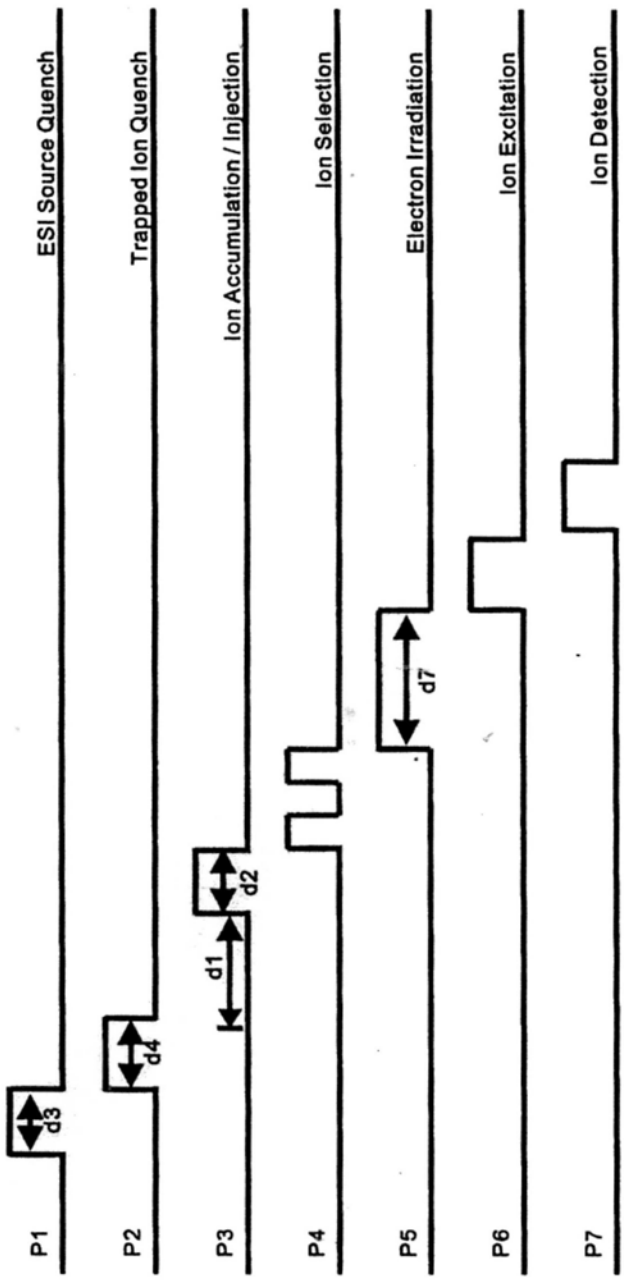

Figure 2.9 A pulse sequence program for ESI-ECD FTICR-MS experiments.

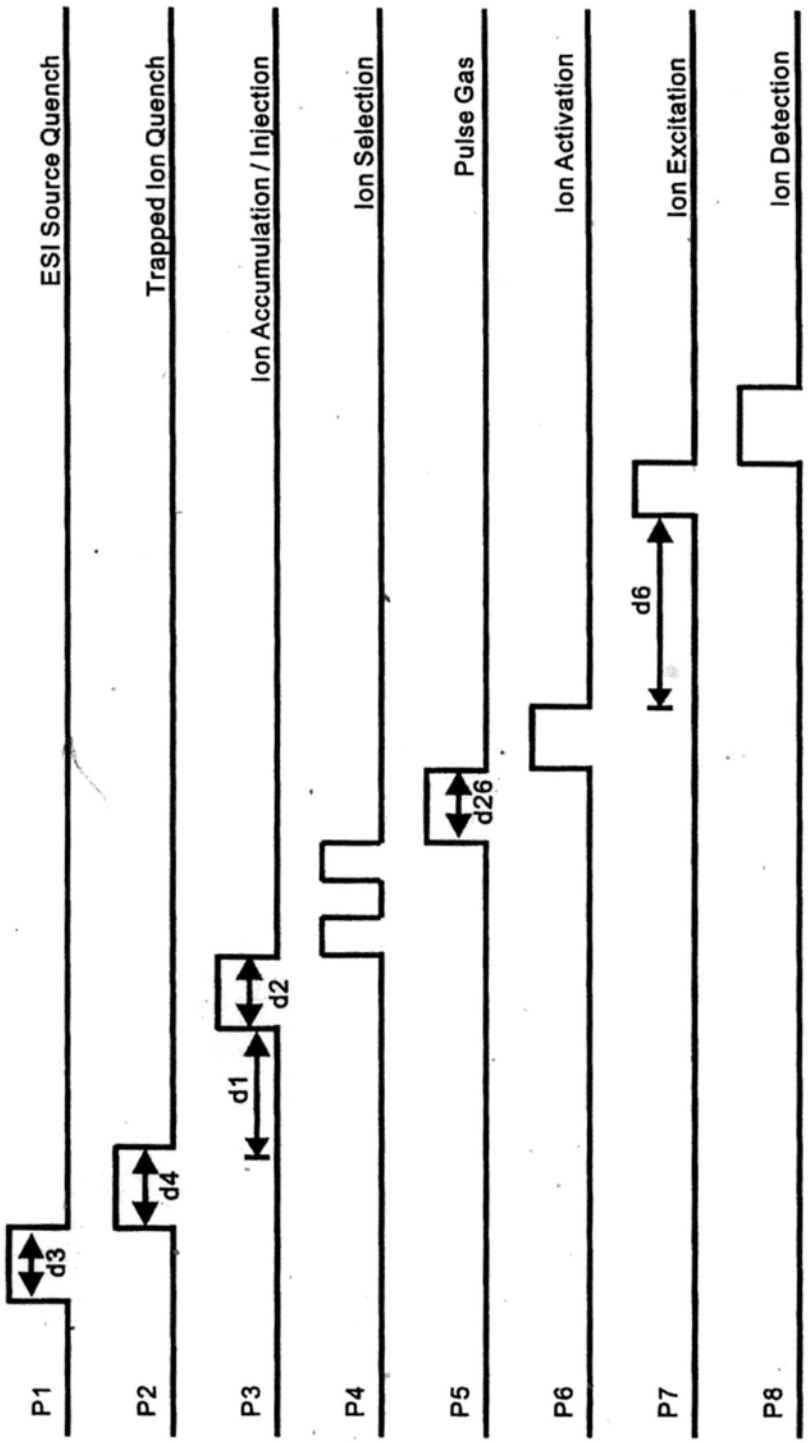

d1: Ion accumulation delay d2: Ion flight time d3: Ion guide quence time
d4 : Cell quench time d6 : Pumping Delay d26: Pulse valve duration

Figure 2.10 A pulse sequence program for ESI-SORI-CID FTICR-MS experiments.

pulse program for ECD experiment. (For the source code of the pulse program, please refer to Appendix II).

For ESI-SORI-CID pulse program, the ion activation process involves two steps: the pulsing of collision gas and ion activation with pumping delay. In the first step, an inert collision gas (argon) is pulsed into the cell region after the ion selection. Usually, the pressure of the high vacuum region will increase to around ~ 3.0×10^{-7} mbar. Then, the ions of interest will be activated by a 500 ms *rf*-waveform with frequency offset of 1,000 Hz relative to the frequency of the selected ions. During the ion activation, the precursor ions will be excited/de-excited and collide efficiently with the collision gas. After this ion activation, a delay of 3.5 seconds is used to pump the pressure within the cell to the base level for the following ion detection event. Figure 2.10 shows the pulse program used for ESI-SORI-CID experiments.

2.4 Theoretical Calculations

2.4.1 Density Functional Theoretical (DFT) calculations

All DFT calculations were performed using the Gaussian 03 molecular orbital package [110]. For the deprotonation reaction induced by the transition metal ions, equilibrium geometries of the truncated model were determined by full optimization followed by harmonic frequency calculations to confirm the nature of minima and transition states. All the stationary points were optimized using the Beck three parameter hybrid (B3LYP) exchange-correlations functional in the framework of the Kohn-Sham density functional theory (DFT) [111-113]. The standard split-valence basis set 6-31++G(d,p) was used for H, C, N and O atoms. All the transition metal cations were described by employing the Hay-Wadt effective core potential (ECP) with LANL2DZ basis set [114-115]. Single point energy calculation were calculated at the B3LYP level in conjunction with LANL2DZ+6-311++G(3df,2p) basis set.

2.4.2 Molecular Mechanics (MM) calculations

The molecular mechanics calculations were performed by using the MacroModel program (v5, Schrodinger Inc., Portland, OR). Generally, energy minimizations of the model systems were performed by the Truncated Newton-Raphson Conjugate Gradient (TNCG) method. The conformational search was conducted using the Monte Carlo [116] method with a random variation of all bonds. Low-energy conformers were found in 5000 steps and structures with energies not higher than 50 kJ/mol of the lowest-energy structures were stored. All structures found in these conformational searches were aligned and the groups of interest containing regions were truncated for further DFT level calculations.

Chapter 3

Electron Capture Dissociation of Peptides Adducted with First Row Divalent Transition Metal Ions

3.1 Introduction

Despite the variety in applications, the performance of ECD is still not satisfactory [117,118]. For instance, the efficiency of ECD for dications in practice is always lower than 20%. In addition, some natural motif [119], or post-transitional modification [120,121] may suppress or eventually inhibit the ECD fragmentation by trapping the "hot" hydrogen radical or holding the fragment ions together through non-covalent interactions. Generally, there are two main directions to improve the performance of ECD. The first direction is related to experimental factors, which involves design of better electron source and injection system [122,123], manipulation of energy for incoming electron (~0 to 50 eV) (HECD) [124] and spatial distribution of trapped ions (SORI-ECD) [125], and activation of the ions before or after electron irradiation (AI-ECD) [126,127]. The second direction involves tuning the charge states of the precursor ions by addition of chemical derivatives, and changing the charge carriers to tune the ECD fragmentation patterns [128-130].

Due to the diverse reactivity of metal ions in gas phase [129], using metal ions as cationizing agents for ECD of peptides may provide complementary sequence information compared to protonated peptides. Especially for transition metal ions, which offer the most diverse and interesting chemistry by formation of a variety of complexes with peptides. Many previous studies have investigated the ECD of metal ions adducted to biomolecules and model peptides [128-140]. The key questions in

ECD of metal ion peptide adduct are the electron neutralization site(s) of the metal ion-peptide complex and the determining factor(s) of various fragmentation patterns. For alkaline metal ions, Williams and co-workers [128] found that ECD of alkali metal ions (Li^+ and Cs^+) adducted model peptides produced exclusively metalated *c*-/*z*-type fragment ions and concluded that the incoming electron tended to neutralize the cation of higher recombination energy. Our group [131] studied the ECD fragmentation of model peptides adducted with alkaline earth metal ions. The incoming electron was believed to be captured by the mobile proton, rather than metal ions. It seems that the metal ions did not play any significant roles in the dissociation process. With regard to transition metal ions, Heck *et al.* [130] classified the ECD behavior as typical (Ni^{2+}, Co^{2+}, and Zn^{2+}) and atypical (Cu^{2+}) by examining the types of ECD fragment ion of metalated hormone oxytocin complexes. Hâkannson *et al.* [132] probed the divalent metal ion-Substance P (SubP) interactions by ECD of metal ion and proton co-adducted SubP trications. These authors suggested that the electron transfer from metal ions to peptide would be correlated to the second ionization energies of metals. Yuri *et al.* [137] attributed the different cleavage patterns obtained from ECD of peptides adducted with different metal ions to the conformational changes of the peptide models. Recently, ECD of histidine-containing and methionine-containing small peptides adducted with platinum complexes were investigated by O'Hair and co-workers [140]. No radical-type fragmentation along the peptide backbone was generated. Only minor sequence ions of *a*-, *b*-, and *y*-type with Pt were occasionally observed.

As summarized above, the effects of metal ions as charge carriers on the ECD fragmentations of the "real" biomolecules have been studied. Due to the presence of strong metal-anchoring group in the amino acid residues, ECD spectra of some metal ion adducted peptides were suppressed to specific bonds cleavage and/or concomitant with some neutral loss from the side chain of a specific amino acid residue in peptides. This type of product ions may be recognized as diagnostic marker ions for the existence

of specific side chain or indicative of interactions between metal ions and the corresponding residues. However, on the other hand, it may limit the fragmentation and conceal the behaviors of ECD for different metal-peptide adducts. For example, ECD of Ni^{2+} and proton co-adducted SubP trications mainly induced side chain loss of methionine, and generated limited sequence ions of peptide [132]. Besides the special metal-anchoring group, the relative rigid frame structure of peptide and "steric effects" induced by "bulky" side chain of specific amino acid residues may inhibit the accommodation of metal ion to its preferred mode of coordination. Investigation of the ECD fragmentation of metal ion adducts of model peptides with relative flexible frame may provide additional information on the mechanism of ECD.

As an extension of our previous work [131], in this study, we report ECD experimental studies of divalent transition metal ion (Mn^{2+}, Fe^{2+}, Co^{2+}, Ni^{2+}, Cu^{2+}, and Zn^{2+}) adducts of model peptides. Table 3.1 summarized the ionization energies, electronic configurations and coordination chemistries of the first row divalent transition metal ions [129, 132]. Model peptides with a general frame of ZGGGXGGGZ, where X is either V or W; and Z is either R, K, H or N, were used. The use of this peptide model, as opposed to the use of bioactive peptides, was to induce residues with mechanistic illustration and to reduce the complexity of the spectra. The inclusion of two basic amino acids (Z) in the model peptides was to ensure the generation of abundant of doubly-protonated peptide ions in order to compare their ECD spectra. Three different basic amino acids, R, K, H, and the neutral polar amino acid, N, were used to compare the ECD fragmentation of metalated peptides with the protonated analogue of different proton affinities. Glycine spacers were used to separate amino acid residues and to provide a frame with relatively high flexibility.

3.2 EXPERIMENTAL

Sample Preparation

Table 3.1 A summary of the physical and chemical information related to the selected divalent transition metal ions.

Element	Symbol	1st IP kJ/mol	2nd IP kJ/mol	Electronic configuration				Ionic Radius (Å)[b]		
				M^{2+}	M^{+}			4-coordinated	6-coordinated	8-coordinated
					Ground state	1st Excited state	ΔE kJ/mol			
Manganese	Mn	717.3	1509.0	$3d^5$	$3d^54s^1$	$3d^54s^1$ ($3d^6$) [a]	112.9 (174.5) [a]	0.80	0.81(0.97)[c]	1.10
Iron	Fe	762.5	1516.9	$3d^6$	$3d^64s^1$	$3d^7$	24.1	0.77(0.78)[d]	0.75(0.92)[c]	1.06
Cobalt	Co	760.4	1648.0	$3d^7$	$3d^8$	$3d^74s^1$	41.5	0.72	0.79(0.88)[c]	1.04
Nickel	Ni	737.1	1753.0	$3d^8$	$3d^9$	$3d^84s^1$	105.2	0.69(0.63)[d]	0.83	-
Copper	Cu	745.5	1957.9	$3d^9$	$3d^{10}$	$3d^94s^1$	271.1	0.71(0.71)[d]	0.87	-
Zinc	Zn	906.4	1733.3	$3d^{10}$	$3d^{10}4s^1$	-	-	0.74	0.88	1.04

[a] Second excited state;

[b] For doubly-charged species;

[c] Values correspond to radii for low spin (high spin) electronic configurations;

[d] Values correspond to radii for tetrahedral (square-planar) coordination.

All materials were obtained commercially and were used without further purification Magnesium (II) acetate and Copper (II) acetate were obtained from Beijing HuaGongChang (Beijing, China); Cobalt (II) acetate, Nickel (II) acetate were obtained from Acros (USA); Zinc (II) acetate was obtained from Riedel-deHaën (Germany); Iron (II) chloride was obtained from Sigma Company. Model peptides were custom-synthesized by Peptron Inc., (Daejeon, South Korea). The samples were prepared at concentrations of $1 \times 10^{-4} - 2.5 \times 10^{-4}$ M in 1:1 water: methanol (Labscan Ltd., Bangkok, Thailand). The concentrations of the metal salts were 5 mM in peptide solutions.

Instrumentation

All experiments were performed on a 4.7 Tesla FTMS system (APEX III, Bruker Instrument Inc., Boston, MA). This instrument was equipped with a standard, commercially available external electrospray ion source (Analytica, Branford, CT). The ESI ion source was modified to adopt a homemade nanospray assembly. Eight to ten μL of sample solution was loaded into a tapered capillary tip, which was electrically grounded using a 15 μm gold-plated tungsten wire. Intact molecular ions were produced. Ion transmission from the external source into the trapped ion cell was achieved by using the standard electrostatic lens system. The sidekick ion accumulation method was used to facilitate the ion trapping process. Ten cycles of multiple ions filling (MIF) were used to enhance the intensity of precursor ions [141]. In all experiments, static trapping potentials of 1.0 V were used. Initial calibration of the instrument was achieved by using a peptide mixture containing LGF, angiotensin II, and melittin. A standard electrically heated filament source was used to produce pulses of electron beam. The filament was made of rhenium ribbon and was fixed at a distance of 108 mm from the rear end of the Infinity cell. Details of the geometry of the filament source have previously been described in Chapter 2. Typical experimental conditions were 3.3 A filament heating current, 3.5-3.8 V average filament bias voltage, and 800-1000 ms

electron irradiation time. All ECD mass spectra were acquired in broadband mode using 128/256 k-byte dataset. Thirty to fifty scans were normally summed to improve the signal-to-noise ratio. The time-domain signals were zero-filled once before Fourier transformation.

Calculations

All calculations were performed using the Gaussian 03 package [110]. Equilibrium geometries were determined by full optimization followed by harmonic frequency calculations to confirm the nature of minima and transition states. All the stationary points were optimized using the Beck three parameter hybrid (B3LYP) exchange-correlation functional in the framework of the Kohn-Sham density functional theory (DFT) [111-113]. The standard split-valence basis set 6-31++G(d,p) was used for H, C, N and O atoms. All the metal cations were described by employing the Hay-Wadt effective core potential (ECP) with LANL2DZ basis set [114-115]. Single point energy calculation were calculated at the B3LYP level in conjunction with LANL2DZ+6-311++G(3df,2p) basis set.

3.3 RESULTS

3.3.1 ECD of transition metal ions adducted RGGGVGGGR

Figure 3.1 and 3.2 present ECD spectra of RGGGVGGGR metalated with Mn^{2+}, Fe^{2+}, Co^{2+}, Ni^{2+}, Cu^{2+}, and Zn^{2+}, respectively. Product ions are labeled according to our previously proposed nomenclature, in which $\overline{c}-$ and $\overline{z}-$ denotes the corresponding N- and C-terminal fragments originated from the homolytic cleavage of the N-C_α linkages, respectively. Any surplus of proton/hydrogen atom or metal ion/atom is indicated in the label [131].

The sequence ion assignments of the ECD spectra of the Mn^{2+} adducted RGGGVGGGR are given in Table 3.2. As summarized in the bond cleavage inserts, abundant fragment ions distributed across the peptides sequences were generated in the

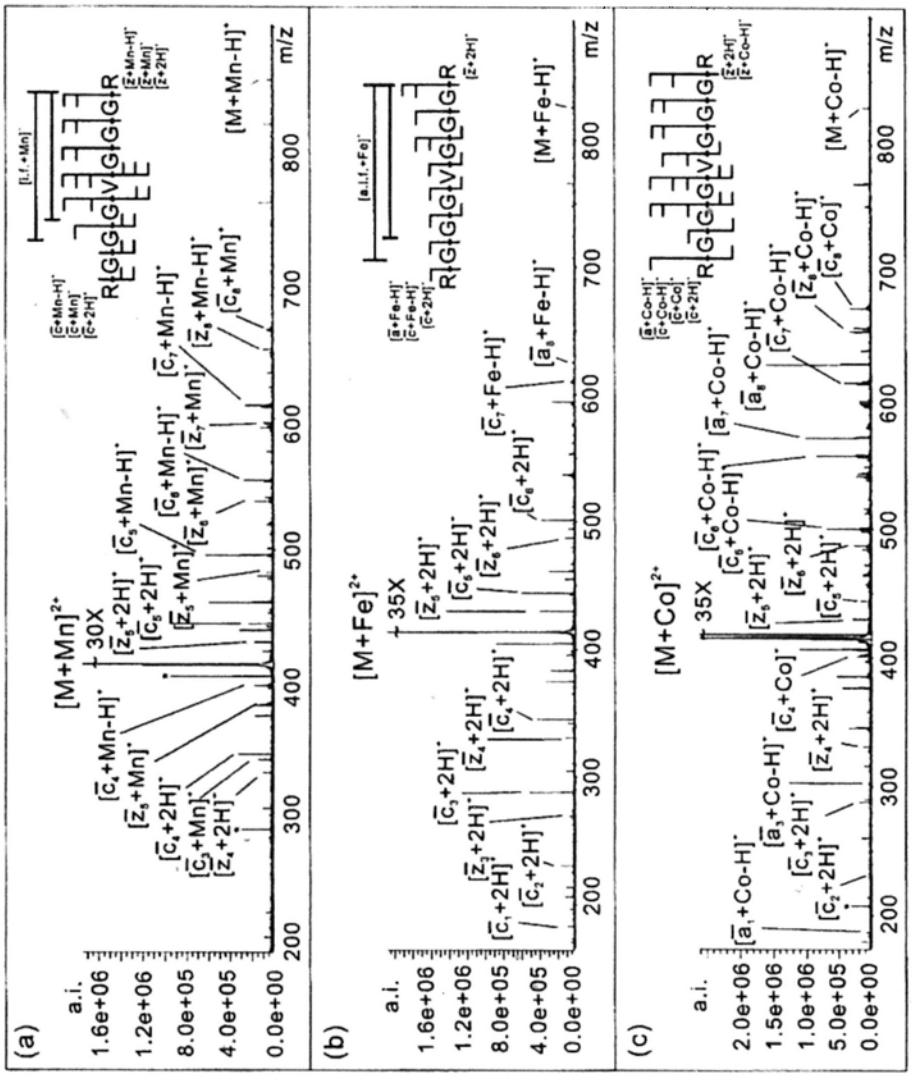

Figure 3.1 Typical ECD mass spectra of RGGGVGGGR adducted with (a) Mn^{2+}, (b) Fe^{2+}, (c) Co^{2+}. "i.f." refers to the internal fragment ions.

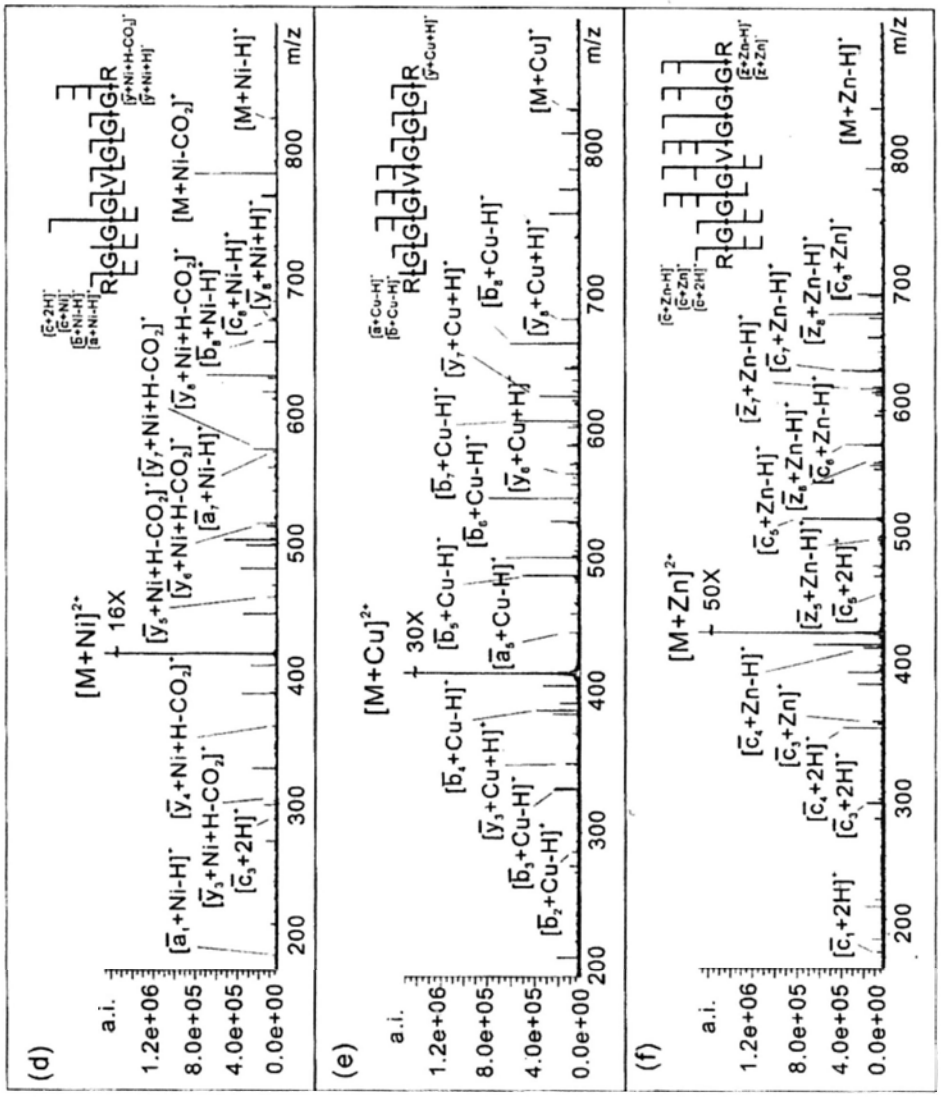

Figure 3.2 Typical ECD mass spectra of RGGGVGGGR adducted with (d) Ni^{2+}, (e) Cu^{2+} and (f) Zn^{2+}.

ECD spectra. The ECD fragment patterns of peptides adducted with different transition metal ions are quite different from each others. It is interesting to find that non-metalated fragment ions were observed for all the ECD spectra of metal ions adducted peptides except for Cu^{2+}. Among the selected transition metal ions, ECD of Mn^{2+} and Zn^{2+} adducted RGGGVGGGR trigger similar types of fragment ions to those obtained from protonated and alkaline metal adducted peptides. The abundances of fragment ions, however, were quite different. For Mn^{2+} adducted peptide, three non-metalated fragment ions, $[\overline{c}_n + 2H]^+$ (n=4 and 5) and $[\overline{z}_5 + H]^+$ were generated. In addition to the protonated fragment ions, abundant metalated *c*-/*z*-type fragment ions were observed, among which $[\overline{c}_5 + Mn - H]^+$ was found to be the most intense fragment ions. In general, metalated *c*-type fragment ions are higher in abundance than the metalated *z*-type fragment ions, which is consistent with that of protonated peptide. Being very similar to the case of alkaline earth metalated peptides, the $[\overline{c}_n + Mn]^+$ fragments are generally less abundant than the corresponding $[\overline{c}_n + Mn - H]^+$ fragments. For the ECD spectrum of RGGGVGGGR adducted with Fe^{2+}, approximately 70% of the fragment ions were protonated *c*-/*z*-type fragment ions. Only minor metalated *c*-ions, $[\overline{c}_n + Fe\text{-}H]^+$ (n=5-7) along with lose of NH_3, were observed. The ECD fragment patterns of the Co^{2+} adducted peptide exhibits some differences as compared with that of Mn^{2+} and Fe^{2+}. Apart from the protonated and metalated *c*- and *z*-fragment ions, abundant metalated *a*-fragment ions were observed. The ECD spectrum of Ni^{2+}-metalated RGGGVGGGR was dramatically different from that of other metal ions. Predominantly metalated *a*-type fragment ions and *y*-type fragment ions with concomitant CO_2 loss were generated. Only one low intensity metalated *c*-ion and one protonated *c*-ion were observed. ECD of Cu-metalated peptide produced mainly metalated *b*- and *y*-type fragment ions through the cleavages of amide

Table 3.2 Assignment of peaks in the ECD spectrum of RGGGVGGGR adducted with Mn^{2+}.

	Theoretical mass	Experimental Mass	S/N	Error in ppm
$[M+Mn-H]^+$	825.3401	825.3388	11.6	-1.6
$[\overline{c}_8+Mn-H]^+$	667.2467	667.2556	6.1	13.4
$[\overline{z}_8+Mn-H]^+$	653.2198	653.2317	10.5	18.2
$[\overline{c}_7+Mn-H]^+$	610.2252	610.2262	30.8	1.6
$[\overline{z}_7+Mn]^+$	597.2062	597.2132	12.6	11.7
$[\overline{c}_6+Mn-H]^+$	553.2038	553.2048	31.0	1.8
$[\overline{z}_6+Mn]^+$	540.1847	540.1869	11.8	4.1
$[\overline{c}_5+Mn-H]^+$	496.1823	496.1858	70.8	7.1
$[\overline{z}_5+Mn]^+$	483.1632	483.1480	8.5	-31.6
$[\overline{c}_5+2H]^+$	444.2677	444.2731	30.2	12.2
$[\overline{z}_5+2H]^+$	430.2408	430.2515	21.3	24.8
$[M+Mn]^{2+}$	413.1735	413.1672	4878.9	-15.2
$[\overline{c}_4+Mn-H]^+$	397.1139	397.1222	23.0	20.9
$[\overline{c}_4+2H]^+$	345.1993	345.1992	39.0	-0.2
$[\overline{c}_3+Mn]^+$	341.1002	341.0973	16.1	-8.5
$[\overline{z}_4+2H]^+$	331.1724	331.1741	12.1	5.0

linkages. ECD spectrum of Zn^{2+} adducted peptide is very similar to that of Mn^{2+}. Mainly metalated *c*-/*z*-type fragment ions, together with two non-metalated *c*-ions, were observed.

3.3.2 ECD of transition metal ions adducted NGGGWGGGN

In order to investigate the importance of the zwitterionic form of the precursor ions on the ECD fragmentation pattern, a similar model peptide of NGGGWGGGN was analyzed by using different metal ions as charge carriers. In this peptide sequence, non-basic polar amino acid residues, i.e. N, were used instead of arginine resiudes. The absence of basic amino acid residues should suppress the deprotonation of the amide hydrogen. Figure 3.3 and 3.4 present ECD spectra of NGGGWGGGN metalated with Mn^{2+}, Fe^{2+}, Co^{2+}, Ni^{2+}, Cu^{2+}, and Zn^{2+}, respectively. The sequence ion assignments of the corresponding Mn^{2+} adducted NGGGWGGGN are given in Table 3.3. Consistent with previous observations using alkaline earth metal ions as charge carriers [131], no non-metalated fragment ion was generated for all transition metal ions adducted NGGGWGGGN. All fragment ions observed in these spectra are metalated. Another noticeable difference between the two model peptides is that more internal fragment ions were produced in case of NGGGWGGGN. For ECD of Mn^{2+}, Co^{2+}, and Zn^{2+} adducted NGGGWGGGN precursor ions, considerably less metalated *c*- and *z*-type fragment ions were observed in the ECD spectra compared to that of the corresponding metalated RGGGVGGGR. Among the selected metal ions, spectra of Fe^{2+} adducted peptide (i.e. ECD of $[Fe(RGGGVGGGR]^{2+}$ *vs* $[Fe(NGGGWGGGN)]^{2+}$) show the largest differences. Mainly metalated *a*- and *c*-type fragment ions, instead of protonated *c*-type ions, were observed. For Ni^{2+} adducted NGGGWGGGN, the patterns of fragment ions were similar to that of RGGGVGGGR. Mainly metalated *a*- and *y*-type ions, were observed, no CO_2 elimination was observed. Similar to the spectrum of Cu^{2+} adducted RGGGVGGGR, metalated b-type fragment ions were generated in the ECD

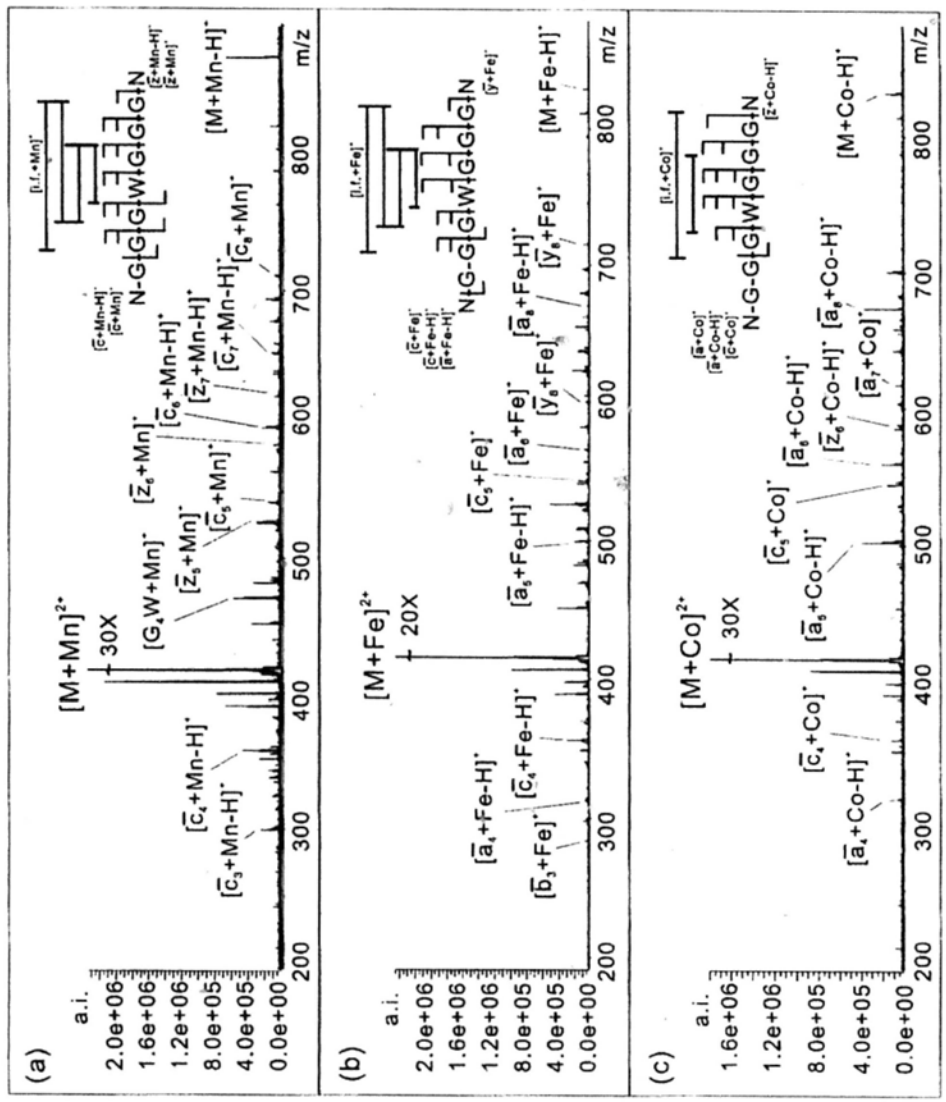

Figure 3.3 Typical ECD mass spectra of NGGGWGGGN adducted with (a) Mn^{2+}, (b) Fe^{2+} and (c) Co^{2+}. "i.f." refers to the internal fragment ions.

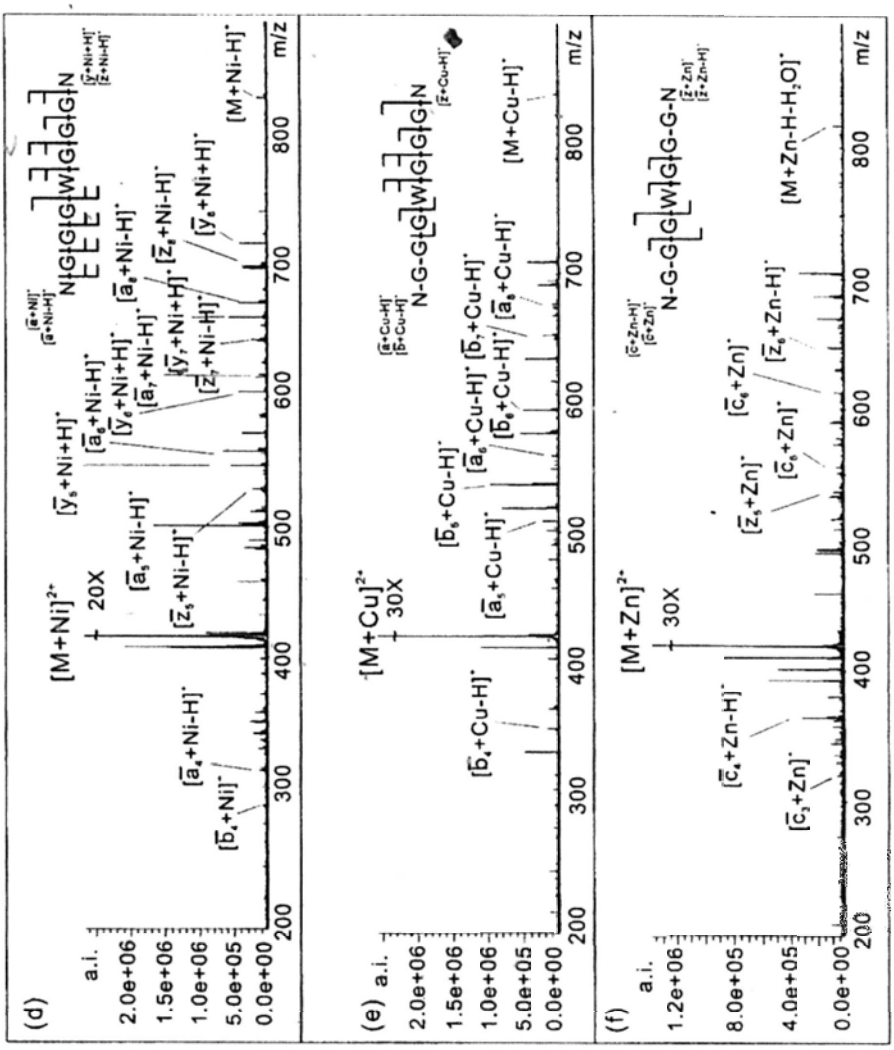

Figure 3.4 Typical ECD mass spectra of NGGGWGGGN adducted with (d) Ni^{2+}, (e) Cu^{2+} and (f) Zn^{2+}.

Table 3.3 Assignment of peaks in the ECD spectrum of NGGGWGGGN adducted with Mn^{2+}.

	Theoretical mass	Experimental Mass	S/N	Error in ppm
$[M+Mn-H]^+$	828.2347	828.2338	11.7	-1.0
$[\bar{c}_8+Mn+H]^+$	714.2150	714.2073	6.7	-10.9
$[\bar{c}_7+Mn-H]^+$	655.1779	655.1766	9.4	-2.0
$[\bar{z}_7+Mn-H]^+$	641.1511	641.1432	7.4	-12.1
$[\bar{z}_6+Mn]^+$	585.1374	585.1467	7.9	15.8
$[\bar{c}_6+Mn-NH_3]^+$	582.1377	582.1356	4.3	-3.8
$[G_5+Mn]^+$	526.1241	526.1163	28.5	-14.7
$[\bar{c}_5+Mn-H]^+$	541.1350	541.1360	10.5	1.8
$[\bar{z}_5+Mn]^+$	528.1159	528.1222	19.0	11.9
$[\bar{c}_5+Mn-H_2O]^+$	524.1322	524.1322	5.6	-0.2
$[G_4+Mn]^+$	469.1026	469.1065	49.5	8.3
$[M+Mn]^{2+}$	414.6207	414.6209	3501.3	0.4
$[\bar{c}_4+Mn-H]^+$	355.0557	355.0617	44.7	16.8
$[\bar{c}_3+Mn-H]^+$	298.0342	298.0418	9.2	25.3
$[\bar{b}_3+Mn]^+$	284.0311	284.0335	3.4	8.5

of Cu^{2+} adducted NGGGWGGGN.

3.4 DISCUSSION

3.4.1 Formation of non-metalated fragments ions

The formation of non-metalated fragment ions from electron capture dissociation of divalent metal ion adducted peptide dications is of fundamental and analytical interests. Such non-metalated fragment ions generated by ECD of metalated peptides have also been reported previously [131,132]. The appearance of such protonated fragment ions fundamentally indicates the existence of zwitterionic structures in the precursor ions. For the metal ion-peptide binary complex, the formation of zwitterionic structures requires the deprotonation and re-protonation within the metal ion-peptide complex. The two types of the most favorable deprotonation sites of the model peptides studied here are the C-terminal carboxylic acid group (-COOH) and the backbone amide (NH) groups [142-145]. The side chains of the two basic amino acid residues and the N-terminal (NH_2) group constitute the sites with highest proton affinity, and thus are believed to be the most possible re-protonation site(s) in the model peptides. To check the effects of the crucial functionalities on the formation of protonated fragment ions, The ECD spectra of a structurally variants of RGGGVGGGR were obtained. Figure 3.5(a-c) shows typical ECD spectra of Mn^{2+} metalated modified peptide as an example.

In order to investigate the effect of re-protonation sites on the formation of protonated fragment ions, ECD of metal ions adducted peptides where the C-terminal arginine was substituted for to aspargine and the N-terminus was subsequently acetylated were performed. The corresponding non-metalated *c*-type fragment ions for the two modified peptides are similar to that the parent peptide, which demonstrated that replacing the C-terminal arginine and the N-terminus (NH_2) did not inhibit the formation of extensive protonated *c*-type fragment ions. However, the protonated fragment ions completely completely disappearred in the ECD spectra of metal ion

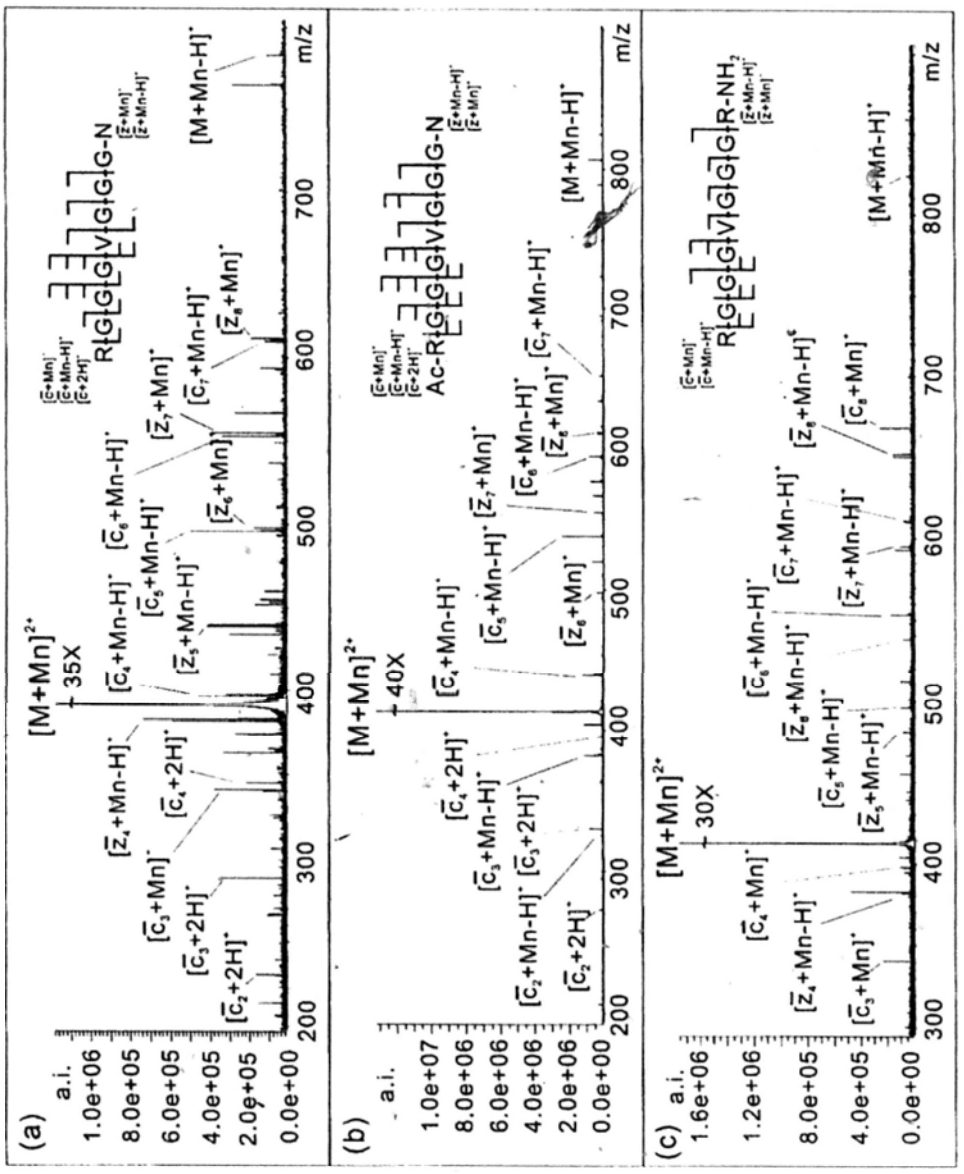

Figure 3.5 Typical ECD mass spectra of Mn^{2+} adducted (a) RGGGVGGGN, (b) RGGGVGGGR-NH_2, (c) Ac-RGGGVGGGN.

adducted peptide with amidated C-terminus. It indicated that the free C-terminal carboxylic site is essential for the formation of non-metalated fragment ions.

Considering the reprotonation of precursor ions, the incoming electron might selectively neutralize the mobile proton or the metal ions depending on the nature of metal ion-peptide complexes. For the singly zwitterionic precursor isomer, the formation of non-metalated fragment ions may be interpreted based on the "superbase" mechanism. The existing proton acts as a charge carrier for the fragment ions. Electron captured by the backbone π^* orbital generates the anionic radical. Subsequently, the released energy might activate the complex to liberate another mobile proton via conformational changes of the metal peptide complex. The anionic radical might abstract the mobile proton to form the ketylamino radical and generate the non-metalated fragment ions. For the doubly zwitterionic precursor isomer, the formation of non-metalated fragment ions can be understood by either the "hot hydrogen atom" mechanism or the "superbase" mechanism. The absence of these fragment ions in ECD of K, H, and N containing peptides was tentatively attributed to the low deprotonation-reprotonation reactivies of metal ion-peptide complexes.

3.4.2 The role of precursor ion heterogeneity

Previously [131], we have demonstrated that the precursor ion heterogeneity ($[(M + Cat^{2+} - nH^+)^{(2-n)+} + nH^+]^{2+}$ (n = 0, 1, and 2)) was one of the important factors that affects the ECD fragmentation of peptides adducted with alkaline earth metal ions. To explore the possible correlation between the precursor ion heterogeneity and the fragmentation behavior, the deprotonation reaction mediated by 1st row divalent transition metal ions was investigated by using N-methyl glycyl-glycinamide as a truncated peptide model. Scheme 3.1 shows the potential energy diagrams of deprotonation reaction mediated by 1st row transition metal ions. To reduce the complexity of the coordination mode, the stationary points (**A**, $\mathbf{TS_{A\text{-}B}}$, and **B**) adopt a

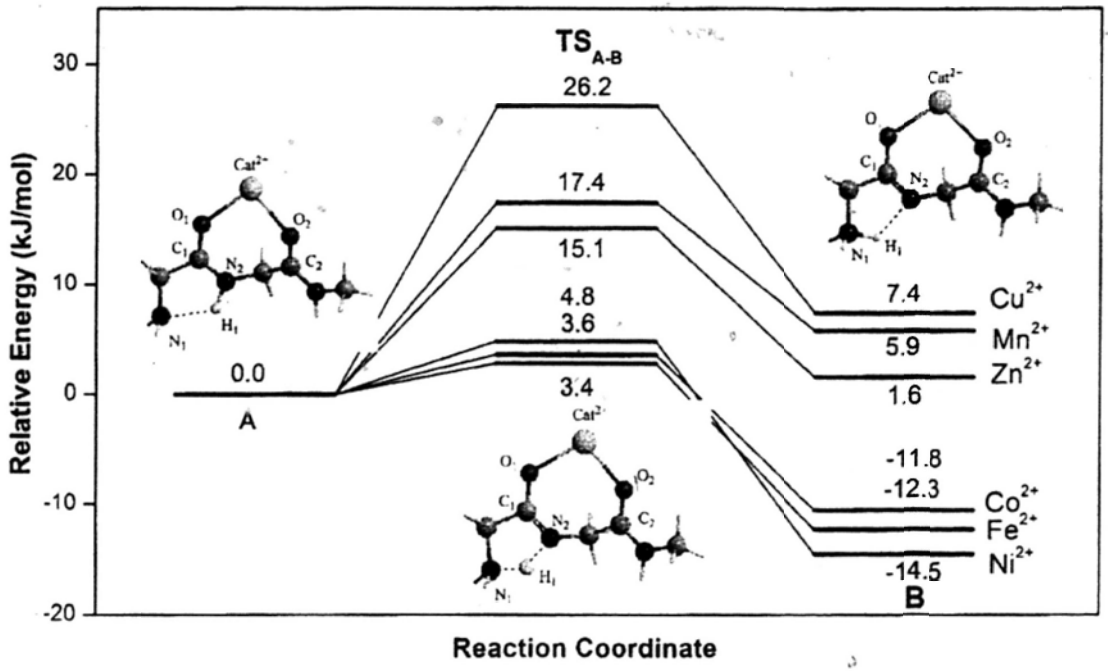

Scheme 3.1 Potential energy diagrams associated with the deprotonation reactions of first row divalent transition metal ions adducted N-methyl glycyl-glycinamide. Single point energy calculated at the B3LYP/LANL2DZ+6-311++G(3df,2p) based on the structures optimized at B3LYP/LANL2DZ+6-31++G(d,p) level. The scale factor for ZPE is 0.961.

Table 3.4 Optimized bond distances (Å) for the reactants, transition states and products involved in the deprotonation reactions at the B3LYP/LANL2DZ+6-31++G(d,p) level.

R	Mn^{2+}			Fe^{2+}			Co^{2+}		
	A	**TS_{A-B}**	**B**	**A**	**TS_{A-B}**	**B**	**A**	**TS_{A-B}**	**B**
$R(H^1\text{-}N^1)$	1.958	1.308	1.052	1.948	1.327	1.048	1.954	1.329	1.476
$R(H^1\text{-}N^2)$	1.039	1.297	1.892	1.041	1.281	1.930	1.041	1.279	1.937
$R(C^1\text{-}O^1)$	1.284	1.294	1.314	1.288	1.298	1.321	1.287	1.297	1.321
$R(C^1\text{-}N^2)$	1.320	1.301	1.285	1.319	1.301	1.284	1.318	1.299	1.283
$R(Cat^1\text{-}O^1)$	1.929	1.919	1.906	1.876	1.867	1.854	1.859	1.849	1.835
R	Ni^{2+}			Cu^{2+}			Zn^{2+}		
	A	**TS_{A-B}**	**B**	**A**	**TS_{A-B}**	**B**	**A**	**TS_{A-B}**	**B**
$R(H^1\text{-}N^1)$	1.963	1.327	1.045	2.210	1.329	1.042	1.938	1.318	1.050
$R(H^1\text{-}N^2)$	1.041	1.280	1.971	1.022	1.276	2.014	1.041	1.288	1.912
$R(C^1\text{-}O^1)$	1.288	1.293	1.323	1.254	1.283	1.302	1.286	1.297	1.320
$R(C^1\text{-}N^2)$	1.317	1.301	1.282	1.329	1.306	1.295	1.323	1.303	1.286
$R(Cat^1\text{-}O^1)$	1.841	1.848	1.811	1.922	1.861	1.861	1.901	1.894	1.883

Table 3.5 Energies (E), zero-point energies (ZPE), total energies (E_{total}) (in hartrees) and relative energies (ΔE) (in kJ/mol) calculated at B3LYP/LANL2DZ+6-31++G(d,p) level and single point energies calculation at B3LYP/LANL2DZ+6-311++G(3df,2p) level.

		B3LYP/LANL2DZ+6-31++G(d,p)				B3LYP/LANL2DZ+6-311++G(3df,2p)		
Metal ion	Species	E	ZPE	E_{total}[a]	ΔE	E	E_{total}[a]	ΔE
Mn^{2+}	**A**	-615.304323	0.179577	-615.131750	0.00	-615.471331	-615.298757	0.00
	TS_{A-B}	-615.295678	0.176137	-615.126410	14.02	-615.461409	-615.292141	17.37
	B	-615.302945	0.180323	-615.129655	5.50	-615.469821	-615.296531	5.85
Fe^{2+}	**A**	-634.785007	0.179405	-634.612599	0.00	-634.948852	-634.776444	0.00
	TS_{A-B}	-634.777580	0.176099	-634.608349	11.16	-634.944388	-634.775157	3.38
	B	-634.786572	0.180325	-634.613280	-1.79	-634.954400	-634.781108	-12.25
Co^{2+}	**A**	-656.408685	0.179448	-656.236236	0.00	-656.572090	-656.399640	0.00
	TS_{A-B}	-656.401284	0.175976	-656.232171	10.67	-656.567366	-656.398253	3.64
	B	-656.410450	0.180534	-656.236957	-1.89	-656.577632	-656.404138	-11.81
Ni^{2+}	**A**	-680.618142	0.179212	-680.445919	0.00	-680.783201	-680.610978	0.00
	TS_{A-B}	-680.611580	0.176150	-680.442300	9.50	-680.778416	-680.609136	4.84
	B	-680.622850	0.180406	-680.449480	-9.35	-680.789863	-680.616493	-14.48
Cu^{2+}	**A**	-707.454030	0.178054	-707.282920	0.00	-707.619287	-707.448177	0.00
	TS_{A-B}	-707.441809	0.175305	-707.273341	25.15	-707.606668	-707.438200	26.19
	B	-707.452309	0.179546	-707.279766	8.28	-707.617902	-707.445358	7.40
Zn^{2+}	**A**	-576.927667	0.179432	-576.755233	0.00	-577.093291	-576.920857	0.00
	TS_{A-B}	-576.920089	0.176084	-576.750872	11.45	-577.084333	-576.915116	15.07
	B	-576.928188	0.180288	-576.754931	0.79	-577.093520	-576.920263	1.56

[a] Scale factor for ZPE is 0.961

conformation in which the metal ion (Cat^{2+}) was bi-coordinated by the carbonyl oxygen atoms. The optimized geometrical parameters and energies of all the stationary points are shown in Table 3.4 and 3.5. As shown in Scheme 3.1, the reactivies of intramolecular proton transfer reactions mediated by different metal ions were generally inversely proportional to the size of the metal ions except for Cu^{2+} (Table 3.1). For the deprotonation reactions mediated by Fe^{2+}, Co^{2+} and Ni^{2+}, the energy barriers for intra-molecular proton transfer were relatively lower and the reactions calculated were more exothermic as compared to the other metal ions. It indicates that the population of zwitterionic conformers in precursor ions might be higher than other transition metal ions. However, as shown previously, the ECD "behaviors", especially the patterns of fragment ions, for these metal ions adducted peptides are different from the typical behavior ECD of protonated peptides. For the deprotonation reactions mediated by Cu^{2+}, the energy barrier for proton transfer was of relatively high energy and the reaction calculated was more endothermic. Thus, the population of zwitterionic conformers in precursor ions should be lower than other transition metal ions. It is also consistent with the fragmentation behavior of Cu^{2+} adducted peptide. Almost no typical ECD fragment ions were observed in the spectrum of Cu^{2+} adducted peptides. Mn^{2+} and Zn^{2+} show in-between deprotonation reactivities as compared with Cu^{2+} and other metal ions. However, the fragment ions generated by ECD of the two metal ion adducted peptides are typical ECD fragment ions. Based on the calculated results, no direct correlation was found between the behavior of ECD of metalated peptides and the deprotonation reactivies.

3.4.3 Trends in ECD fragmentation of metalated peptides

Since different transition metal ion adducted peptides were found to generate different types of fragment ions, it might be informative to plot the relative contributions of different dissociation channels of metalated peptides across the 1st row

transition metal ions (i.e. the number of d-electrons). Three types of fragment ions were commonly found in the ECD spectra and were tentatively treated as originating from different dissociation channels. Type I fragments represent the characteristic fragment ions generated in ECD of protonated peptides. Because *c*-/*z*$^{\bullet}$-type fragment ions are typical ECD fragment ions in the ECD spectra of protonated model peptides studied here, we treat *c*-/*z*-type fragment ions both with and without metal ions as typical ECD fragment ions and denote as type I fragment ions. Type II fragments include metalated *a*- and *y*-type fragment ions. Type III fragment ions represent the typical species formed in the CID of protonated peptides, including metalated *b*-/*y*- ions. Since *y*-ions are formed in both type II and III fragment ions, its contribution to the abundance of type II and type III fragment ions were assumed to be proportional to the relative intensity of the corresponding *a*-/*b*- ions. The product ion abundance (PIA) of each type of fragment ions was calculated using the equation (1):

$$\text{PIA } (type\ X) = \frac{\sum(\%type\ X)}{\sum(\%all\ fragment\ ions)} \times 100\% \qquad (1)$$

where X = I, II or III.

Fragment ion intensity contributed by metastable dissociation under the present trapping conditions was eliminated by control experiments. The control experiments were acquired right after the acquisition of the normal ECD spectrum using the same tuning conditions and pulse program, while the electron irradiation event was replaced by a decay of the same duration. The contribution made in non-electron irradiation conditions was subtracted from that of normal ECD experiment. Figure 3.6 shows the PIA(s) of various types of fragment ions in the ECD of different metal ion adducted RGGGWGGGR and NGGGWGGGN. It is interesting to note that the trends of the PIA(s) of the two peptides are quite similar.

Both Mn^{2+} and Zn^{2+} show almost exclusively c-/z- fragment ions (i.e. type I). The

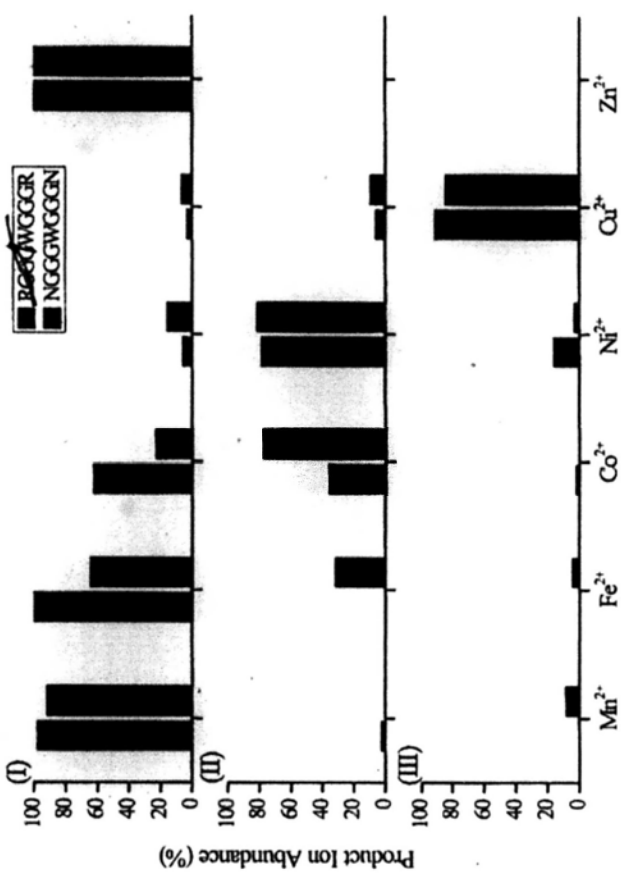

Figure 3.6 Product ion abundances (PIA) of metalated ZGGGWGGGZ (Z=R and N).

Table 3.6 Product ion abundances (PIA, %) of ECD of first metal ions adducted ZGGGWGGGZ (Z=K and H).

Metal Ions	KGGGWGGGK			HGGGWGGGH		
	Type (I)	Type (II)	Type (III)	Type (I)	Type (II)	Type (III)
Mn^{2+}	55.5	16.2	9.3	78.6	--	--
Fe^{2+}	52.1	12.0	7.8	69.3	21.2	--
Co^{2+}	31.3	48.4	9.2	23.9	34.7	23.3
Ni^{2+}	--	34.9	37.6	3.8	85.6	1.5
Cu^{2+}	--	--	87.5	--	--	86.3
Zn^{2+}	81.9	9.5	--	81.9	9.9	--

intensity of *c-/z-*fragment ions decrease progressively from Mn^{2+} to Ni^{2+} with a concomitant increase of the *a-/y-* fragment ions (type II). From the present experimental information, it seems that there is a progressive shift of the fragmentation channel across the 1st row transition metals. In line with previous experiments, Cu^{2+} adducted peptide behaved rather differently. In all cases, ECD of Cu^{2+} adducted peptides show type III fragment ion, i.e. exclusively *b-/y-* ions.

Now we compare the PIA of each type of fragment ions for different model peptides metalated with the same metal ions. Considering RGGGWGGGR and NGGGWGGGN, more type I fragment ions were generated in the ECD of the same metal ions adducted RGGGWGGGR than those of the metalated NGGGWGGGN. As expected, more type II fragment ions were generated in the ECD of metal ions adducted NGGGWGGGN as compared with those of RGGGWGGGR. The PIAs of ECD of metal ions KGGGWGGGK and HGGGWGGGH were tabulated in Table 3.6. The general trends were similar to that of the arginine containing peptide.

3.4.4 The role of electronic configuration

3.4.4.1 Metal ions with half filled and fully filled d shells: Mn^{2+} and Zn^{2+}

By comparing the ECD fragmentation of selected divalent transition metal ions with that of alkaline [128] and alkaline earth metal ions [131], it is interesting to find that two of the selected metal ions, Mn^{2+} and Zn^{2+}, behaved similarily to alkaline earth metal ions, while others behaved differently. The studied alkaline earth metal ions, including Mg^{2+}, Ca^{2+}, Sr^{2+}, and Ba^{2+}, have the same valence electronic configuration of s^0 occupations. As shown in Table 3.1, this is also true for Zn^{2+} ions, which have a $3d^{10}4s^0$ electron configuration. Although the outmost electron orbital of Mn^{2+} is not fully filled, it has half filled d shells ($3d^5$). The common feature of these metal ions is that the outmost orbitals are relative stable. In the previous paper [131], we postulated that alkaline-earth metal ions reduction under the current electron capture dissociation

conditions did not play any significant role in inducing fragmentations. We believed it is also true for Mn^{2+}- and Zn^{2+}-adducted peptides. Because of their half filled or fully filled d shells, trapping of an electron in the 3d orbital is not favorable. If metal ion-electron recombination occurs, the incoming electron needs to occupy the 4s orbital with slightly higher energy. The corresponding ground state electronic configurations for Mn^{2+} and Zn^{2+} after charge reduction are high spin electronic configuration, $3d^5 4s^1$, and $3d^{10}4s^1$, respectively. However, these states with both s and d orbital occupied for transition metal monocations are particular unreactive [146]. Occupation of 4s orbital results in an increase in Pauli repulsion between the metal ions and coordinated peptides; on the other hand, the occupied 4s orbital prevents attractive binding interactions with the metal 3d electrons as well. Due to the existence of a mobile proton liberated by metal ion coordination, it is proposed that the electron would be captured by the mobile proton and/or backbone amide π^* to trigger the usual ECD dissociation channel(s) via "hot-hydrogen" or "superbase" intermediates to form a series of *c*-/*z*-type fragment ions. This explains the observation of *c*-/*z*-type fragment ions which resembles the ECD spectra of protonated species.

3.4.4.2 Metal ions with partially filled d shells: Fe^{2+}, Co^{2+}, and Ni^{2+}

We now turn to the other three metal ions. For Fe^{2+}, Co^{2+}, and Ni^{2+}, their outmost orbitals are neither half nor fully filled. For Co^{2+} and Ni^{2+}, accepting an electron into their outmost orbitals would lead to a ground state electronic configuration of $3d^n$ (n=8 and 9, respectively). The striking similarity of these metal ions is that their corresponding charge reduced monocations are low spin with more than one of the 3d orbitals doubly occupied (where low spin refer to ^3F and ^2D, as compared to the s occupation excited state ^5F ($4s^1 3d^7$), ^4F($4s^1 3d^8$) for Co^+ and Ni^+, respectively). The ground state of Fe^+ is ^6D ($4s^1 3d^6$), such that the 4s orbital will also be occupied by electron injection as in the case of Mn^{2+} and Zn^{2+}. However, the free Fe^+ has a ^4F ($3d^7$)

excited state that lies only 0.25eV above the ground state. It has been shonw that the Fe^+ (^4F) is more reactive and has an energically more favorable electronic state in ion-molecule reactions [147]. The switch of two different spin states for Fe^+ -complex can be approached by inter-system crossing [148,149]. Because Fe^{2+} adducted model peptides have more degrees of freedom as compared to those of small organic molecules, a longer lived metalated intermediate is proposed to be exist. The longer life of intermediates would allow a more frequent sampling of the crossing points. Therefore, the drastically different behavior of Fe^{2+} adducted RGGGVGGGR and NGGGWGGGN is believed to be the result of crossing of the potential energy surfaces. For Fe^{2+} adducted RGGGVGGGR, the incoming electron selectively neutralizes the mobile proton of zwitterionic precursor ions to form a radical and initials the typical dissociation channel. While for NGGGWGGGN, the incoming electron would be exclusively captured by the metal ions. The released energy is enough to induce the system crossing between different potential energy surfaces. Thus, it is proposed that the ^4F ($3d^7$) electronic state of Fe^+ formed after electron injection to Fe^{2+} is responsible for the odd ECD behavior. For Co^+ and Ni^+, the excited states, $3d^n4s^1$, (n=7 and 8) are unreactive and higher promotional energies are required. Thus, it is believed that the monocations favor a $3d^n$ electronic configuration during the dissociation process. Unlike the high spin $3d^n4s^1$ configurations, the $3d^n$ configuration of these metal ions provides attractive bonding interactions between the 3d orbitals and the peptides. Due to the high reactivity of electronic states with empty d and s orbitals for these metal ions, fragmentation formed after metal ions-electron recombination becomes more competitive to the usual ECD process. The incoming electron is believed to be trapped by the metal ions. It is proposed that the metal ion-electron recombination process is responsible for generating fragment species other than *c*-/*z*-type fragment ions. Thus, the fragment ions species observed for Fe^{2+}, Co^{2+} and Ni^{2+} were quite different to those observed in spectra of protonated and alkaline earth metal adducted peptides.

3.4.4.3 ECD of Cu^{2+} adducted model peptides

The ECD behavior of Cu^{2+} metalated model peptides stands apart from all the studied metal ions and generated exclusively metalated *b-/y-* fragment ions. Previous research proposed that the Cu^{2+}-peptide complexes favor reduction of Cu^{2+} to Cu^{+} forming.a closed d shell ($3d^{10}$) system in the electron irradiation event. Thus the typical CID fragment ions were formed by internal energy transfer induced vibrational excitation [130]. The other hypothesis was that Cu^{2+} was already reduced to Cu^{+} in the precursor ions through an "*internal*" electron-transfer before electron irradiation [132]. The incoming electron was captured by the peptide radical, rather than the metal ion. Further CID of Cu(I) adducted analogues might provide additional information about the two mechanisms.

3.4.5 Recombination of the electron: metal ion or proton

Previously, Heck and co-workers [130] suggested that metal ions act as an initial site of electron capture; and the subsequent electron transfer and energy transfer are two competitive processes in the ECD experiments of metalated oxytocin. The electron transfer process for Co^{2+}, Ni^{2+}, and Zn^{2+} adducted complexes leads to formation of hydrogen radical and causes typical ECD fragmentations. However, for the model peptides studied here, the ECD behavior of Co^{2+} and Ni^{2+} adducted peptide share some similarities, but quite different from that of Zn^{2+}. Håkannson *et. al.* [132] proposed that the ECD behavior correlated with second ionization energy (IE2) of metal. They explained the different fragmentation pattern for Co^{2+} and Ni^{2+} metalated SubP trications by their higher second ionization energy and the binding mode. The proposed correlation between IE2 of metal ions and ECD behavior of metalated peptide seems logical. Follow this assumption, more typical I fragment ions should be observed for Co^{2+} adducted peptides as compared to that of Zn^{2+}. In contrast to the prediction, type II fragment ions dominate the products in the ECD spectrum of Co^{2+} adducted

NGGGWGGGN. Thus, we believe that the IE2 of metal ions should not be the decisive factor for the ECD behavior of metal ion adducted model peptides studied here. In addition, previous theoretical results indicated that the recombination energy of metal ions would be largely decreased by ligand coordination as compared with the IE2 of a free metal atom [138,139]. Thus, it is not logical to directly correlate the ECD fragmentation of metalated peptides with the IE2 of free metal atom.

We now compare the dissociation behavior of ECD with the CID results for metalated peptide. If the "slow-heating" fragment ions were formed by energy transfer after electron captured by the metal ions, the resulting fragment types upon ECD and CID should be, to some extent, similar to each other. Gross and co-workers [150] found that *a*-type fragments were the dominant products in Co^{2+} and Ni^{2+}-peptide complexes ($[M + Cat - H]^+$) under CID conditions, especially at the C-terminal site of an amino acid residue with aromatic side chain. They also observed abundant of metalated *a*-type fragment ions in CID of Fe^{2+} adducted cysteine-containing peptides [151]. It is consistent with our observation that the metalated *a*- type fragment ions were observed in the ECD of Fe^{2+}, Co^{2+} and Ni^{2+}-metalated NGGGWGGGN. Russell and co-workers found that the principal decay products were metalated *b*- and *a*-type fragment ions in the metastable dissociation of Cu^+ ionized N-terminal arginine containing peptide, $[M + Cu]^+$, which resemble the ECD fragmentation of Cu^{2+} adducted model peptide studied here [152]. Wesdemiotis and co-workers investigated the post source decay (PSD) mass spectra of bradykinin (BK) relevant peptides complexed with Co^{2+}, Ni^{2+}, Cu^+ and Zn^{2+} [153]. Similarly, the primary fragment ions were also metalated *a*-, *b*- and *y*-type ions for PSD spectra of $[M + Cat - H]^+$ ($Cat = Co^{2+}$, Ni^{2+}) and $[M + Cu]^+$. These similarities between the ECD and vibrationally excitated dissociation techniques indicated that the "slow-heating" ECD fragment ions were generated by energy transfer after electron trapped by the metal ions, rather than the radical. On the other hand, no *c*-/*z*-type fragment ions were generated in either the PSD of $[M + Zn - H]^+$ or CID of $[M + Zn]^{2+}$

[154], the dominant fragment ions are the usual "slow-heating" *b*-/*y*-type fragment ions. These total different behaviors indicated that the ECD fragments of model peptides adducted Mn^{2+} or Zn^{2+} were induced by the radical formed after electron capture, rather than via vibrational excitation.

We propose that the typical ECD fragment ions are formed by usual ECD mechanism. Electron capture by metal ions and electron capture by mobile proton and/or amide π^* of the peptide are two competitive processes. This argument can be supported by comparing the PIAs of various fragment ions of model peptides metalated with the same metal ions. As discussed above, the main difference between the two type of peptides (RGGGWGGGR *vs* NGGGWGGGN) is the populations of isomers of precursor ions. For the metalated RGGGWGGGR, the population of zwitterionic structures is believed to be higher than that of NGGGWGGGN. This may provide greater possibilities for the usual ECD channel and thus more type I fragment ions were generated as shown in Figure. 3.6.

In summary, we proposed that the electronic configurations of divalent metal ions govern the ECD behaviors of their metalated model peptides. In other words, if the incoming electron favors an *s*-orbital occupation of the divalent transition metal ions, ECD of corresponding metalated peptides would favor generating typical ECD fragment ions; if the incoming electron favors a 3d-orbital occupation for the divalent transition metal ions, "slow-heating" type fragment ions would be generated, which mainly involves metalated *a*-, *b*- and *y*-type fragment ions.

3.4.6 Formation of metalated *a*-/*y*-type fragment ions

Formation of metalated *a*- and *y*-ions in the ECD spectra of Fe^{2+}, Co^{2+}, and Ni^{2+} adducted peptides shows a clearly tunable effect of metal ion adduction on the ECD fragmentation. It indicated that adduction of transition metal ions might "toggle" the major ECD channel. Among these three metal ions adducted peptides, the Ni^{2+} adducted

peptide, which generates predominantly metalated *a*-/*y*-type fragment ions, is of particular interest. This metal ion appears to "catalyze" this particular dissociation pathway which is not seen for any of the other metal ions studied.

From a survey of the literature [152], three fragmentation pathways have been proposed to account for backbone C_α-C cleavage besides the CO lost after the formation of *b*-ions. One is the amide hydrogen migration pathway. The second involves metal ions insertion into the C_α-C bond, followed by amide hydrogen transfer by metal ions. The third is the C_β hydrogen migration from side chain of residue. Because the inter-residue glycines of the model peptide do not inhibit the *a*-type fragment ions, the migrated hydrogen should not be essential from the side chain of inter-residues. If the electron was captured by the divalent transition metal ions, the reactivies of metal monocation should be taken into consideration. The metal monocation insertion into the C_α-C bond has been proposed for a number of metal ion-organic molecule reactions and verified by theoretical calculations [147,148]. Thus, here it is believed that insertion reactions might occur for the reduced peptide-metal ion complexes.

Scheme 3.2 shows a direct amide hydrogen transfer pathway, in which the metal ion acts as a spectator. Scheme 3.3 shows the indirect amide hydrogen transfer pathway with the metal ions as a hydrogen transmitter. Both the two mechanisms involve amide hydrogen migration. In order to check the function of adjacent amide hydrogen for the formation of metalated a-type fragment ions, ECD of Ni^{2+} adducted RGGGLGPGR, with one glycine replaced by proline, was performed. Because proline lacks an amide hydrogen, it is possible to inhibit the formation of corresponding a-ion. Figure 3.7 shows the relative intensities of various fragment ions generated in the ECD of Ni^{2+} adducted RGGGLGGGR and RGGGLGPGR. The length of the bars correlates linearly with the relative intensities of the fragment ions. It is clear that the original $[\bar{a}_7+Ni\text{-}H]^+$ observed in ECD of Ni^{2+} adducted RGGGLGGGR, has disappeared, while the other *a*-type fragment ions were still observed in the spectrum. In addition to the

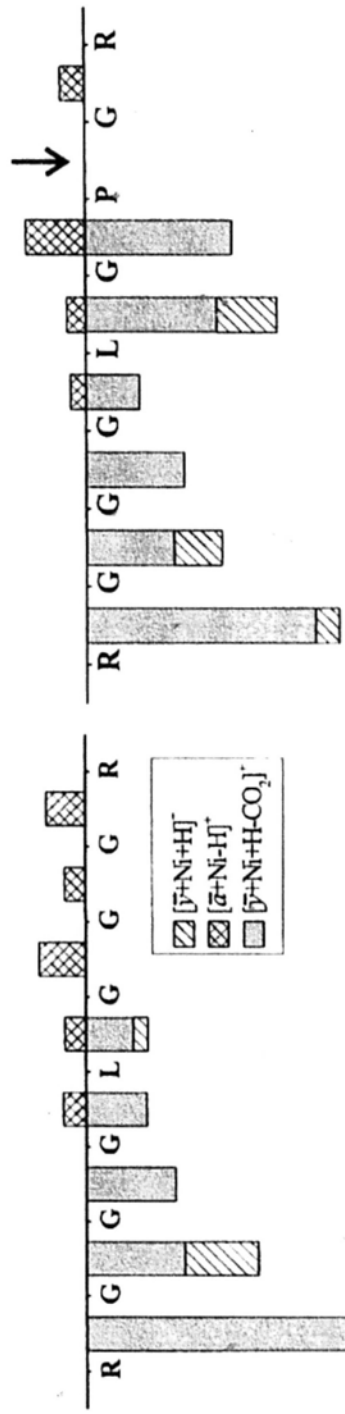

Figure 3.7 Relative intensity of various fragment ions in the ECD of Ni^{2+} adducted RGGGLGGGR and RGGGLGPGR.

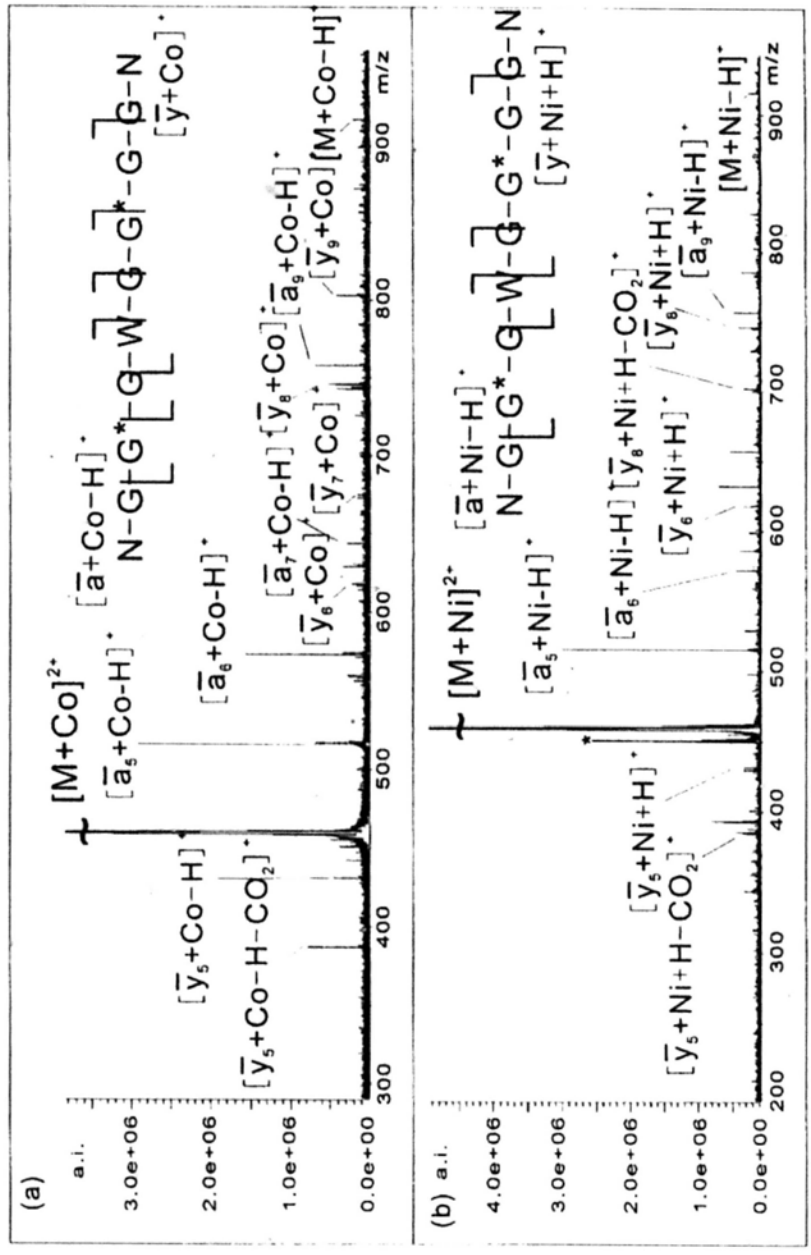

Figure 3.8 Typical ECD spectra of NG(Sar)GWG(Sar)GGN adducted with (a) Co^{2+} and (b) Ni^{2+}

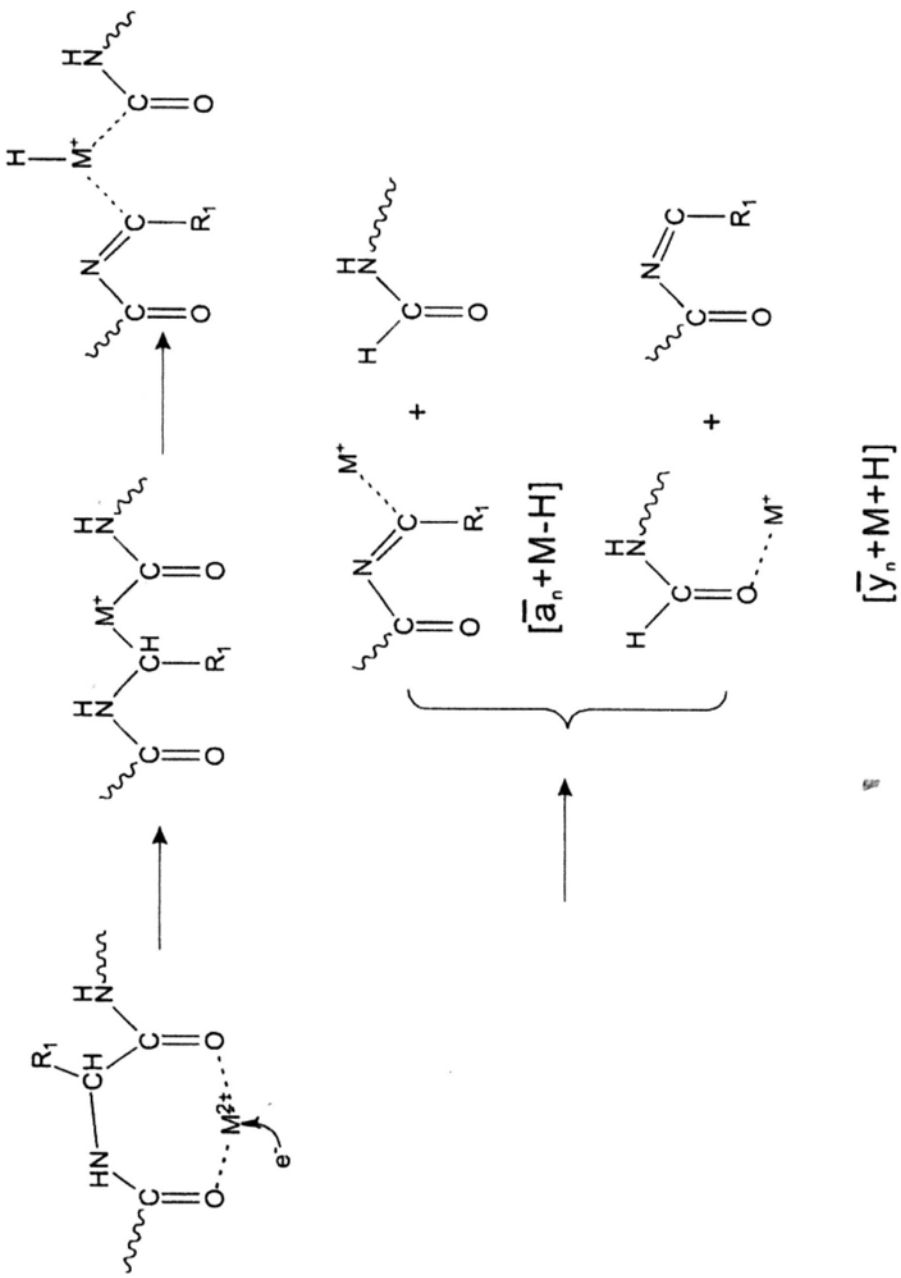

Scheme 3.2 Proposed mechanism for the formation of metalated *a*-/*y*-type fragment ions in the ECD of metalated peptides.

Scheme 3.3 Proposed mechanism for the formation of metalated *a*-type fragment ions in the ECD of metalated peptides.

proline substitution, the glycine amide nitrogen methylated amino acid (MeGly or Sarcosine G*) containing peptide, NGG*GWGG*GGN was used as an additional model. As shown in Figure 3.8, as expected, the corresponding *a*-and y-ions adjacent to the sarcosine residue disappeared in the ECD of the Ni^{2+} adducted peptide. These spectra indicate that the amide hydrogen might be essential during the formation of metalated *a*-type fragment ions in the ECD of Ni^{2+} adducted peptides. However, in the ECD spectrum of Co^{2+} adducted NGG*GWGG*GGN, the corresponding *a*- and *y*-ions were still observed and thus the detail mechanism for their formation needs further investigation.

Apart from the model peptides, we also studied the ECD behavior of metalated Bradykinin, RPPGFSPFR, as a representative for linear bio-active peptides. Similar to the observations obtained using model peptides, both metalated and non-metalated fragment ions were generated for all the selected metal ions except Cu^{2+} (Appendix III). The *c*-/*z*-type fragment ions formed by cleavage of N-terminus of proline residues and the metalated *a*-type fragment ions formed by cleavage the C-terminus C_α-C bond of proline residues were not observed due to the cyclic nature of the proline residues.

3.5 Conclusions

ECD of different divalent transition metal ions adducted model peptides generated different fragment patterns. Based on the ECD tandem mass spectra of a series of metalated model peptides, it is proposed that the electronic configurations of metal ions govern the ECD behavior of the corresponding metalated peptides. For Mn^{2+} and Zn^{2+} with half filled and fully filled d shells, respectively, the usual ECD fragmentation behavior of metalated peptides was rationalized by electron-proton recombination. For the other metal ions, including Fe^{2+}, Co^{2+}, Ni^{2+} and Cu^{2+}, with partially filled d shell, the formation of usual "slow-heating" type of fragment ions was caused by energy transfer to the metalated peptide after electron-metal ion recombination.

Chapter 4

Electron Capture Dissociation of Peptides Adducted with Group IIB Metal Ions: Formation of Peptide Radical Cations ($M^{+\bullet}$)

4.1 Introduction

To better understand the dissociation process(es) and to further improve the performance of the electron capture dissociation method, many researchers have studied the influence of various experimental parameters on the dissociation behavior of peptides/protein ions. An important experimental parameter is the nature of the charge carrier(s). Several researchers have studied the impact of replacing protons with fixed charges using functionalities such as quanternary amino groups. [156,157]. Our group and other researchers have focused on the use of divalent and trivalent metal ions as charge carriers. In practice, ECD with metal ions as charge carriers have been used to characterize O-sulfated tyrosine [133], petrobacin [134], metabolites [136], oligosaccharides [135], phosphocholines [157], supramolecular complexes [158], and dendrimers [159]. In Chapter 3, the effects of first row divalent transition metal ions adduction on the ECD of model peptides were investigated. Based on the experimental results, it was proposed that the electronic configuration of metal ions is an important parameter that affects the ECD behavior of metalated peptide.

This chapter aims to study the effect of adduction by Group IIB metal ions (Zn^{2+}, Cd^{2+}, and Hg^{2+}) on the ECD fragmentation of model peptides. Table 4.1 summarized the ionization energies and coordination chemistries of the three metal ions. Similar to Chapter 3, model peptides with a general framework of ZGGGXGGGZ, where X is either V or W; and Z is either R, K, H, were used in this study. The use of these model

Table 4.1 A summary of the physical and chemical information of Group IIB metal ions.

		1st IE [a]	2nd IE [a]	Electronic Configuration		Pauling Radius (Å)		Ionic Radius (Å)		
Element	Symbol	eV	eV	M^{2-}	M^{+}	M^{2+}	M^{+}	4-coordinated	6-coordinated	8-coordinated
Hydrogen	H	13.60	-	-	-	-	-	-	-	-
Zinc	Zn	9.39	17.96	$3d^{10}$	$3d^{10}4s^{1}$	0.74	0.88	0.74	0.88	1.04
Cadmium	Cd	8.99	16.91	$4d^{10}$	$4d^{10}5s^{1}$	0.97	1.14	0.92	1.09	1.24
Mercury	Hg	10.44	18.80	$5d^{10}$	$5d^{10}6s^{1}$	1.10	1.25	1.10	1.16	1.28

peptides, as opposed to the use of bioactive peptides, was to include residues that illustrate the types of mechanistic possiblity and to reduce the complexity of the spectra. Basic amino acids, R, K, and H were included in the model peptide to facilitate direct comparison of the ECD spectra of metalated peptides with the protonated analogues of different proton carriers. Glycine spacers were used to separate amino acid residues and to provide a molecular framework with high flexibility. Valine and tryptophan were included to alter the ionization energy of the peptides. The main goal of this chapter is to compare the ECD behavior of peptides cationized with transition metal ions having a fully filled d-shell.

4.2 Experimental

Sample preparation

All materials were obtained commercially and were used without further purification. Zinc (II) acetate was obtained from Riedel-de Haën (Seelze, Germany), Cd (II) nitrate and Hg(II) nitrate were obtained from Sigma and Aldrich (St. Louis, MO, USA). Model peptides were custom-synthesized by Peptron Inc., (Daejeon, South Korea). The samples were prepared at concentrations of $1 \times 10^{-4} - 2.5 \times 10^{-4}$ M in 1:1 water: methanol (Labscan Ltd., Bangkok, Thailand). The concentrations of the metal salts were 5 mM in peptide solutions.

Instrumentation

All experiments were performed on a 4.7 Tesla FTMS system (APEX III, Bruker Instrument Inc., Boston, MA). This instrument was equipped with a standard, commercially available external electrospray ion source (Analytica, Branford, CT). The ESI ion source was modified to adopt a homemade nanospray assembly. The detailed instrumental set up and ECD experimental conditions were given in Chapter 2 and 3.

Calculations

All calculations were performed using the Gaussian 03 package [110]. Equilibrium geometries were determined by full optimization followed by harmonic frequency calculations to confirm the nature of minima and transition states. All the stationary points were optimized at the level of B3LYP/LANL2DZ+6-31++G(d,p). Single point energy calculation were calculated at the B3LYP level in conjunction with LANL2DZ+6-311++G(3df,2p) basis set.

4.3 Results and discussion

4.3.1 ECD of Group IIB metal ions adducted RGGGWGGGR

Figure 4.1 (a-c) shows the ECD spectra of RGGGWGGGR adducted with Zn^{2+}, Cd^{2+}, and Hg^{2+}, respectively. The mass assignments of the ECD spectrum of Hg^{2+} adducted peptide are given in Table 4.2. Product ions are labeled according to our previously proposed nomenclature, in which $\overline{c}-$ and $\overline{z}-$ denotes the corresponding N- and C-terminal fragments originated from the homolytic cleavage of the N-C_α linkages, respectively. Any surplus of proton/hydrogen atom or metal ion/atom is indicated in the label [131]. Interestingly, peptides adducted with different Group IIB metal ions generated different ECD tandem mass spectra. Among the three metal ions studied, the ECD fragmentation of Zn^{2+} adducted RGGGWGGGR is similar to that of alkaline earth metal ions. Typical ECD fragment ions, i.e. *c*-/*z*-ions, with and without metal ions were generated. Even and odd electron side chain losses from the metalated *z*-ions could also be observed. The ECD spectrum of Cd^{2+} adducted model peptides is substantially different from that of Zn^{2+}. Only minor *c*-/*z*-ions with and without metal ions were observed. Abundant signals corresponding to the peptide radical cation ($M^{+\bullet}$) and its neutral loss fragment ions were observed in the ECD spectrum of Cd^{2+} adducted peptides. For Hg^{2+} adducted RGGGWGGGR, only one non-metalated *c*-ion was observed. The spectrum was dominated by fragment ions derived from neutral losses of

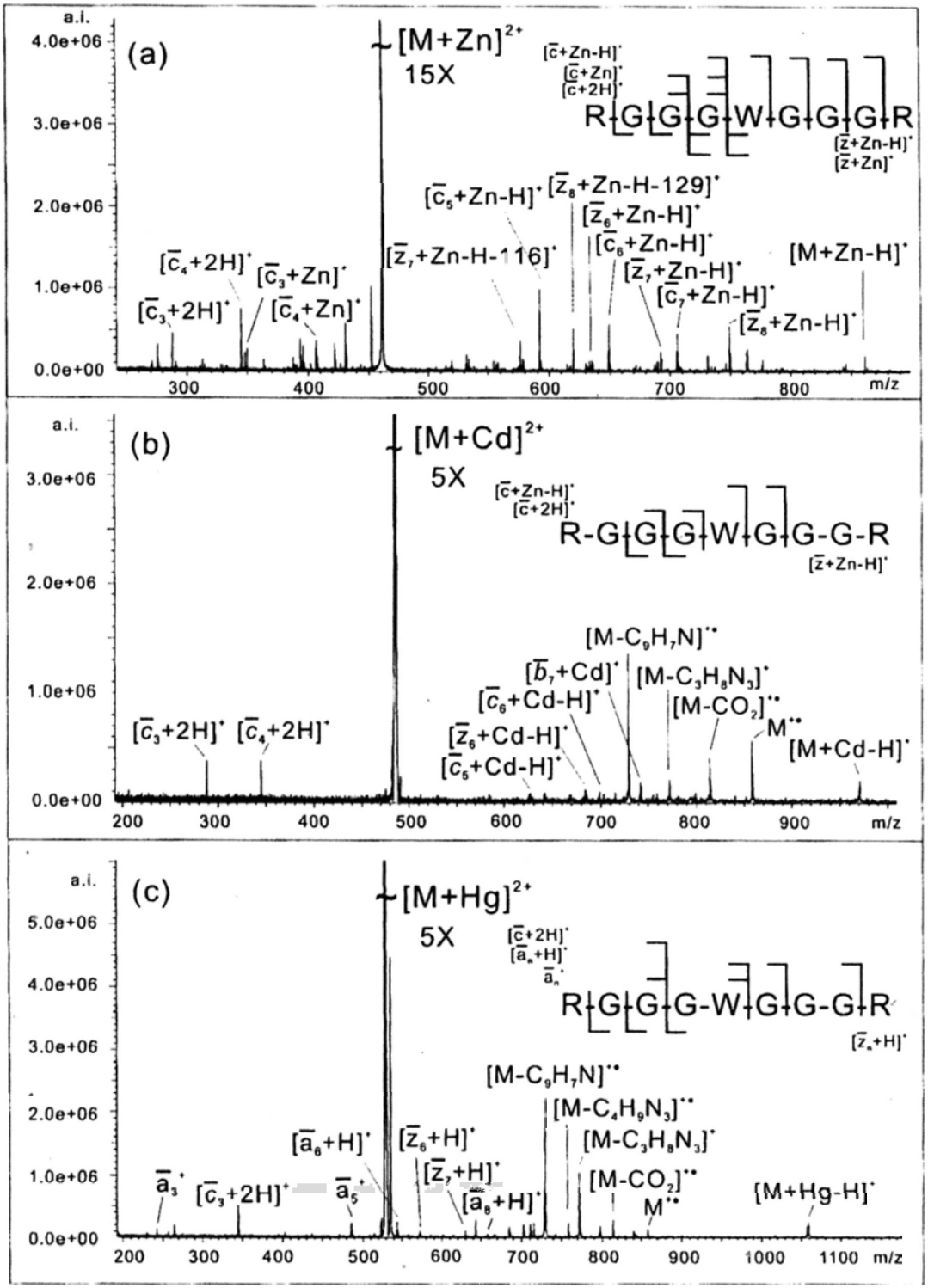

Figure 4.1 Typical ECD mass spectra of RGGGWGGGR adducted with (a) Zn^{2+}, (b) Cd^{2+}, (c) Hg^{2+}.

Table 4.2 Assignment of peaks in the ECD spectrum of RGGGWGGGR adducted with Hg^{2+}.

	Theoretical mass	Experimental Mass	S/N	Error in ppm
$[M+Hg-H]^{+}$	1059.3843	1059.3806	11.6	-3.5
$M^{+\bullet}$	858.4209	858.4258	6.3	5.8
$[M-CO_2]^{+\bullet}$	814.4310	814.4433	13.2	15.1
$[M-C_3H_8N_3]^{+}$	772.3485	772.3455	48.7	-3.8
$[M-C_4H_9N_3]^{+\bullet}$	759.3407	759.3361	10.7	-6.0
$[M-C_9H_7N]^{+\bullet}$	729.3624	729.3636	103.6	1.7
$[M-CO_2-C_3H_8N_3]^{+}$	728.3587	728.3547	35.9	-5.5
$[M-CO_2-C_4H_9N_3]^{+\bullet}$	715.3508	715.3458	11.0	-7.1
$[M-C_9H_7N-H_2O]^{+\bullet}$	711.3518	711.3414	10.0	-14.7
$[\bar{y}_8+2H]^{+}$	703.3270	703.3310	9.9	5.6
$[\bar{z}_8+H]^{+\bullet}$	687.3084	687.3129	2.7	6.5
$[M-CO_2-C_9H_7N]^{+\bullet}$	685.3726	685.3727	8.0	0.2
$[\bar{a}_8+H]^{+\bullet}$	658.3294	658.3311	3.4	2.7
$[\bar{z}_7+H]^{+\bullet}$	630.2868	630.2786	5.5	-13.1
$[\bar{z}_6+H]^{+\bullet}$	573.2654	573.2599	5.3	-9.6
$[\bar{a}_6+H]^{+\bullet}$	544.2864	544.2815	11.6	-9.1
$[M+Hg]^{2+}$	530.1958	530.1967	1121.4	1.6
$[\bar{a}_5+H]^{+\bullet}$	487.2650	487.2664	11.0	2.9
$\bar{a}_5^{+\bullet}$	486.2572	486.2586	10.5	2.9
$[\bar{c}_3+2H]^{+}$	345.1993	345.1990	23.8	-0.9
$\bar{a}_3^{+\bullet}$	243.1564	243.1573	6.9	3.6

Table 4.3 Summary of product ions abundance of ECD of ZGGGWGGGZ (Z=R, K, H) adducted with Group IIB metal ions.

		Zn^{2+}			Cd^{2+}			Hg^{2+}		
	n	R	K	H	R	K	H	R	K	H
$[M + Cat - H]^+$		4.5	2.9	7.9	3.7	7.5	6.0	3.1	2.0	7.2
$[\bar{c}_n + Cat - H]^+$	8	-	8.2	11.4	-	7.5	52.1	-	-	4.1
	7	5.8	5.1	1.8	-	4.5	3.4	-	3.6	
	6	7.2	7.6	4.1	2.5	2.9	5.1		2.1	-
	5	13.3	11.5	12.5	2.3	3.8	7.6			-
	4	11.6	22.5	17.9	-	4.1	8.1	-	-	-
	3	5.5	9.9	18.4	-	-	1.3	-	-	-
$[\bar{z}_n + Cat - H]^+$	8	8.0	-	3.3	-	-	-	-		-
	7	2.5	-	-	3.8	2.1	-	-	-	-
	6	1.9	5.7	7.2	2.9	2.0	3.4	-	-	-
	5	2.15	4.2	2.3	-	3.0	2.6	-	-	-
$M^{+\bullet}$		-	-	-	13.8	10.2	1.2	1.7	1.0	
$[M-CO_2]^{+\bullet}$		-	-		9.9	39.6	2.8	3.5	2.4	-
$[M-W_{Sc}]^{+\bullet}$		-	-	-	32.7	3.7	2.1	27.4	5.1	13.0
$[M-W_{Sc}-CO_2]^{+\bullet}$		-		-	-	-	-	2.1	-	5.6
$[M-Z_{Sc}^{\bullet}]^+$		-	-	-	18.3	-	-	15.6	8.5	7.8
$[M-Z_{Sc}^{\bullet}-CO_2]^+$		-	-	-	-	6.5	-	12.4	19.0	6.9
$[\bar{a}_n + H]^{+/\bullet}$	8	-	-	-	-	-	-	0.9		
	6	-	-	-	-	-	-	3.1	-	-
	5	-	-	-	-	-	-	6.8	15.4	17.6
	3	-	-	-	-	-	-	1.8	-	-
$[\bar{c}_n + 2H]^+$	7	-	-	-	-	-	-	-	2.2	-
	4	12.1	-	-	9.3	2.6	-	-	-	4.7
	3	7.8	-	-	9.3	-	-	6.3	-	-
$[\bar{z}_n + H]^{+\bullet}$	8	-	-	-	-	-	-	0.7	-	
	7	-	-	-	-	-	-	1.5	-	-
	6	-	-	-	-	-	2.1	1.4	-	-
	5	-	-	-	-	-	-	-	2.7	-
$[\bar{y}_n + 2H - CO_2]^+$	8	-	-	-	-	-	-	3.3	6.3	9.7
	7	-	-	-	-	-	-	1.2	3.8	16.1
	6	-	-	-	-	-	-	-	-	2.9
	5	-	-	-	-	-	-	1.4	-	-

$M^{+\bullet}$. A relatively weak signal corresponding to the peptide radical cation was observed.

Some non-metalated *a*-/z-type fragment ions were generated in the ECD spectra of Hg^{2+} adducted peptide. The ECD spectral information for metal ions adducted ZGGGWGGGZ (Z = K or H) were found to generate similar spectra as compared to that of RGGGWGGGR and are summarized in Table 4.3.

4.3.2 CID of Hg^{2+} and Cd^{2+} adducted peptides

The formation of peptide radical cation ($M^{+\bullet}$) is of fundamental and analytical importance. These ions have never been reported in the literature relevant to ECD of metal ions adducted peptides binary complex. A conceivable explanation for the formation of $M^{+\bullet}$ might involve an electron transfer (ET) reaction between the peptide and the divalent metal cation. This electron transfer process has previously be found to occur in the collision induced dissociation (CID) of metal-ligand-peptide ternary complexes [103-105], such as copper(II) terpyridine peptide complexes. In order to determine the role of the electron capture process in the formation of the peptide radical cations, CID of Cd^{2+} and Hg^{2+} adducted peptides were conducted using argon as collision gas. Figure 4.2 shows the CID tandem mass spectra of Cd^{2+} and Hg^{2+} adducted peptides. CID of Cd^{2+} adducted peptide generated primarily non-metalated b-ions; whereas CID of Hg^{2+} adducted peptide gave both metalated and non-metalated *b*-/*y*-ions. The absence of any y-ions and the formation of series of non-metalated b-ions in the CID spectrum of Cd^{2+} adducted peptide imply that Cd^{2+} binds preferentially to the C-terminal side of the peptide. The formation of $[M+Cd-60]^{2+}$ also supports this postulation. Loss of *m/z* 60 from the precursor ions of peptides containing C-terminal arginine residue has previously been investigated [160] and was assigned to be the concomitant loss of a H_2O and HN=C=NH moieties from the C-terminal carboxylic acid and the arginine side chain, respectively. Nevertheless, no evidence for the

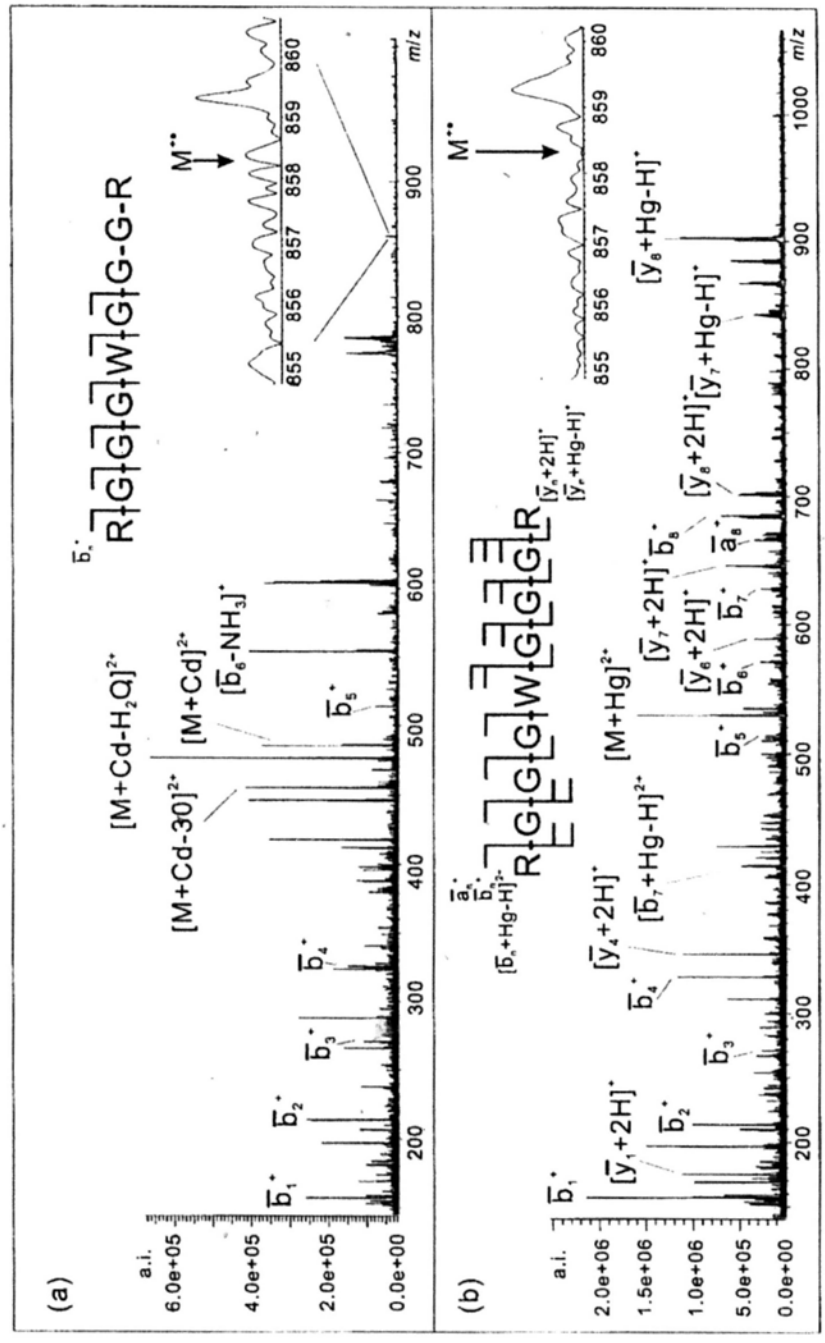

Figure 4.2 CID mass spectra of RGGGWGGGR adducted with (a) Cd^{2+}, (b) Hg^{2+}.

formation of the peptide radical cation $M^{+\bullet}$ and related fragment ions was found in both CID spectra. The absence of $M^{+\bullet}$ species in these CID spectra indicates that electron capture is a pre-requisite process for the electron transfer between peptides and metal.

4.3.3 Formation of peptide radical ion $M^{+\bullet}$ under ECD conditions

Since electron capture is an essential process for the formation of peptide radical cation ($M^{+\bullet}$) and its related species, it is logical to examine the feasibility of the electron transfer process between the monovalent Group IIB metal ions and the peptide molecules. Theoretically, the energetics of the electron transfer reaction is governed by:

$$\Delta H_{et} = R.E.(Cat^{+}) - I.E.(M) \qquad (4.1)$$

where $R.E.(Cat^{+})$ is the recombination energy of the monovalent metal ion with electron and I.E.(M) is the ionization energy of the peptide. Ignoring the effect of coordination environment of metal ion, the $R.E.(Cat^{+})$ is equal to the first ionization of the metal atom. Table 4.1 summarizes some related physical properties of Group IIB elements. The first ionization energies for Hg, Cd and Zn are 10.44 eV, 8.99 eV and 9.39 eV, respectively. As compared with that of the amino acid residue having the lowest I.E., i.e. tryptophan (I.E. = 7.24 eV) [161], it is obvious that electron transfer from the peptide moiety to any of the monovalent Group IIB metal ions is energetically feasible.

In the literature, the phenomenon of electron transfer from gas phase organic molecules to monovalent metal ions has been examined extensively [162-165]. Bohme and coworkers [164] found that Hg^{+} and Zn^{+} can undergo charge transfer reaction with benzene (I.E = 9.24 eV) in gas phase leading to the formation of $[C_6H_6]^{+\bullet}$ species. In a comprehensive study of the reactivity of Hg^{+}, Bohme and coworkers [165] concluded that Hg^{+} can ionize organic molecules with ionization energy lower than 10.1 eV. Herein, we proposed that the peptide radical cation $M^{+\bullet}$ was generated through an "electron capture induced spontaneous electron transfer" model. Reduction of the metal

ion by the incoming electron generates the monovalent metal ions peptide complex, $[M+ Cat(I)]^+$. If the recombination energy of monovalent metal ion is larger than the ionization energy of peptides, the system is likely to relax spontaneously and access the $[M^{\bullet+} + Cat(0)]^+$ state via electron transfer from peptide to metal monocation. Without any charges in the metal centre, the metal-peptide complex would dissociate to give the observed $M^{+\bullet}$.

4.3.4 Influences of amino acid residues in the peptides

To get more information relating to the charge transfer behavior of Group IIB metal ions under electron capture dissociation conditions, another model peptide with similar peptide framework, i.e. RGGGVGGGR, was examined. By replacing the tryptophan residue with a valine residue, the ionization energy of the peptide should increase to a value close to the ionization energy of arginine residue (i.e. I.E = 9.20 eV) [166]. Figure 4.3(a-c) shows typical ECD spectra of divalent Group IIB metal ion adducted RGGGVGGGR. With adduction of Zn^{2+} and Hg^{2+} species, the spectral behavior of RGGGVGGGR shows high similarities with respect to that of RGGGWGGGR under ECD conditions. ECD of Zn^{2+} adducted RGGGVGGGR gave exclusive *c-/z*-type fragment ions; whereas ECD of Hg^{2+} adducted RGGGVGGGR gave mainly $M^{+\bullet}$ and related species. An interesting feature of the ECD spectrum of Hg^{2+} adducted RGGGVGGGR is the fewer number of fragment ions arising from the backbone cleavages. Consistent with the expected lowering of the energy release through the charge transfer reaction between the peptide moiety and the Hg^+ ion, i.e. R.E. (Hg^+) – I.E. (RGGGVGGGR), the extent of backbone cleavage was substantially reduced. From the ECD spectrum of the Cd^{2+} adducted RGGGVGGGR, it is interesting to find that no peptide radical ions ($M^{+\bullet}$) and related species were generated. The ECD spectrum is dominated by non-metalated and metalated *c-/z*-type fragment ions. Cross

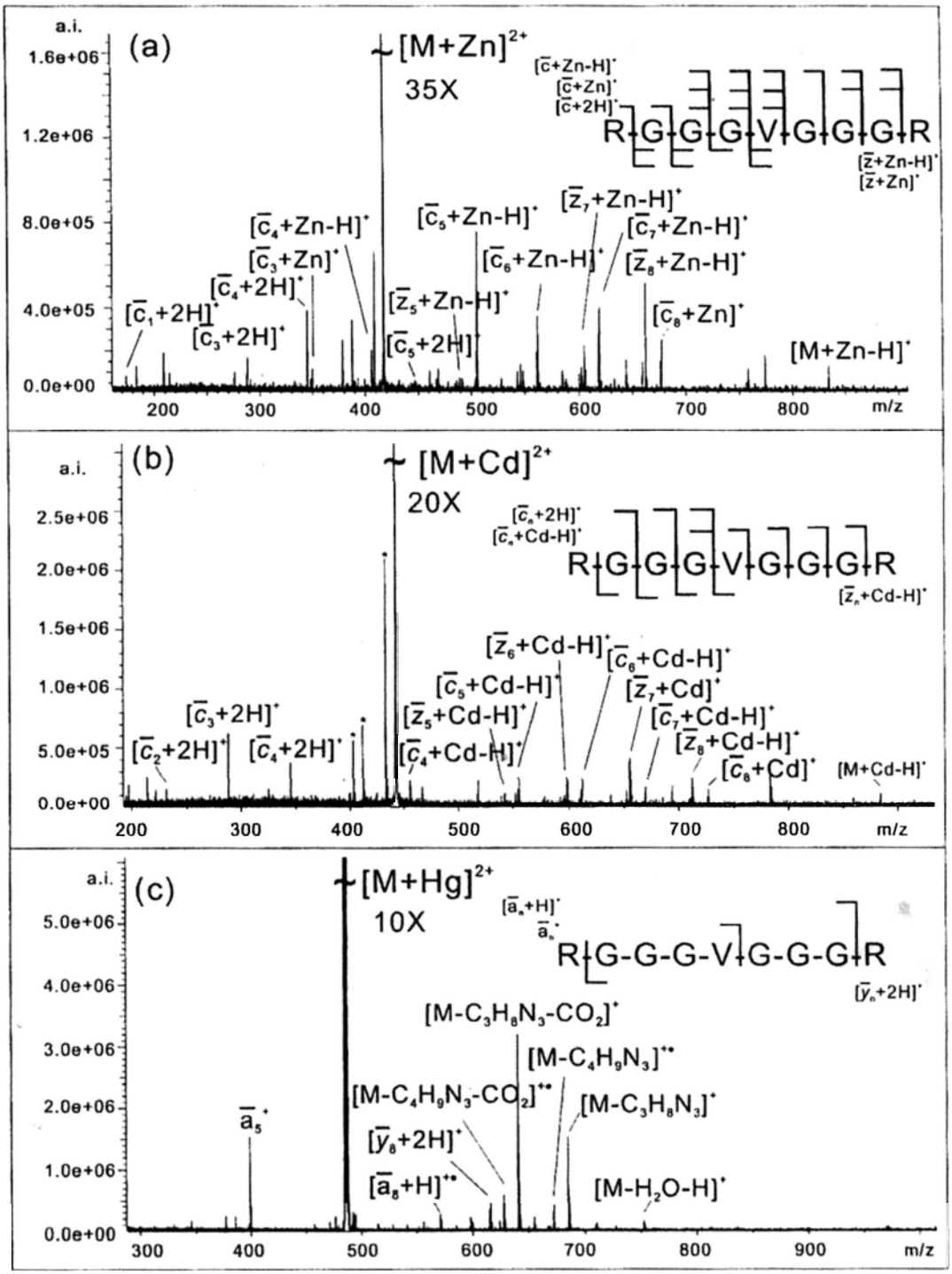

Figure 4.3 Typical ECD mass spectra of RGGGVGGGR adducted with (a) Zn^{2+}, (b) Cd^{2+}, (c) Hg^{2+}.

comparing the ECD spectra of RGGGVGGGR and RGGGWGGGR obtained with Cd^{2+} adduction (Figure 1b and 3b), it is intriguing to note that the initial ionization site of the peptide can lead to the remote loss of radical fragments. Since there is no apparent charge transfer reaction between the RGGGVGGGR moiety and the charge-reduced Cd^{+}, it is therefore logical to postulate that ionization of RGGGWGGGR by the charge-reduced Cd^{+} proceeds primarily through the transfer of an electron from the tryptophan side chain to the Cd^{+}. Losses of odd-electron arginine side chains (see Figure 4.1 (b)) from the $RGGGW^{+\bullet}GGGR$ must therefore proceed via a rearrangement reaction involving the migration of the radical centre from the tryptophan side chain to the arginine residue. Scheme 4.1 shows a possible reaction mechanism for side chain(s) loss in the ECD of RGGGWGGGR adducted with Cd^{2+}. Similar to the reaction process involving the loss of arginine side chain from the z-ions, the indole radical cation might abstract the C_α hydrogen in the arginine residue to form a distonic ion, i.e. the charge resides on the typtophan side chain and the radical is located at the C_α of the arginine residue. The radical site would induce the formation of C_α=C_β double bond with concomitant loss of the $[C_3H_8N_3]^{\bullet}$ through the cleavage of the C_β-C_γ linkage. For tryptophan side chain loss, proton abstraction from NH of tryptophan side chain by arginine separates the charge and radical, then homolytic cleavage C_α-C_β bond can lead to the loss of $[C_9H_7N]$.

4.3.5 The effect of solvation energy

A major discrepancy arising from the current experimental results and the theoretical prediction is related to the ECD behavior of Zn^{2+} adducted peptides. From Table 4.1, the 1st ionization energy of Zn is ~0.4 eV higher than Cd. If the driving force of the electron transfer reaction between the peptide moiety and the monovalent metal ions is solely related to their I.E. and R.E. respectively, Zn^{2+} adducted peptides should

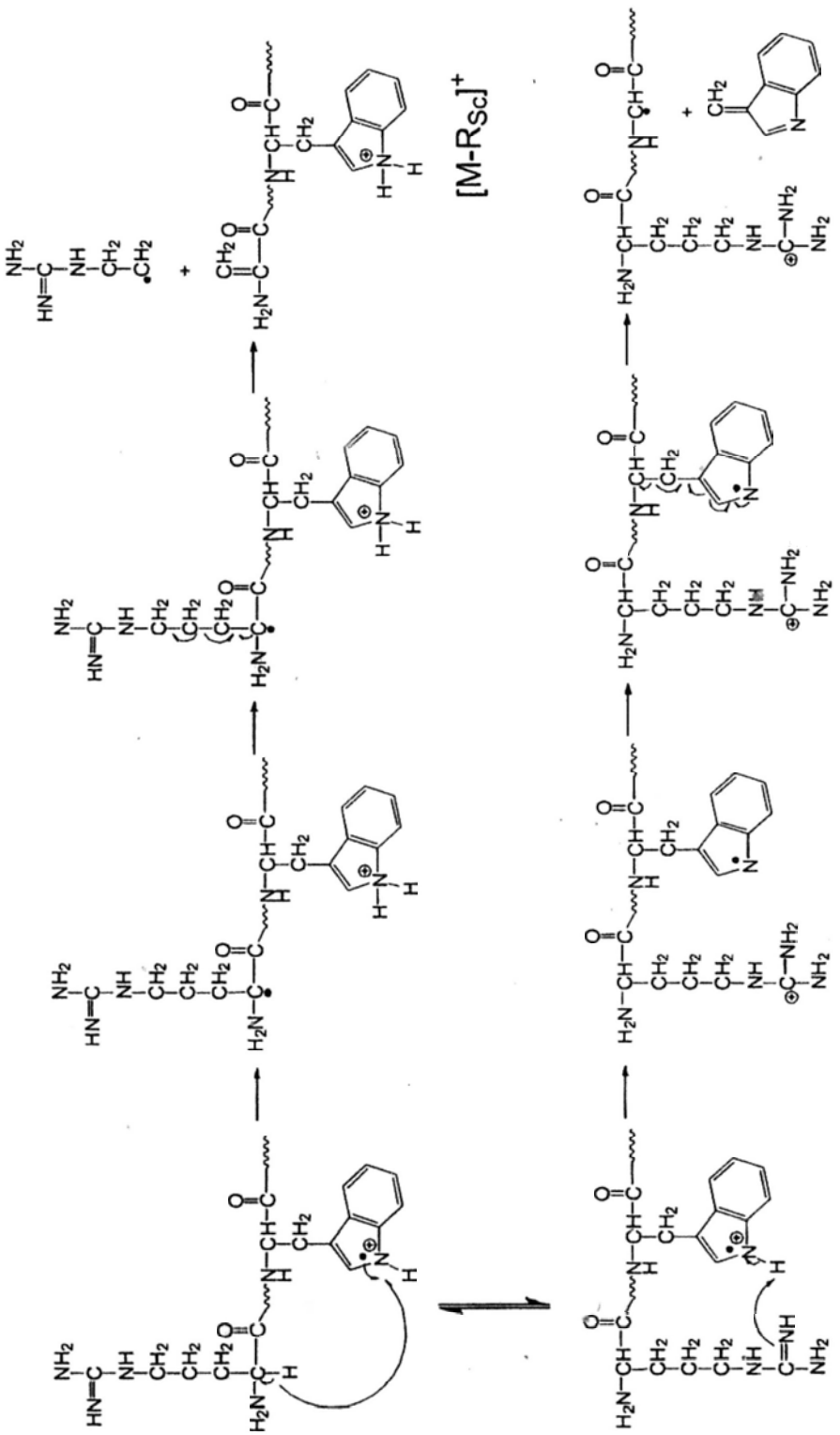

Scheme 4.1 A proposed mechanism for side chain(s) loss in the ECD of RGGGWGGGR adducted with Cd^{2+}.

show a spectral behavior similar to that of the Cd^{2+} adducted peptides or even approaching to that of the Hg^{2+} adducted peptides, i.e. at least the ECD of spectrum of Zn^{2+} adducted RGGGWGGGR should contain the peptide radical cation! In the study of the gas phase reactions between monovalent transition metal ions and benzene, Bohme and co-workers demonstrated [164] that electron transfer reaction can actually occur in Hg^{+}/benzene and Zn^{+}/benzene systems but not the Cd^{+}/benzene system. The latter could presumably be explained on the basis of the higher ionization energy of benzene (versus tryptophan residue). However, both our experimental results and literature reports demonstrate that ECD of Zn^{2+} adducted peptides gives only typical metalated and non-metalated *c*-/*z*-type fragments. Regardless of the ionization energy of the peptide moiety, no peptide radical cation or its related species could be observed.

One way to explain the observed discrepancies is related to the solvation modulation of the recombination energy of the transition metal ions. In the metal ion adducted peptide systems, the transition metal ions should be coordinated by the polar functionalities of the peptide moiety, such as the carbonyl oxygen and arginine side chains. Reduction of the metal ions from their monovalent states to the neutral states would drastically alter the ion solvation. Part of the ion-electron recombination energy would therefore be used to compensate the change in the solvation energy. The equation governing the electron transfer should therefore be modified as:

$$\Delta H_{ct} = \text{R.E.}(Cat^{+}) - \text{I.E.}(M) - \text{solvation energy} \qquad (4.2)$$

The order of solvation energies for monovalent Group IIB metal ions should be inversely proportional to the size of the metal ions (see Table 4.1). It is therefore possible that the inclusion of the solvation energy term might "toggle" the energetics of the charge transfer reaction from spontaneous to non-spontaneous for Zn-system but not for the other group IIB metal systems. A better understanding on the solvation of monovalent metal ions by the peptide moiety is needed to evaluate this hypothesis.

4.3.6 The role of precursor ion heterogeneity

On top of the perturbation of solvation energy on the electron transfer reaction, the heterogeneity of the precursor ions might also play an important role in governing the resulting spectral features of these Group IIB metal ion adducted peptides. Previous experimental and theoretical studies of metal ion-peptide complexes have shown that the metal ion can induce deprotonation of the amide functional groups of peptides [142-145] and generate different forms of zwitterions. To gain additional insights into the effect of Group IIB metal ions coordination on the deprotonation reaction of the amide group, theoretical calculation using N-methyl glycyl-glycinamide as a truncated peptide model was investigated.

Scheme 4.2 shows the potential energy curves of deprotonation reaction mediated by Zn^{2+}, Cd^{2+}, and Hg^{2+}, respectively. The optimized structural parameters and energies for the reactants, transition states and products are tabulated in Table 4.4 and Table 4.5. The stationary points (A, $TS_{A\text{-}B}$, and B) adopt a conformation in which the metal ion (Cat^{2+}) was bi-coordinated by the carbonyl oxygen atoms. As shown in Scheme 4.2, the Zn^{2+} mediated intramolecular proton transfer from the amide to the N-terminal amino group is almost thermo-neutral (ΔH = +1.6 kJ mol^{-1}) and has a fairly low activation barrier (E_{TS} = +15.1 kJ mol^{-1}). In the presence of high proton affinity functionalities, the gas phase Zn^{2+} coordinated moieties should, therefore, adopt a zwitterionic form in which the backbone amide group(s) and /or the C-terminal carboxylic acid group are deprotonated, and the basic functionalities are protonated. Three tautomers, with a general formula $[(M + Cat^{2+} - nH^{+})^{(2-n)+} + nH^{+}]^{2+}$ (n = 0, 1, and 2), should exist in the precursor ions.

After establishing the existence of mobile proton(s) in the precursor ions, it is time to reconsider the recombination processes. Beside the metal ion-electron recombination, the mobile proton-electron recombination might constitute the second neutralization

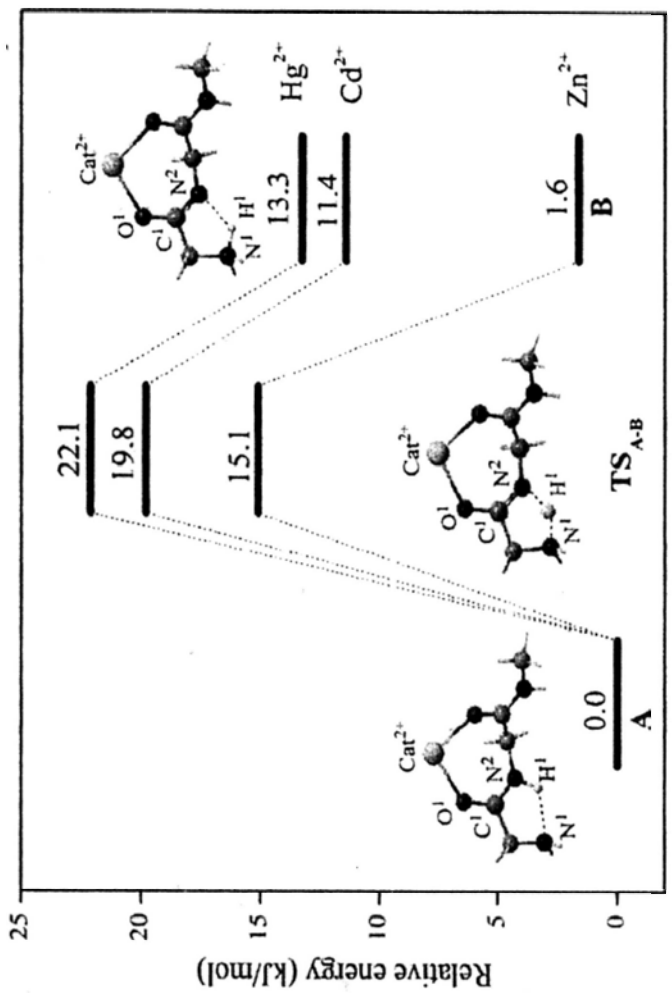

Scheme 4.2 Potential energy surfaces associated with the deprotonation reactions of Zn^{2+}, Cd^{2+}, and Hg^{2+} adducted N-methyl glycyl-glycinamide. Single point energy calculated at the B3LYP/LANL2DZ+6-311++G(3df,2p) based on the structures optimized at B3LYP/LANL2DZ+6-31++G(d,p) level. The scale factor for ZPE is 0.961.

Table 4.4 Optimized bond distances (Å) for the reactants, transition states and products involved in the deproronation reaction at the B3LYP/LANL2DZ+6-31++G(d,p) level.

	Zn^{2+}			Cd^{2+}			Hg^{2+}		
	A	**TS_{A-B}**	**B**	**A**	**TS_{A-B}**	**B**	**A**	**TS_{A-B}**	**B**
$R(H^1\text{-}N^1)$	1.938	1.318	1.050	1.954	1.292	1.054	2.003	1.292	1.053
$R(H^1\text{-}N^2)$	1.041	1.288	1.912	1.038	1.310	1.868	1.033	1.309	1.874
$R(C^1\text{-}O^1)$	1.286	1.297	1.320	1.278	1.290	1.310	1.268	1.287	1.309
$R(C^1\text{-}N^2)$	1.323	1.303	1.286	1.326	1.305	1.290	1.328	1.305	1.289
$R(Cat^1\text{-}O^1)$	1.901	1.894	1.883	2.113	2.107	2.092	2.253	2.219	2.198

Table 4.5 Calculated energies *E*, zero-point energies *ZPE*, total energies E_{total} (in hartrees) and relative energies (in kJ/mol)calculated at the B3LYP/LANL2DZ+6-31++G(d,p) level and single point energies calculation at B3LYP/LANL2DZ+6-311++G(3df,2p)// B3LYP/LANL2DZ+6-31++G(d,p) level.

		B3LYP/LANL2DZ+6-31++G(d,p)				B3LYP/LANL2DZ+6-311++G(3df,2p)		
Metal	Species	*E*	*ZPE*	E_{total}[a]	ΔE	*E*	E_{total}[a]	ΔE
Zn^{2+}	**A**	-576.927667	0.179432	-576.755233	0.0	-577.093291	-576.920857	0.0
	$\mathbf{TS_{A-B}}$	-576.920089	0.176084	-576.750872	11.5	-577.084333	-576.915116	15.1
	B	-576.928188	0.180288	-576.754931	0.8	-577.09352	-576.920263	1.6
Cd^{2+}	**A**	-559.391811	0.178768	-559.220014	0.0	-559.553593	-559.381797	0.0
	$\mathbf{TS_{A-B}}$	-559.382382	0.175444	-559.213781	16.4	-559.542864	-559.374262	19.8
	B	-559.388425	0.179518	-559.215908	10.8	-559.549968	-559.377451	11.4
Hg^{2+}	**A**	-554.031896	0.178044	-553.860796	0.0	-554.193138	-554.022038	0.0
	$\mathbf{TS_{A-B}}$	-554.021686	0.174844	-553.853661	18.7	-554.181655	-554.01363	22.1
	B	-554.027949	0.178959	-553.855969	12.7	-554.188966	-554.016987	13.3

[a]Scale factor for *ZPE* is 0.961

channel for the incoming electron. Along this channel, the hydrogen radical would be formed, and induce typical ECD fragmentation, leading to the formation of *c*-/*z*-ions and $[M + Cat - H]^+$. Because of the lower energy needed for Zn^{2+} mediated deprotonation reaction, it is believed that the proton-electron recombination prevails over the metal ion-electron recombination. Fragment ion species derived from this reaction channel should resemble those derived from typical ECD of protonated peptides, i.e. mostly *c*-/*z*-type fragment ions.

For Cd^{2+}/peptide system, the energy barrier of deprotonation was found to be higher than that of Zn^{2+} (E_{TS} = +15.1 kJ/mol). The reactions are calculated to be more endothermic, ΔH = +11.4 kJ/mol. The population of zwitterionic conformers in precursor ions should then be much lower than that of Zn^{2+} containing systems. For ECD of Cd^{2+} adducted peptide, it is believed that the metal ion reduction should be more competitive with respect to the proton-electron recombination. The simultaneous occurrence of both *c*-/*z*-type fragment ions and $M^{+\bullet}$ related species in the ECD spectra of Cd^{2+}/peptide systems supports a notion that metal ion reduction and proton-electron recombination are competitive processes. For the Hg^{2+} adducted model, the deprotonation is calculated to be even more unfavorable than for the Cd^{2+} adducted case. Considering the highest electron transfer reactivity of mercury mono-cation, it is believed that the metal ion-electron recombination is dominant in the electron recombination process. That is consistent with the experiment observations.

4.3.7 Dissociation model of ECD of peptides adducted with Group IIB metal ions

Scheme 4.3 summarizes the reactions in the ECD of Group IIB metal ion adducted model peptides. It is believed that there are two reaction channels within the metalated peptide ions upon the capture of a low-energy electron, i.e. metal ion reduction and electron-proton recombination. The choice of the reaction channel is determined by the

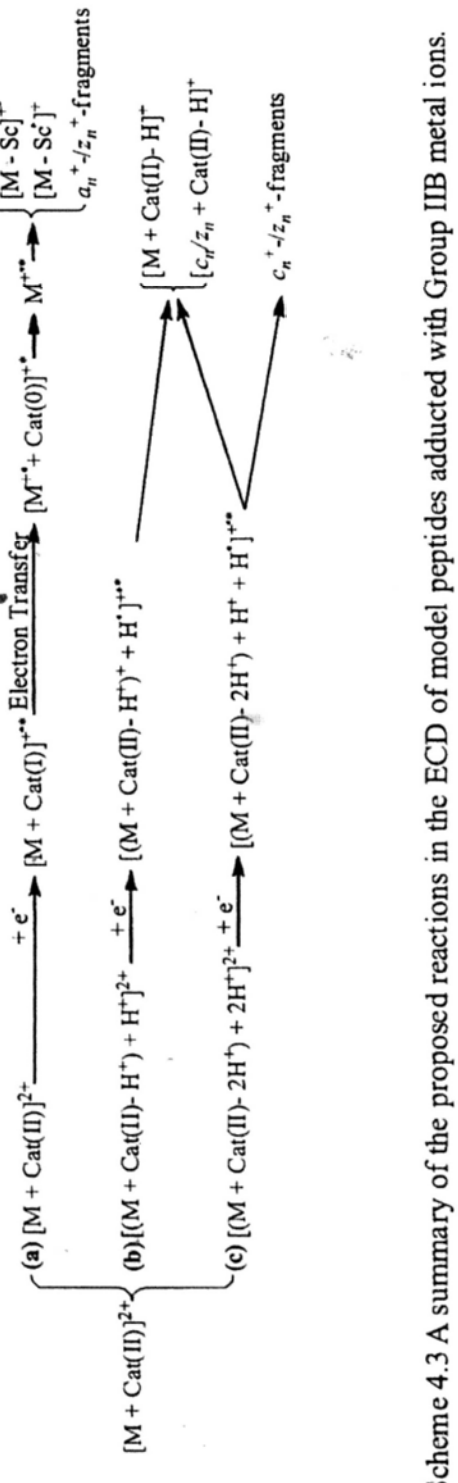

Scheme 4.3 A summary of the proposed reactions in the ECD of model peptides adducted with Group IIB metal ions.

ability of metal ion to promote deprotonation of the amide functional groups upon complexation to the peptide. If the metal ion does not promote deprotonation and the solvation modulated recombination energy of the monovalent metal ion is larger than the ionization energy of the peptide, the reaction would take place along the upper branch. Electron capture induced spontaneous electron transfer would occur. The $M^{+\bullet}$ and related fragment ions would be preferentially formed. This situation is best illustrated in the ECD of Hg^{2+}/peptide system. In contrast, if the metal ion promotes deprotonation of the amide functional groups and/or the solvation modulated recombination energy of the monovalent metal ion is lower than the ionization energy of the peptide, the reaction would take place along the lower branch to from the usual labile ketylamino radical. Subsequent decomposition of this intermediate would lead to the metalated and/or non-metalated c-/z-type fragment ions. This situation is best illustrated in the ECD of Zn^{2+}/peptide system. If the metal ion has a moderate ability to promote deprotonation, and the solvation modulated recombination energy of the monovalent metal ion is higher than the ionization energy of the peptide moiety, both reaction channels would be operative and generate an ECD spectrum containing both *c-/z*-type fragment ions and $M^{+\bullet}$ (and related fragment ions), i.e. ECD of Cd^{2+}/RGGGWGGGR system. Selecting a peptide moiety with higher ionization energy, i.e. RGGGVGGGR, the charge-transfer reaction between the peptide moiety and the monovalent metal ion might become energetically unfavorable. The corresponding ECD spectrum would then be dominated by the classical *c-/z*-fragment ions.

4.4 Conclusions

Electron capture dissociation of model peptides with Group IIB metal ions as charge carriers reveals interesting fragmentation chemistry. Typical ECD fragment ions were observed in the ECD of peptides adducted with Zn^{2+}. Peptide radical cations $M^{+\bullet}$

and related fragment species were observed in the ECD of model peptides adducted with Cd^{2+} or Hg^{2+}. Based on these distinctive reaction products, it is postulated that both electron-proton recombination and metal-ion reduction processes could be operate. The relative proportion of these processes depends on kinetic factors (i.e. the number density of the zwitterionic form of the precursor ions) and/or the thermodynamic factors (i.e. the solvation-modulated electron-metal ion recombination energy). Regardless of the controlling factor, the reduction of divalent metal ions by the electron capture event could induce spontaneous electron transfer from the peptide moiety to the monovalent metal centre and generate hydrogen-deficient $M^{+\bullet}$ species. Depending on the overall reaction exothermicity, the $M^{+\bullet}$ species might be formed with substantial internal energy and undergo further decomposition to give structural specific information.

Chapter 5

Effect of Tyrosine Nitration on the ECD of Protonated and Metalated Peptides

5.1 Introduction

As an important post-transitional modification, protein tyrosine nitration (PTN) has drawn much attention in the past years [167-169]. Previous research indicated that nitration of tyrosine can affect enzyme catalytic rates, protein-protein interactions, and phosphor-tyrosine signaling pathways [170]. About 60 human disorders, such as Parkinson's disease and Alzheimer's disease, have been observed in connection with protein mutation including tyrosine nitration [171]. As shown in Scheme 5.1, PTN is usually formed by addition of a nitro group (NO_2) onto one of the two equivalent carbons of the aromatic ring in *ortho* position to the phenolic hydroxyl group.

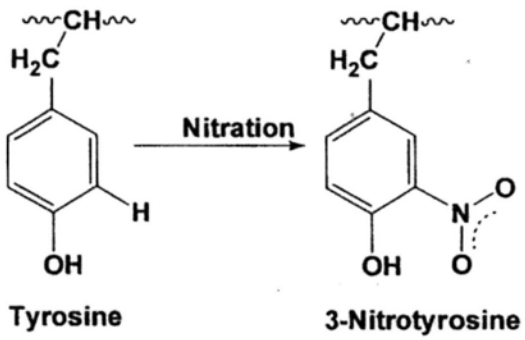

Scheme 5.1

In *vivo*, the formation of nitration in tissues may arise from the nitric oxide-derived oxidation products such as nitrogen dioxide ($^{\bullet}NO_2$), peroxynitrite ($ONOO^-$), or its CO_2 adduct, nitrosoperoxo-carbonate [172,173]. The abundance of tyrosine in proteins is around 3-4 mol%. However, PTN does not occur at random. A previous study indicated that most of the tyrosine residues modified by nitration were surface exposed [174]. It is still challenging to predict the target for PTN of a given protein. Therefore, detection of

nitrated proteins as well as localization of the nitrated tyrosine in the protein become increasingly necessary.

Many methods developed so far focus on the detection of nitrotyrosine-containing proteins and peptides [175-179]. For example, the characteristic ion pattern observed in MALDI spectra might be used as a diagnostic pattern for identification of nitrated peptides. However, the lability of the nitro group would result in a distribution of signals for nitrated peptides over several peaks with a concomitant reduction in sensitivity for observation of such peptides.

By addition of electron affinity (EA)-tunable tags to cysteine residue, Beauchamp and co-workers [180] found that ECD fragmentation was inhibited for peptides with high electron affinity tag such as 3-nitrobenzylcysteine (EA=1.00 eV) and 3, 5-dinitrobenzylcysteine (EA=1.65 eV). These authors proposed that similar effects would occur in the ECD of nitrated tyrosine containing peptides. Later, Cooper *et al.* investigated the ECD and CID behavior of 3-nitrotyrosine containing peptides [181]. It was found that the ECD fragment ions were inhibited by tyrosine nitration in the doubly protonated peptides. For triply protonated peptides, some fragment ions were observed. The authors suggested that ECD of nitrated peptides should produce backbone fragments when the charge of precursor is > N+2, where N= number of nitrotyrosines. However, the CID behavior is unaffected by the presence of tyrosine nitration. Consecutive *b*-/*y*-ions with the PTM intact on the tyrosine were observed. Recently, these same authors investigated tyrosine nitration by top-down mass spectrometry and concluded that the ECD can be used in top-down analysis of nitrated proteins [182]. In a more recent paper [183], they investigated the origin of ammonia loss by comparing the ECD fragmentation of peptides with/without basic amino acid residues and concluded that ammonia loss is derived from the N-terminal of basic amino acid containing peptides.

In this chapter, the ECD of doubly, triply and quadruply protonated SERCA2a segments were studied. These experimental results along with theoretical results provided some new insights into the ECD of nitrated tyrosine containing peptides. Beside real peptides, the ECD of some metal ion adducted model peptides with nitrated tyrosine were also investigated to explore the behavior of metal ion adducted tyrosine nitrated peptides under ECD conditions. Finally, the interactions of nitrated phenol with first row transition metal ions as a model of metal ion-nitrated tyrosine side chain binding were calculated by DFT methods.

5.2 Experimental

Sample preparation

The nitrated peptides SERCA2a 121-131 ($E_nYEPEMGKV_nYR$), SERCA2a 111-131 (RNAEDAIEALKE$_n$YEPEMGKVYR), SERCA2a 291-297 (GAI$_n$Y$_n$YFK), RGGG$_n$YGGGR ($_n$Y= nitrated tyrosine) and their unmodified analogues were commercially synthesized by Peptron Inc., (Daejeon, South Korea). The samples were prepared at concentrations of $1 \times 10^{-4} - 2.5 \times 10^{-4}$ M in 1:1 water: methanol (Labscan Ltd., Bangkok, Thailand). The concentrations of the metal salts were 5 mM in peptide solutions. All materials were obtained commercially and were used without further purification.

Instrumentation

All experiments were performed on a 4.7 Tesla FT-ICR MS (APEX III, Bruker Instrument Inc., Boston, MA). The detailed instrumental arrangements are illustrated in Chapter 2. In ECD experiments, the electron beam was produced by a standard electrically-heated filament source. Typical experimental conditions were 3.15 A filament heating current, 3.68 V average filament bias voltage and 300 ms electron

irradiation time. 30-50 scans were summed up to improve the signal-to-noise ratio.

Calculations

The structural features of nitrated tyrosine containing peptides were calculated using MacroModel program (v5, Schrödinger Inc., Portland, OR). Generally, energy minimizations of the model systems were performed by Truncated Newton-Raphson Conjugate Gradient (TNCG) method. The conformational search was conducted using the Monte Carlo [116] method with a random variation of all bonds. Low-energy conformers were found in 5000 steps and structures with energies not higher than 50 kJ/mol of the lowest-energy structures were stored. The truncated nitrated tyrosine containing model peptides were built for further high level calculations. The geometries of the truncated model systems were optimized at the B3LYP/6-31++G(d,p) [111-113] level. The vertical electron affinities and recombination energies of the model systems were calculated without geometry relaxation. In the calculation of metal ion-nitrated phenol interaction, the basis set 6-311+G(d) was used for the transition metal ions and the basis set 6-31++G(d,p) was used for the non-metal elements. All quantum mechanical calculations were performed by Gaussian 03 [110] under the Linux environment using Orion in the ITSC of CUHK.

5.3 Results and Discussion

5.3.1 Effect of tyrosine nitration on the ECD of protonated peptides

Figure 5.1 shows the ECD spectra of doubly protonated SERCA2a 121-131 and SERCA2a 291-297 before and after single nitration. For the unmodified peptides, typical ECD fragment ions, including *c*-/*z*$^{\bullet}$- ions and side chain losses from $z^{+\bullet}$-ions, were observed. For the nitrated peptides, instead of ECD fragment ions, neutral losses from the charge reduced precursor ion $[M+2H]^{+\bullet}$ dominate in the spectra. As reported earlier [182,183], the neutral species are different combinations of $OH^{\bullet}$, H_2O and NH_3. In order to test the effect of number of nitrated tyrosines, ECD of triply protonated

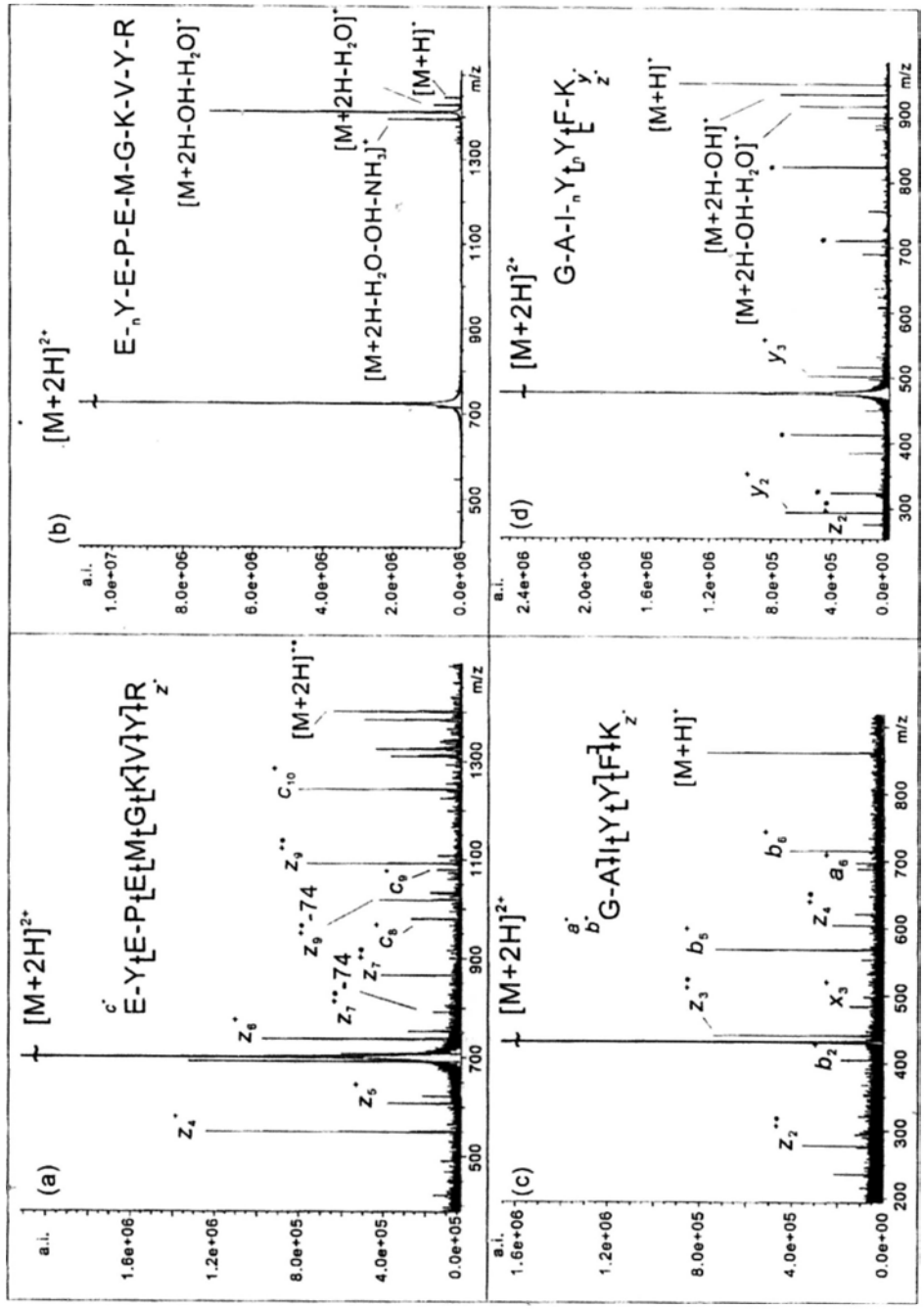

Figure 5.1 Typical ECD spectra of doubly protonated SERCA2a 121-131and 291-297 with and without tyrosine nitration

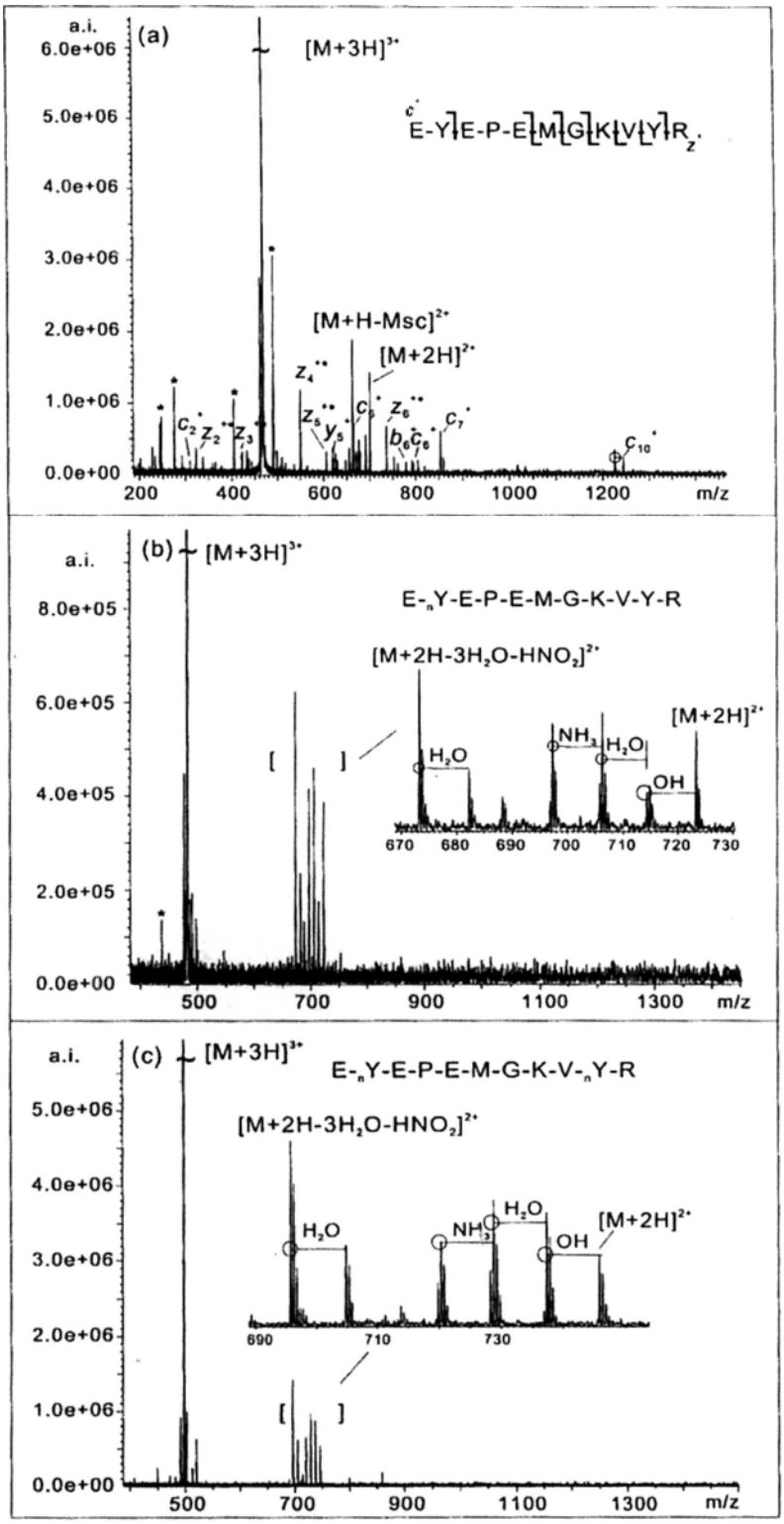

Figure 5.2 Typical ECD spectra of triply protonated SERCA2a 121-131(a) without nitrated tyrosine; (b) with a nitrated tyrosine residue; and (c) with two nitrated tyrosine residues.

SERCA2a 121-131 with no tyrosine nitration, one nitrated tyrosine residue, and two nitrated tyrosine residues were performed. As shown in Figure 5.2 (a-c), similar to the case of doubly protonated peptides, the ECD fragment ions are completely inhibited. The main ions arose from neutral losses from the charge reduced precursor ions. In addition to the usual neutral losses, peaks corresponding to losses of the combination of HNO_2 (or $NO^{\bullet}$+ $OH^{\bullet}$) and H_2O from the charge reduced precursor ions were observed for triply charged SERCA2a peptides containing either a singly nitrated tyrosine residue or tow nitrated tyrosine residues.

To further test the effects of charge states, ECD of triply protonated and quadruply protonated SERCA2a 111-131 were investigated and the corresponding spectra are shown in Figure 5.3 (a-d). For the unmodified peptides, extensive backbone fragment ions were generated. Only one minor *c*- ion was observed in the ECD spectra of single nitrated triply protonated peptide ions. For the quadruply protonated analogue, five minor fragment ions were generated. The main ions observed in these spectra are neutral losses ($OH^{\bullet}$) from the singly charge reduced and doubly charge reduced precursor ions. The appearance of neutral loss from doubly charge reduced precursor ions clearly indicated the occurrence of secondary electron capture during the electron capture process. In contrast, no doubly charge reduced precursor ions were observed for peptides lacking a nitrated residue. Double resonance (DR) experiment with ejection of doubly charge reduced precursor ion was performed for quadruply protonated SERCA2a 111-131 to check the role of this intermediate in the formation of backbone fragment ions. Four of the five fragment ions generated in experiment without DR disappeared, which indicated that these ions were formed by secondary electron capture. However, different from the previous results of Cooper and coworkers [181], the usual ECD fragment ions were still greatly suppressed by the inclusion of single tyrosine nitration as compared with the normal peptides lacking a nitrated residue.

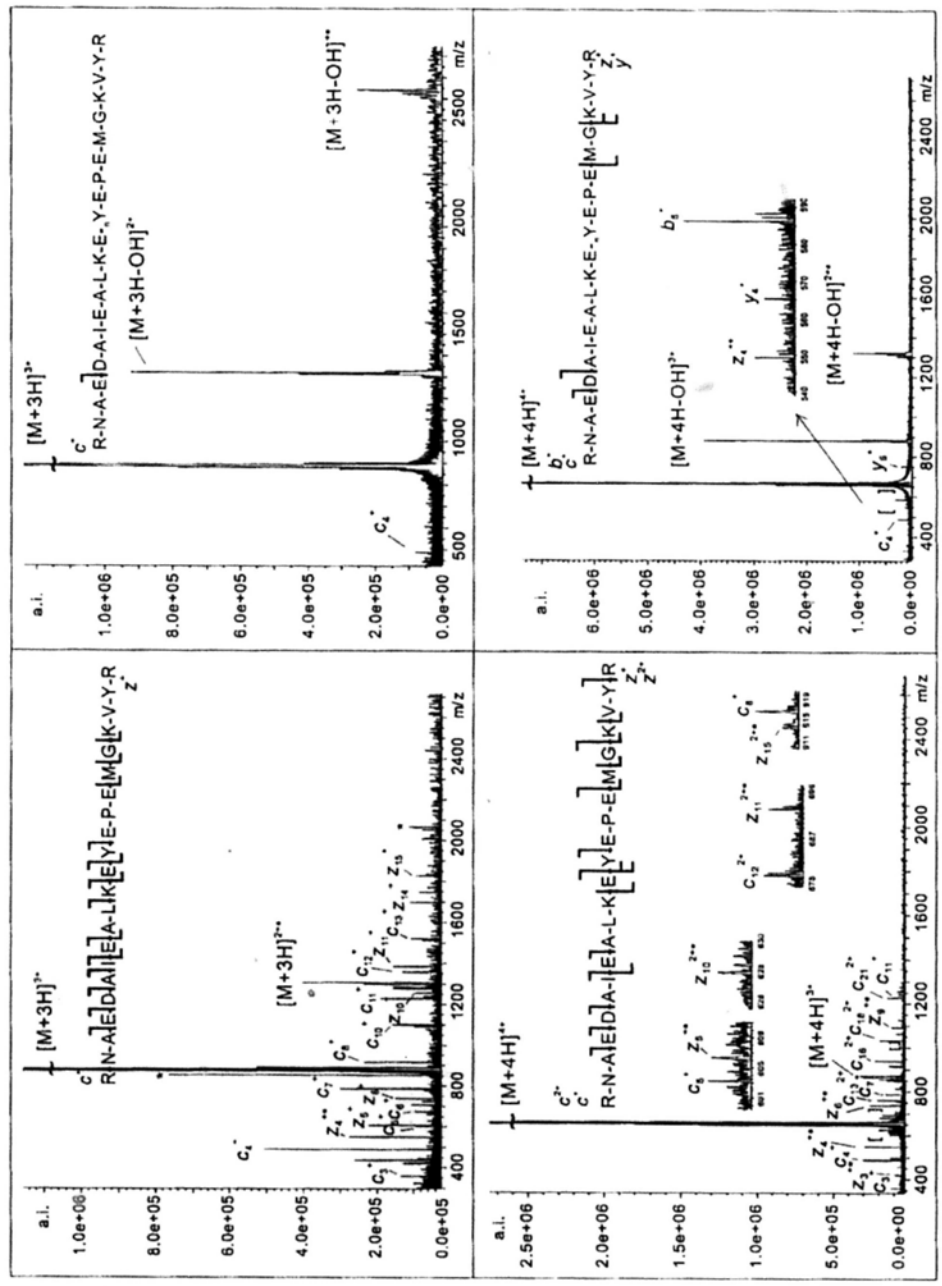

Figure 5.3 Typical ECD spectra of triply and quadruply protonated SERCA2a 110-131 with and without tyrosine nitration

5.3.2 Theoretical calculations

5.3.2.1 Molecular Mechanical conformational search

Figure 5.4 and 5.5 show the representative structures of triply protonated and doubly protonated SERCA2a 121-131 ions, respectively. For the doubly protonated species, both canonical and zwitterionic forms of the precursor ions were considered. Because of the complexity of the system, it was not possible to fully explore and examine the stabilities of the full structures by using DFT methods. As a result, the structures obtained here by conformational search might not represent the most stable species. However, the low energy structures reported here should provided useful information for a qualitative discussion of the experimental observations.

For the triply protonated species, the three protons were placed on the N-terminal, side chains of lysine (K) and arginine (R) residues. The most stable structure (a) features a hydrogen bonding interaction between the protonated guanidine group of R and nitro group of nitrated tyrosine residue (Y). Another low energy structure (b) is stabilized by hydrogen bonding between the N-terminal amine protonated and the nitro group of Y. For the doubly protonated species, the zwitterionic structures were found to be more stable than the canonical structures. In the stable zwitterionic species, as shown in Figure 5.5 (a), the nitro group forms hydrogen bonds with both the protonated side chains of K and R. In addition, a salt bridge is formed between the deprotonated C-terminal carboxyl group and the protonated N-terminal amine group. Compared with the triply protonated species, the doubly protonated species folds more tightly. A representative canonical structure obtained from conformational search is shown in the Figure 5.5 (b). In this structure, the protons are placed on the side chains of the two basic amino acid residues (K and R). The hydroxyl group of the nitrated tyrosine residue interacts with the protonated guanidine group of R. Energetically, the canonical structures are roughly 60-100 kcal/mol less stable than the zwitterionic structures.

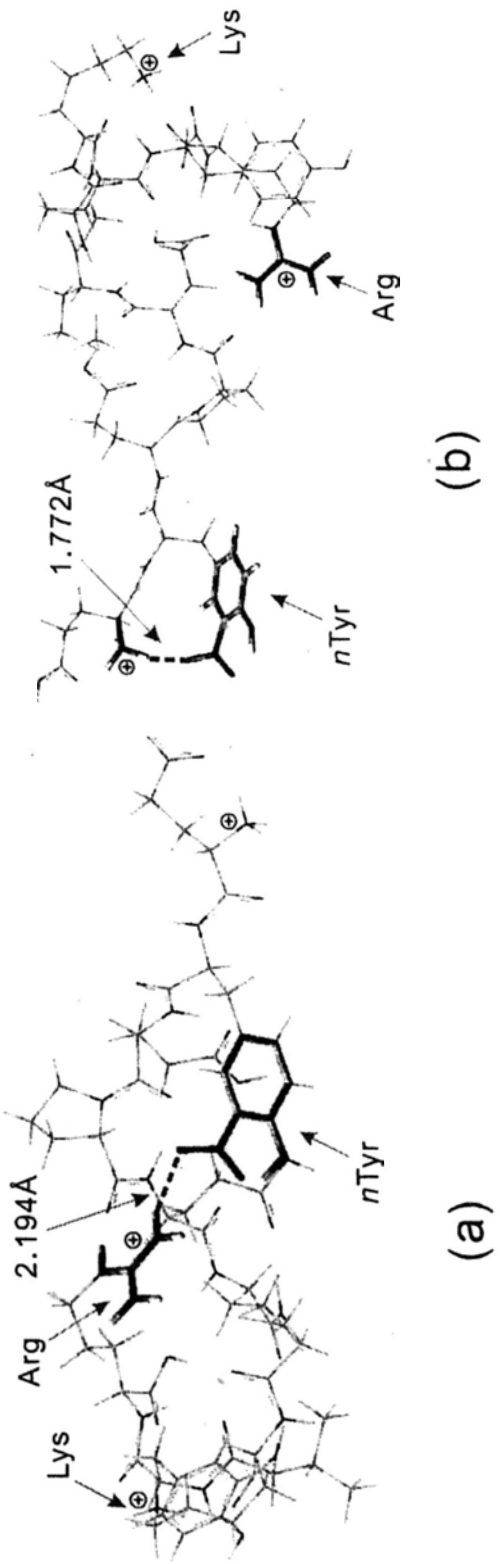

Figure 5.4 Representative low energy structures of $[E_nYEPEMGKVYR+3H]^{3+}$.

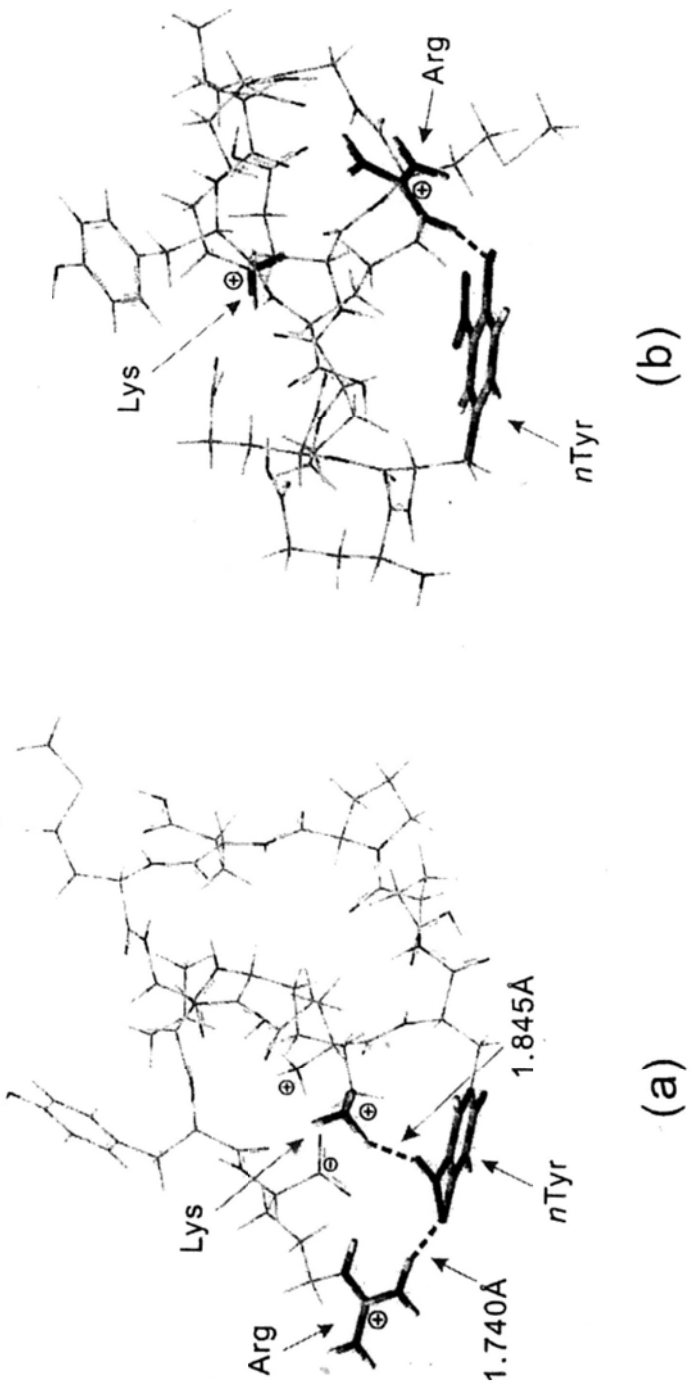

Figure 5.5 Representative low energy structures of $[E_n YEPEMGKVYR+2H]^{2+}$.

Based on the Boltzmann distribution, the contribution of canonical structures to the population of various structures of precursor ions should be much smaller than that of zwitterionic structures. For both the triply protonated and doubly protonated structures, the hydrogen bonding interactions between the protonated functional group and the nitrated tyrosine might facilitate the intra-molecular transfer of proton or hydrogen atom to the nitro group during/or after the electron capture event.

5.3.2.1 DFT calculation of truncated model

To further explore the mechanism of fragmentation suppression induced by tyrosine nitration in the ECD process, a truncated model peptide (Structure **1** in Figure 5.6) consisting of a nitrated tyrosine side chain and a backbone amide linkage was built for DFT calculation. The proton affinity (PA), electron affinity (EA) and hydrogen atom affinity (HA) of truncated model peptides were summarized in Table 5.1. The calculated proton affinity of nitro oxygen is about 45 kJ/mol smaller than that of the carbonyl oxygen. Both of them are much smaller than that of guanidine group of arginine. This implies that nitration of tyrosine should not alter the protonation sites of the peptides. The hydrogen atom affinity of the nitro oxygen is about 130 kJ/mol larger than that of carbonyl oxygen. It implies that the "hot" hydrogen as proposed in the "Cornell mechanism" may be tied down by the nitro group in the side chain of nitrated tyrosine. After establishing the role of nitro group in trapping the hot hydrogen radical, the energetics of neutral loss ($OH^{\bullet}$) from the nitrated tyrosine and that of the N-C_{α} bond cleavage in the truncated model peptide were examined. As shown in Figure 5.7, the energy barrier for N-C_{α} bond cleavage is higher than that of N-O bond cleavage. This is consistent with the experimental observations, where $OH^{\bullet}$ loss is much more abundant than *c*-/*z*-ion formation.

Based on the Utah-Washington mechanism and the "electron predator" model,

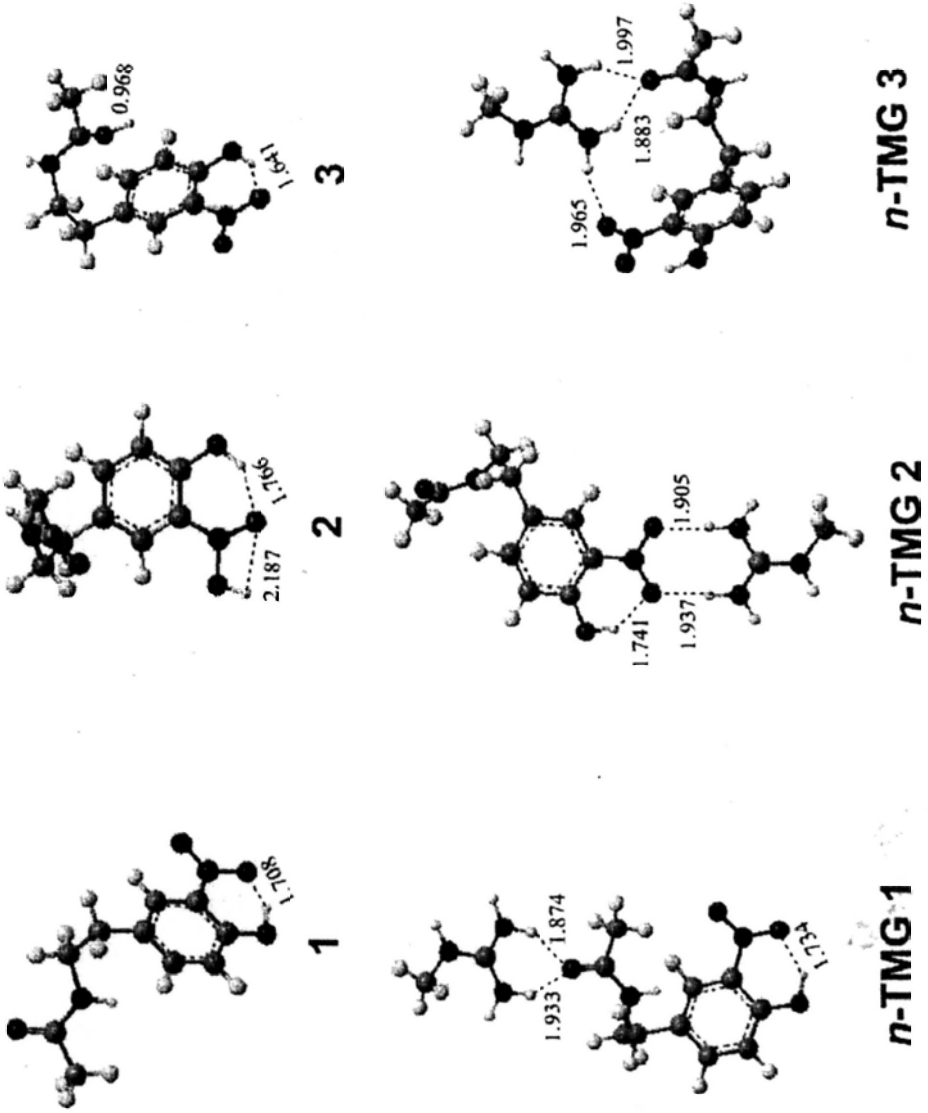

Figure 5.6 Optimized structures of the truncated model peptides at the level of B3LYP/6-31+G(d,p)

Table 5.1 Calculated HA, PA and EA of truncated model peptides at the B3LYP/6-31++G(d, p) level of theory.

	Normal tyrosine	Nitration tyrosine	Carbonyl Oxygen	Nitro Oxygen	Nitroso Oxygen
EA (eV)	-0.26 (-0.19)[a]	1.11 (1.91)[a]	--	--	--
PA (kJ/mol)	--	--	887.0	841.9 (1320.4)[b]	--
HA (kJ/mol)	--	--	46.5	188.0	228.0

[a] Adiabatic electron affinity in parentheses.

[b] Proton affinity of nitro group of negativly charged truncated model peptide.

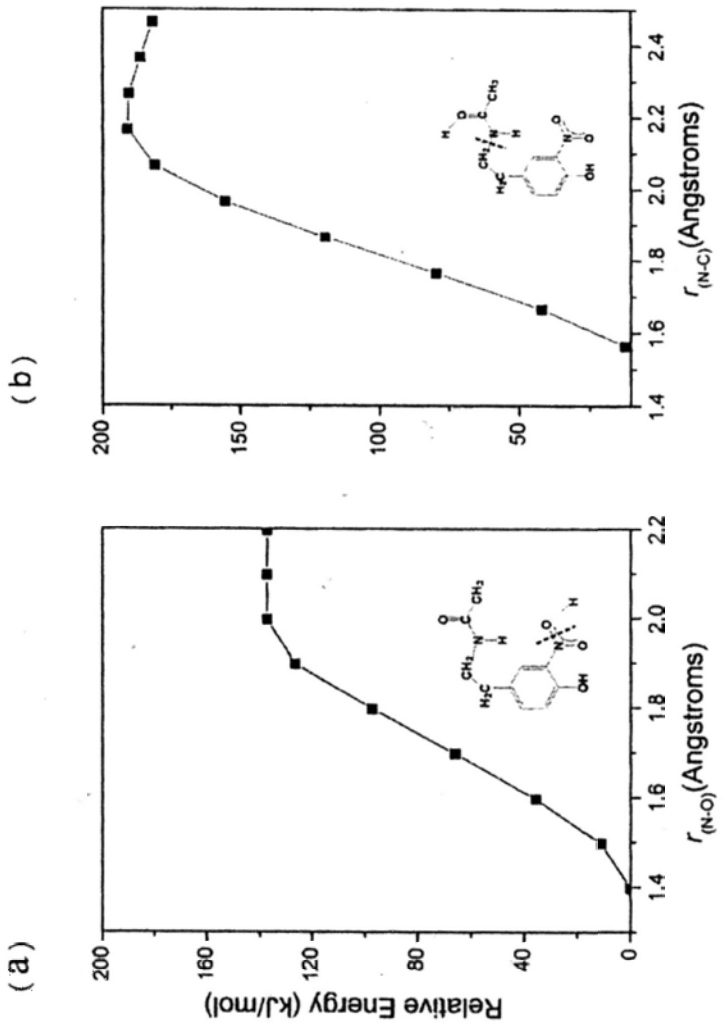

Figure 5.7 Potential energy profiles along the (a) N-O(H) coordinate in model **2** and (b) backbone N-C coordinate in model **3** calculated at the level of B3LYP/6-31++G(d,p).

the initial location and relaxation of the incoming electron may be altered by the presence of a higher electron affinity tag. Here, a model peptide including protonated methyl guanidinium and nitrated tyrosine was built to explore the location of the unpaired electron in the ground state using the DFT method. Considering the possible interactions between protonated groups and the nitrated tyrosine residue from conformational searches, three bonding modes between the protonated guanidinium and nitrated tyrosine were calculated. As shown in Figure 5.6, in *n*-TMG1, there is no direct interaction between the nitrated tyrosine and the protonated methyl guanidinium. The protonated methyl guanidinium interacts with the backbone carbonyl oxygen. The *n*-TMG2 involves two hydrogen bonds between the nitro group and protonated methyl guanidinium. In the *n*-TMG3, the protonated methyl guanidinium interacts with both the nitro oxygen and backbone oxygen. This structure shows the highest similarity to the geometrical optimized structures as obtained from the previous conformational search. In all cases, the ground state singly occupied molecular orbital (SOMO) of the charge reduced model systems was found to localize mainly on the nitro-phenolic π^* orbital, rather than the usual s orbital around the methyl guanidinium group as shown in Figure 5.8.

In a previous study, Cooper and coworkers observed ECD backbone fragments if the charge of precursor was > N+2, where N= number of nitrotyrosines in the peptides [181]. However, only a few fragment ions were observed in the ECD of tyrosine nitrated SERCA2a 111-131 (triply protonated and quadruply protonated) as shown in Figure 5.3. During the ECD process, a second electron would be captured by the charge reduced preeursor ions or the species corresponding to $OH^{\bullet}$ loss from charge reduced precursor ions. It is believed that the second electron captured by charge reduced precursor ions might be responsible for inducing typical ECD fragmentation. In our peptides, instead of the ECD fragment ions, only the $[M+nH-OH^{\bullet}]^{(n-2)+\bullet}$ which were

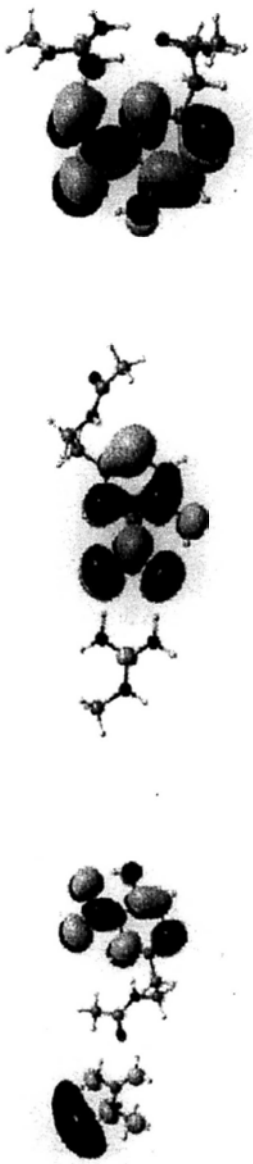

Figure 5.8 Single occupied molecular orbital (SOMO) of truncated model peptides.

formed by second electron capture, were observed. It indicated that the $[M+nH-OH^{\bullet}]^{(n-2)+\bullet}$ might formed by second electron capture of $[M+nH-OH^{\bullet}]^{(n-1)+}$. After the $OH^{\bullet}$ loss, a nitroso (NO) modified tyrosine containing peptides would be formed as the precursor ions for consecutive electron capture. Therefore, it was proposed that the typical dissociation channels of hydrogen-surplus radical cation $[M+nH-OH^{\bullet}]^{(n-2)+\bullet}$ were inhibited by the nitroso (NO) modified tyrosine containing peptides. Similar to that of nitro modified tyrosine, the higher HA of a nitroso (NO) modified tyrosine group (228.0 kJ/mol in Table 1) would trap the newly generated hot hydrogen radical that formed by secondary electron capture. Thus it would continue to suppress ECD fragmentation.

In summary, the ECD fragmentations of protonated peptides were largely suppressed by a single tyrosine nitration. The stepwise hydrogen radical trapping by nitro (NO_2) and nitroso (NO) groups in the modified tyrosine residues and the low energy barrier for $OH^{\bullet}$ involved neutral loss were believed to be responsible for the unusual ECD behavior of nitrated tyrosine containing peptides.

5.3.3 ECD of metal ion adducted peptides containing nitrated tyrosine

In the last two chapters, the effects of metal ion adduction on the ECD of model peptides were studied. A clear "tuning effect" on the fragmentation was observed by addition of different transition metal ions. In this section, ECD of Cu^{2+}, Fe^{2+} and Hg^{2+} adducted nitrated tyrosine containing model peptides were investigated. The selection of these three metal ions was based on their unique ECD behaviors. For example, typical CID fragment ions were observed in the Cu^{2+} adducted peptides; different types of fragment ions were observed in the ECD of Fe^{2+} adducted peptides with and without basic amino acid residue; and peptide radical cation was generated in the ECD of Hg^{2+} adducted peptide. To simplify the spectra as well as data interpretation, a model peptide with the sequence RGGGYGGGR was used.

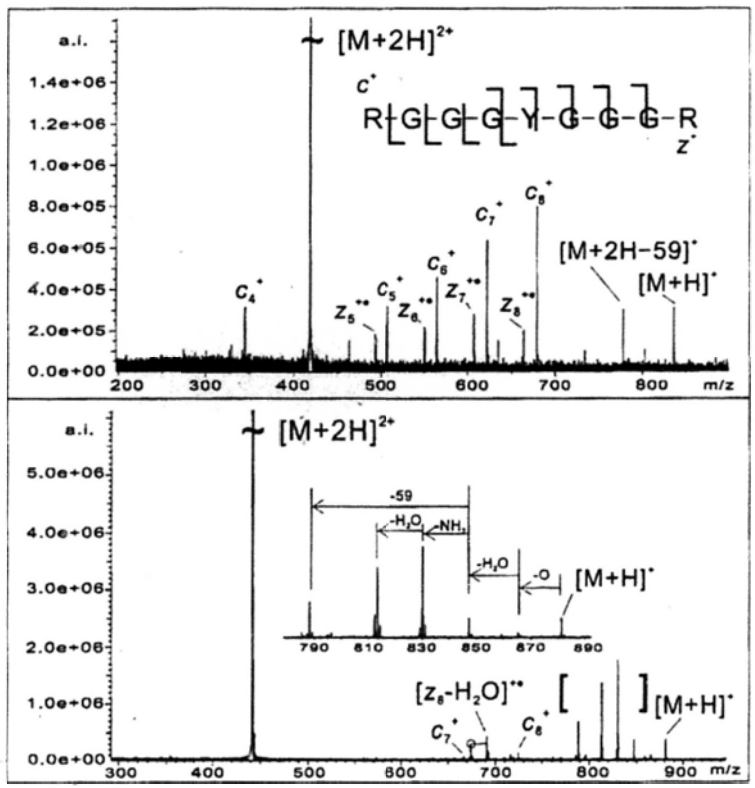

Figure 5.9 Typical ECD spectra of doubly protonated RGGGYGGGR with and without tyrosine nitration.

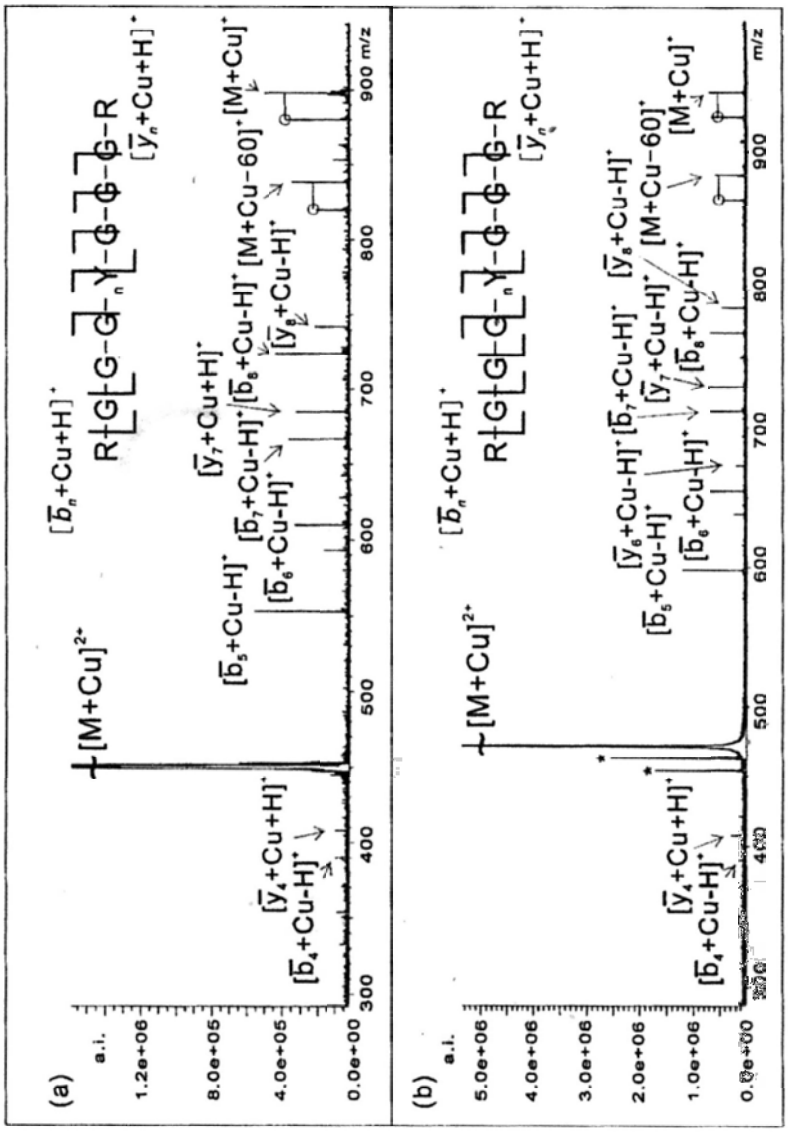

Figure 5.10 ECD spectra of Cu^{2+} adducted RGGGYGGGR and RGGGnYGGGR.

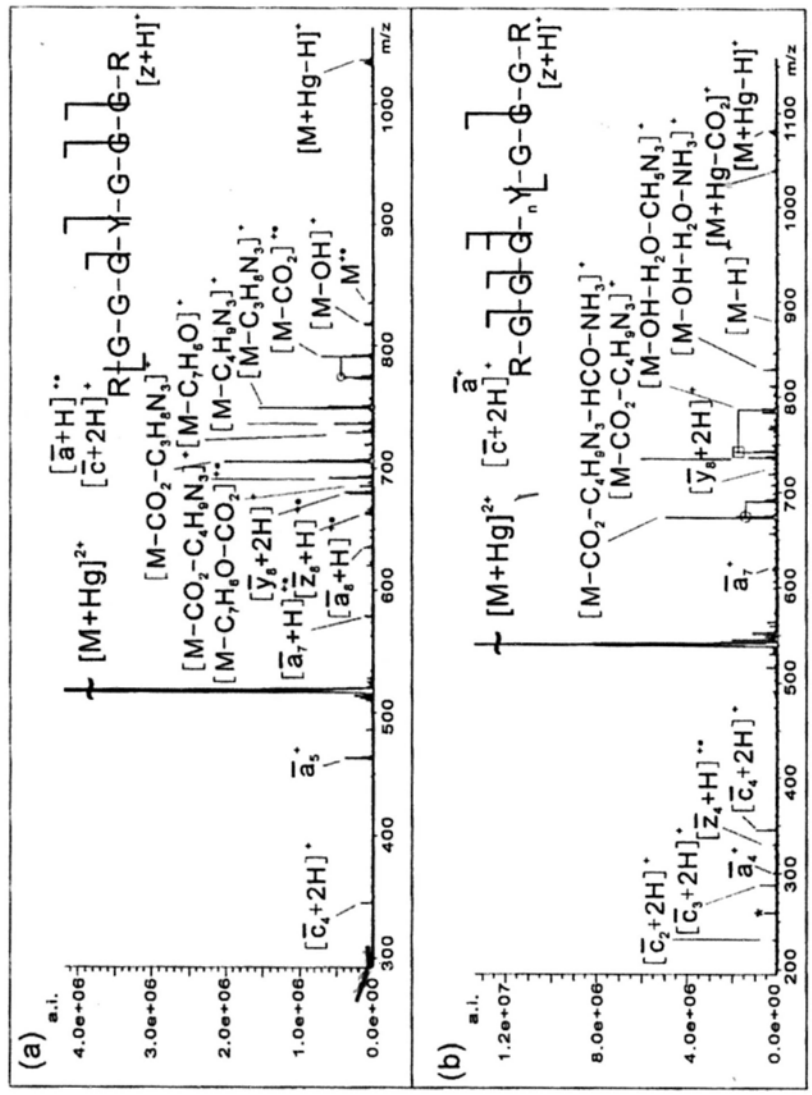

Figure 5.11 ECD spectra of Hg^{2+} adducted RGGGYGGGR and RGGGnYGGGR

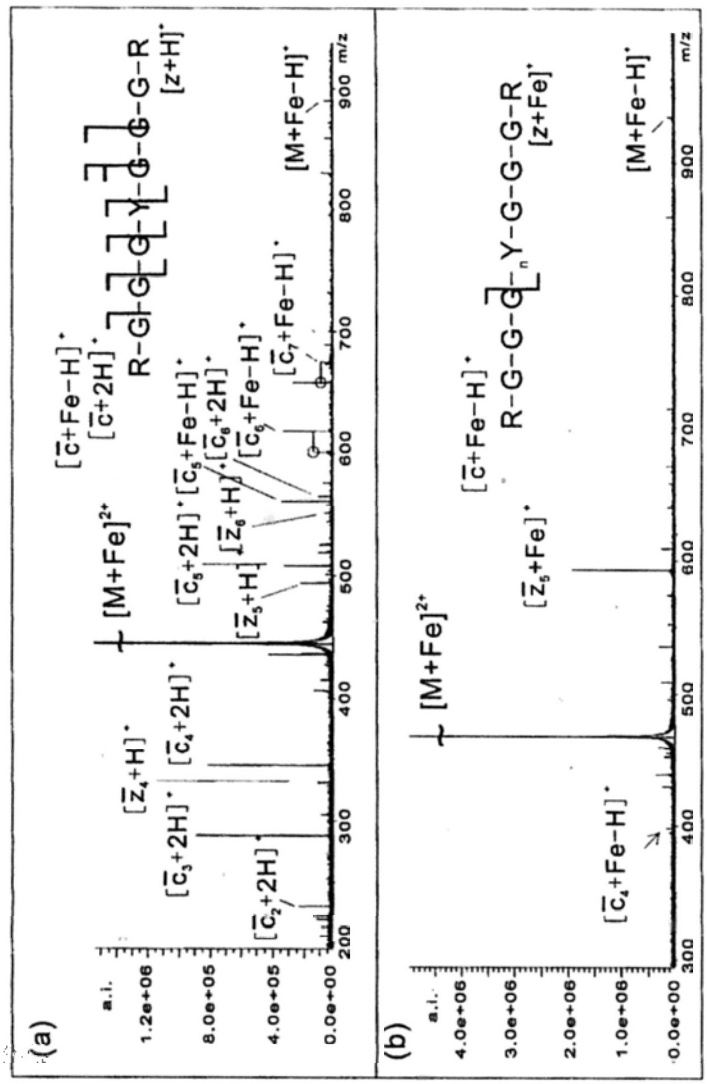

Figure 5.12 ECD spectra of Fe^{2+} adducted RGGGYGGGR and RGGGnYGGGR

Figure 5.9 shows the ECD of protonated peptides RGGGYGGGR before and after nitration. Similar to the SERCA peptides, the typical ECD fragment ions were generated in the protonated peptides without nitration; whereas few ECD fragment ions were formed in the ECD spectrum of the nitrated tyrosine containing peptides. Figure 5.10 shows the ECD spectra of Cu^{2+} adducted analogues. In contrast to the protonated analogues, the ECD spectra of Cu^{2+} adducted model peptides (RGGGYGGGR and $RGGG_nYGGGR$) show similar features. Series of metalated *b*-/*y*-type fragment ions were generated and the nitration site of the peptide could be localized. It seems that nitration of tyrosine has no significant effect on the ECD fragmentation of Cu^{2+} adducted peptides. Figure 5.11 shows the ECD spectra of Hg^{2+} adducted RGGGYGGGR before and after tyrosine nitration. Similar to the ECD fragmentation of Hg^{2+} adducted RGGGWGGGR, peptide radical cation $M^{+\bullet}$ and fragment ions derived from neutral losses of $M^{+\bullet}$ including $[C_7H_6O]$ (Y) and $[C_4H_9N_3]$ (R) dominated the ECD spectrum of Hg^{2+} adducted RGGGYGGGR. The ECD spectrum of Hg^{2+} adducted tyrosine nitrated peptide ($RGGG_nYGGGR$) showed some differences. No species corresponding to nitrated tyrosine side chain loss was observed. The fragment ions are dominated by neutral losses from the arginine side chain in conjunction with CO_2 loss. Figure 5.12 shows the ECD spectra of Fe^{2+} adducted RGGGYGGGR before and after tyrosine nitration. For the peptide without nitration, typical ECD fragment ions, including protonated *c*-/*z*-type fragment ions and metalated *c*-ions were observed. After tyrosine nitration, almost all typical ECD fragment ions, especially the non-metalated fragment ions, were inhibited. A metalated ion, tentatively attributed as $[\bar{z}_5+Fe]^+$, was observed with high abundance. The formation of this ion might be caused by some specific interactions between Fe^{2+} and the nitrated tyrosine side chain. Further investigation is needed to verify this hypothesis.

In summary, ECD of metal ion (except Cu^{2+}) adducted nitrated tyrosine containing

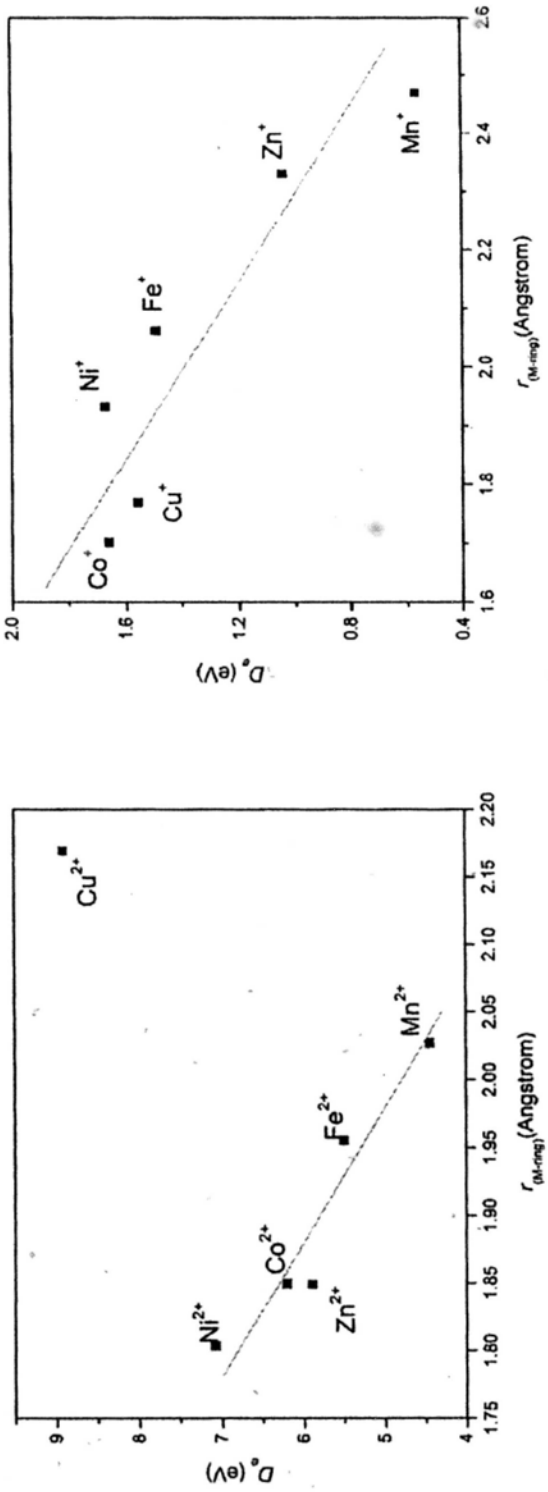

Figure 5.13 Correlation between the metal ring distance and the binding energy of the metal cation-nitrated phenol complexes

Table 5.2 Geometries and binding energies of M^{2+}-NP complexes in the cation-π coordination model calculated at the B3LYP/6-31++G(d,p)/6-311+G(d) level of theory.

	$M^{2+/+}$ (spin multiplicities in parentheses)											
	Mn (6/7)		Fe (5/4)		Co (4/3)		Ni (3/2)		Cu (2/1)		Zn (1/2)	
r(M-ring)[a]/Å	2.027	2.470	1.956	1.770	1.850	1.702	1.804	1.932	2.169	2.062	1.849	2.331
r(C-N)[b]/Å	1.496	1.472	1.497	1.473	1.500	1.473	1.501	1.465	1.488	1.464	1.500	1.469
∠M-C[c]-N/°	59.2	65.8	60.5	52.6	54.8	51.7	54.2	71.4	96.5	68.5	55.0	80.1
D_e/eV	4.44	0.56	5.50	1.56	6.21	1.66	7.08	1.67	8.91	1.49	5.90	1.04

[a] Distance between the metal atom and C_6 plane.

[b] Distance of C-NO_2 bond.

[c] The carbon atom in line with the C-NO_2 bond of the C_6 plane.

Table 5.3 Geometries and binding energies of M^{2+}-NP complexes in the cation-nitro group coordination model calculated at the B3LYP/6-31++G(d,p)/6-311+G(d) level of theory.

	$M^{2+/+}$ (spin multiplicities in parentheses)											
	Mn (6/7)		Fe (5/4)		Co (4/3)		Ni (3/2)		Cu (2/1)		Zn (1/2)	
$r(M\text{-}O^1)^a$/Å	2.071	2.317	2.032	2.166	1.984	2.048	1.954	2.067	2.996	2.307	1.999	2.375
$r(M\text{-}O^2)^b$ /Å	2.024	2.251	1.979	2.138	1.935	2.032	1.929	2.041	2.008	2.046	1.963	2.160
$r(C\text{-}N)^c$ /Å	1.335	1.376	1.336	1.378	1.329	1.377	1.328	1.378	1.443	1.383	1.333	1.380
D_e/eV	6.43	1.59	7.26	2.12	7.74	2.12	8.29	2.47	10.50	2.14	7.79	1.85

[a] Distance between the metal atom and the nitro oxygen hydrogen bonded with hydroxyl hydrogen.

[b] Distance between the metal atom and the other nitro oxygen.

[c] Distance of C-NO_2 bond.

peptides generated some unique fragment ions as compared to the unmodified peptide. Further experimental study of the effect of other metal ion adduction on the ECD fragmentation of nitrated tyrosine containing peptides should be conducted.

5.3.4 Interaction of nitrated phenol with metal ions: model of nitrated tyrosine binding

Interactions of transition metal ions with amino acids residues/peptides have been a subject of interest in recent years [184,185]. An extension of this research involves the study of the effect of chemical modifications on the interaction of metal ions with the biomolecules. For example, does the nitro (NO_2) group on the tyrosine side chain affect the binding mode of metal ion-peptide complexes? In this section, the binding of nitrated phenol (NP) with first row transition metal ions was investigated using the DFT method. Nitrated phenol was used as a simple model for probing the binding of metal ions to nitrated tyrosine. As shown in Scheme 5.2, two kinds of coordination, including the cation-π coordination and cation-nitro coordination were considered.

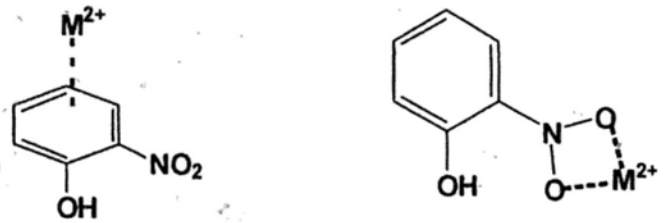

Scheme 5.2

Tables 5.2 and 5.3 show the results of geometry optimization of metal ion-NP complexes. The exothermicity of binding (binding energy) is defined as:

$$D_e = E(M^{+/2+}) + E(NP) - E(M^{+/2+}NP) \quad (5.1)$$

For Fe^+, although the ground state of the metal ions is sextet ($3d^64s^1$), previous studies indicated that the quartet ($3d^7$) state metal complexes were more stable than that of sextet state [147]. Therefore, only the quartet state metal complexes were calculated

here. Figure 5.13 (a, b) show the correlation between the metal ring distance and the binding energy of the cation-π coordination complexes. The odd behavior of binding energy for Cu^{2+}-NP complex may be caused by the oxidation of the NP by Cu^{2+}. NBO analysis shows that the charge on metal were 0.99 and 0.96 for the cation-π and cation-nitro coordination mode, respectively, which indicated that the Cu^{2+} was reduced to Cu^{+}.

As shown in the tables, the binding energies of the cation-nitro coordination are generally larger than that of cation-π coordination. It indicates that the metal ions favor coordinating with the nitro group of the nitrated tyrosine rather than the aromatic ring. Occupation of the nitro group by metal ions would alter the electronic properties as well as the hydrogen affinity of the nitrated tyrosine residue in the peptides and thus change the ECD fragmentation.

5.4 Conclusion

In this chapter, the effect of tyrosine nitration on the ECD of peptides was investigated. It was found that single nitration of tyrosine residue suppresses the ECD fragmentation of doubly, triply and quadruply protonated peptides. Directly scan of the N-O and N-C_α bond of the truncated peptides using the DFT method indicated that the $OH^{\bullet}$ radical lost from the hydrogen adducted nitro group is energetically more feasible than traditional ECD channel. Based on the calculation, after $OH^{\bullet}$ lost, the nitroso (NO) group adducted tyrosine could form a subsequent hot hydrogen trap and suppress the ECD fragmentation of peptides of higher charge state.

The possible use of metal ions, rather than the proton as charge carrier in the ECD of peptides for nitrated tyrosine localization, was also investigated. By comparing the behavior of metalated model peptides with and without tyrosine nitration, it was found that the fragmentations of Cu^{2+} adducted peptides with and without nitration are similar to each other. As a result, the site of tyrosine nitration could be localized. The typical

ECD fragments observed in the Fe^{2+} adducted normal peptide were substituted by a high abundance metalated *z*-ion. The dramatically changes were tentatively attributed to the coordination between Fe^{2+} and the nitrated tyrosine residue, but further investigation is required.

In addition, the interactions of nitrated phenol with first row transition metal ions as a model of metal ions-nitrated tyrosine were theoretically investigated. By comparing the cation-π coordination and cation-nitro group coordination, it was found that the cation-nitro coordinated complexes were generally more stable for all the metal ions studied.

Chapter 6

Conclusions

The effect of transition metal ions as charge carriers in the ECD of peptides were investigated in this thesis. The ECD behavior of model peptides cationized with different divalent transition metal ions were examined and compared with that of protonated analogues with different basic amino acid residue (R, K and H) as proton carriers. Based on the ECD fragmentation of peptides adducted by first row divalent transition metal ions, it is proposed that the electronic configurations of the metal ions govern the ECD behavior of the metalated peptides. The two competitive channels observed are electron captured by peptide and electron captured metal ion are. For Mn^{2+} ($3d^5$) and Zn^{2+} ($3d^{10}$), which posses half-fully and fully filled d shells, it is believed that the usual ECD fragmentation behavior of metalated peptides was caused by electron-proton recombination. For the other metal ions, including Fe^{2+} ($3d^6$), Co^{2+} ($3d^7$), Ni^{2+} ($3d^8$), and Cu^{2+} ($3d^9$), with partially filled d shells, the formation of usual "slow-heating" type of fragment ions was believed to be caused by energy transfer after electron-metal ion recombination.

To further investigate the effect of transition metal ions with the same electronic configuration, ECD spectra of model peptides adducted with Group IIB metal ions (Zn^{2+}, Cd^{2+} and Hg^{2+}) as charge carrier were compared. Typical ECD fragment ions, mainly including *c*-/*z*-type fragments were observed in the ECD of peptides adducted with Zn^{2+}. Peptide radical cations $M^{+\bullet}$ and related fragment species were observed in the ECD of model peptides adducted with Cd^{2+} or Hg^{2+}. Based on these distinctive reaction products, a new model coined "electron capture induced spontaneous electron transfer" was proposed to account for the experimental observations. It is believed that

the relative proportion of electron-proton recombination and metal-ion reduction processes depends on factors arising from kinetics (i.e. the number density of the zwitterionic form of the precursor ions) and/or thermodynamics (i.e. the solvation-modulated electron-metal ion recombination energy). Regardless of the controlling factor, the reduction of divalent metal ions by the electron capture event could induce spontaneous electron transfer from the peptide moiety to the monovalent metal centre and generate hydrogen-deficient $M^{+\bullet}$ species. Depending on the overall reaction exothermicity, the $M^{+\bullet}$ species might be formed with large internal energy and undergo further decomposition to give structural specific information.

As an extension of normal model peptides, ECD of protonated nitrated tyrosine containing peptides with different charge states and peptides cationized with transition metal ions were investigated. The ECD fragmentations of metalated model peptides with and without tyrosine nitration were compared. It was found that some fragment ions that were inhibited in the ECD of protonated peptides were liberated in the ECD of metalated peptides. In addition to the experimental study, the interactions of nitrated phenol with first row transition metal ions as a model of metal ions-nitrated tyrosine were theoretically investigated. By comparing the cation-π coordination and cation-nitro group coordination, it was found that the cation-nitro coordinated complexes were generally more stable for all the metal ions studied.

Further experimental and theoretical investigations into the effect of metal ions adduction, such as other metal ion and larger model peptides, on the ECD fragmentation and structures of metalated peptides should be conducted.

References

1. Lijas, A. *Science.* 1999; **285**: 2077.
2. Metzger, J. W. *Angew. Chem. Int. Ed.* 1994; **33**: 723.
3. Gevaert, K.; Vandekerckhove, J. *Electrophoresis.* 2000; **21**: 1145.
4. Aebersold, R.; Goodlett, D. R. *Chem. Rev.* 2001; **101**: 269.
5. Patterson, S. D.; Aebersold, R. H. *Nat. Genet.* 2003; **33**: 311.
6. Edman, P. *Acta. Chem. Scand.* 1950; **4**: 283.
7. Katsuki, S.; Scott, J. E.; Yamashin, I. *Biochem. J.* 1965; **97**: C25.
8. Hunkapiller, T.; Tempst, P.; Hood, L. *Nature.* 1984; **310**: 105.
9. Aebersold, R.; Mann, M. *Nature.* 2003; **422**: 198-207.
10. Geisow, M. J. *Nat. Biotechnol.* 1998; **16**: 206.
11. Persidis, A. *Nat. Biotechnol.* 1998; **16**: 393.
12. Chu, D. S.; Liu, H.; Nix, P.; Wu, T. F.; Ralston, E. J.; Yates, J. R. *Nature.* 2006; **443**: 101.
13. Miranker, A.; Edmonds, C. G.; Smith, R. D. *Science.* 1990; **248**: 201.
14. Domon, B.; Aebersold, R. *Science.* 2006; **312**: 212.
15. Garcia, B. A. *J. Am. Soc. Mass Spectrom* 2010; **21**:193.
16. Kelleher, N. L. *Anal Chem* 2004; **76**: 197.
17. McLafferty, F. W.; Breuker, K.; Jin, M.; Han, X.; Infusini, G.; Jiang, H.; Kong, X.; Begley, T. P. *FEBS J.* 2007; **274**: 6256.
18. Siuti, N.; Kelleher, N. L. *Nat. Methods.* 2007; **4**: 817.
19. Yergey, J. A.; Cotter, R. J.; Heller, D.; Fenselau, C. *Anal. Chem.* 1984; **56**: 2262.
20. Hunt, D.F.; Henderson, R. A.; Shabanowitz, J.; Sakaguchi, K.; Michel, H.; Sevilir, N.; Cox, A. L.; Appella, E. Engelhard, V. H. *Science* 1992; **255**: 1261.
21. James, P.; Quadroni, M.; Carafoli, E.; Fonnet, G. *Biochem, Biophys. Res. Commun.* 1993; **195**: 58.
22. VerBerkmoes, N. C.; Bundy, J. L.; Hauser, L.; Asano, K. G.; Razumovskaya, J.; Larimer, F.; Hettich, R. L.; Stephenson, J. L. *J. Proteome Res.* 2002; **1**: 239.

23. Pandey, A.; Mann, M. *Nature* 2000; **405**: 837.

24. Bleakney, W. *Phys. Rev.* 1929; **34**: 157.

25. Munson, S. B.; Field, F. H. *J. Am. Chem. Soc.* 1966; **88**: 2621.

26. Barber, M.; Bordoli, R. S.; Sedgwick, R. D.; Tyler, A. N. *Nature* 1981; **293**: 270.

27. Beckey, H. D. *Principles of Field Ionization and Field Desorption Mass Spectrometry.* Pergamon: Oxford, England, 1977.

28. Macfarlane, R. D.; Torgerson, D. F. *Science* 1976; **191**: 920.

29. Reiter, J. A.; Zhao, H. *J. Am. Chem. Soc.* 1994; **116**: 7827.

30. Karas, M.; Bachmann, D.; Bahr, U.; Hillenkamp, F. *Int. J. Mass Spectrom. Ion Processes* 1987; **78**: 53.

31. Yamashita, M.; Fenn, J. B. *J. Phys. Chem.* 1984; **88**: 4451.

32. Fenn, J. B.; Mann, M.; Meng, C. K.; Wong, S. F. Whitehouse, C. M. *Science* 1989; **246**: 64.

33. Trimpin, S.; Inutan, E. D.; Herath, T. N.; McEwen, C. N. *Anal. Chem*; 2010; **82**: 11.

34. Dole, M.; Mack, L. L.; Hines, R. L. *J. Chem. Phys.* 1968; **49**: 2240.

35. Iribarne, J. V.; Thomson, B. A. *J. Chem. Phys.* 1976; **64**: 2287.

36. Roepstorff, P.; Fohlman, J. *Biomed. Mass Spectrom.* 1984; **11**: 601.

37. Johnson, R. S.; Martin, S. A.; Biemann, K.; Stults, J. T.; Watson, J. T. *Anal. Chem.* 1987; **59**: 2621.

38. Jennings, K. R. *Int. J. Mass Spectrom. Ion Phys.* 1968; **1**: 227.

39. Cody, R. B.; Frelser, B. S. *Anal. Chem.* 1982; **54**: 96.

40. Grant, E. R.; Coggiola, M. J.; Leem, Y. T.; Schulz, P. A.; Sudbo, A. S.; Shen, Y. R. *Chem. Phys. Lett.* 1977; **52**: 595.

41. Price, W. D.; Schnier, P. D.; Williams, E. R. *Anal. Chem.* 1996; **68**: 859.

42. Mabud, D. A.; Dekrey, M. J.; Cooks, R. G. *Int. J. Mass Spectrom. Ion Processes* 1985; **67**: 285.

43. Hunter, A. P.; Games, D. E. *Rapid Commun. Mass Spectrom.* 1994; **8**: 559.

44. Gu, C.; Tsaprailis, G; Breci, L.; Wysocki, V. H. *Anal. Chem.* 2000; **72**:5804.

45. Boering, K. A.; Rolfe, J.; Brauman, J. I. *Rapid Commun. Mass Spectrom.* 1992; **6**:303.

46. Gauthier, J. W.; Trautman, T. R.; Jacobson, D. B. *Anal. Chim. Acta* 1991; **246**: 211.

47. Vaisar, T.; Urban, J. *J. Mass Spectrom.* 1998; **33**: 505.

48. Summerfield, S. G.; Bolgar, M. S.; Gaskell, S. J. *J. Mass Spectrom.* 1997; **32**: 225.

49. Cordero, M. M.; Houser, J. J.; Wesdemiotis, C. *Anal. Chem.* 1993; **65**: 1594.

50. Nold, M. J.; Wesdemiotis, C.; Yalcin, T.; Harrison, A. G. *Int. J. Mass Spectrom. Ion Proc.* 1997; **164**: 137.

51. Eckart, K.; Holthausen, M. C.; Koch, W.; Spiess, J. *J. Am. Soc. Mass Spectrom.* 1998; **9**: 1002.

52. Yalcin, T.; Khouw, C.; Csizmadia, I. G.; Peterson, M. R.; Harrison, A. G. *J. Am. Soc. Mass Spectrom.* 1995; **6**: 1165.

53. Paizs, B.; Lendvay, G.; Vekey. K.; Suhai, S. *Rapid Commun. Mass Spectrom.* 1999; **13**: 525.

54. Farrugia, J. M.; O'Hair, R. A. J.; Reid, G. E. *Int. J. Mass Spectrom.* 2001; **210/211**: 71.

55. Rodriquez, C.F.; Cunje, A.; Shoeib, T.; Chu, I. K.; Hopkinson, A. C.; Siu, K. W. M. *J. Am.Chem. Soc.* 2001; **123**: 3006.

56. Vath, J. E.; Biemann, K. *Int. J. Mass Spectrom. Ion Proc.* 1990; **100**: 287.

57. Laskin, J.; Futrell, J. H. *J. Am. Soc. Mass Spectrom.* 1996; **14**: 1340.

58. Zubarev, R. A.; Kelleher, N. L.; McLafferty, F. W. *J. Am. Chem. Soc.* 1998; **120**: 3265.

59. Syka, J. E. P.; Coon, J. J.; Schroeder, M. J.; Shabanowitz, J.; Hunt, D. F. *Proc. Natl. Acad. Sci. U. S. A.* 2004; **101**: 9528.

60. Gord, J. R.; Horning, S. R.; Wood, J. M.; Cooks, R. G.; Freiser, B. S., *J. Am. Soc. Mass Spectrom.* 1993; **4**: 145.

61. Budnik, B. A.; Haselmann, K. F.; Elkin, Y. N.; Gorbach, V. I.; Zubarev, R. A., *Anal. Chem.* 2003; **75**: 5994.

62. Budnik, B. A.; Haselmann, K. F.; Zubarev, R. A., *Chem. Phys. Lett.* 2001; **342**: 299.

63. Ly, T.; Julian, R. *Angew. Chem. Int. Ed.* 2009; **48**: 7130.

64. Cooper, H. J.; Håkansson, K.; Marshall, A. G. *Mass Spectrom. Rev.* 2005; **24**: 201.

65. Kelleher, R. L.; Zubarev, R. A.; Bush, K.; Furie, B.; Furie, B. C.; McLafferty, F. W.; Walsh, C. T. *Anal. Chem.* 1999; **71**: 4250.

66. Stensballe, A.; Jensen, O. N.; Olsen, J. V.; Haselmann, K. F.; Zubarev, R. A. *Rapid*

Commun. Mass Spectrom. 2000; **14**: 1793.

67. Shi, S. D. H.; Hemling, M. E.; Carr, S. A.; Horn, D. M.; Lindh, I.; McLafferty, F. W. *Anal. Chem.* 2001; **73**: 19.
68. Hakansson, K.; Cooper, H. J.; Emmett, M. R.; Costello, C. E.; Marshall, A. G.; Nilsson, C. L. *Anal. Chem.* 2001; **73**: 4530.
69. Mirgorodskaya, E.; Roepstorff, P.; Zubarev, R. A. *Anal. Chem.* 1999; **71**: 4431.
70. Guan, Z. Q. *J. Am. Soc. Mass Spectrom.* 2002; **13**: 1443.
71. Oh, H.; Breuker, K.; Sze, S. K.; Ge, Y.; Carpenter, B. K.; McLafferty, F. W. *Proc. Natl. Acad. Sci. U.S.A.* 2002; **99**: 15863.
72. Yang, J.; Håkansson, K. *J. Am. Soc. Mass Spectrom.* 2006; **17**: 1369.
73. Kaczorowska, M. A.; Cooper, H. J. *J. Am. Soc. Mass Spectrom.* 2008; **19**: 1312.
74. Koster, S.; Duursma, M. C.; Boon, J. J.; Heeren, R. M. A.; Ingemann, S.; van Benthem, R. A. T. M.; de Koster, C. G. *J. Am. Soc. Mass Spectrom.* 2003; **14**: 332.
75. Olsen, J. V.; Haselmann, K. F.; Nielsen, M. L.; Budnik, B. A.; Nielsen, P. E.; Zubarev, R. A. *Rapid Commun. Mass Spectrom.* 2001; **15**: 969.
76. Cerda, B. A.; Breuker, K.; Horn, D. M.; McLafferty, F. W. *J. Am. Soc. Mass Spectrom.* 2001; **12**: 565.
77. Zubarev, R. A.; Kruger, N. A.; Fridriksson, E. K.; Lewis, M. A.; Horn, D. M.; Carpenter, B. K.; McLafferty, F. W. *J. Am. Chem. Soc.* 1999; **121**: 2857.
78. Sawicka, A.; Skurski, P.; Hudgins, R. R.; Simons, J. *J. Phys. Chem. B.* 2003; **107**: 13505.
79. Sobczyk, M.; Anusiewicz, W.; Berdys-Kochanska, J.; Sawicka, A.; Skurski, P.; Simons, J. *J. Phys. Chem. A.* 2005; **109**: 250.
80. Sobczyk, M.; Simons, J. *J. Phys. Chem. B.* 2006; **110**: 7519.
81. Syrstad, E. A.; Turecek, F. *J. Am. Soc. Mass Spectrom.* 2005; **16**: 208.
82. Jones, J. W.; Sasaki, T.; Goodlett, D. R.; Turecek, F. *J. Am. Soc. Mass Spectrom.* 2007; **18**: 432.
83. Turecek, F.; Chen, X. H.; Hao, C. T. *J. Am. Chem. Soc.* 2008; **130**: 8818.
84. Licinci, G.; Scrimin, P. *Angew. Chem. Int. Ed.* 2003; **42**: 4572.
85. Pyle, A. M. *Science* 1993; **261**: 709.
86. Holm, R. H.; Kennepohl, P.; Solomon, E. I. *Chem. Rev.* 1996; **96**: 2239.

87. Case, M. A.; McLendon, G. L. *Acc. Chem. Res.* 2004; **37**: 754.

88. Riordan, J. F.; Vallee, L., Eds. Academic: San Diego, CA, 1993; 227.

89. Bertini, I.; Turano, P.; Villa, A. *Chem. Rev.* 1993; **93**: 2833.

90. Vallee, B. L.; Auld, D. S. *Proc. Natl. Acad. Sci. USA.* 1990; **87**: 220.

91. Lei, Q. P.; Amster, I. J. *J. Am. Soc. Mass Spectrom.* 1996; **7**: 722.

92. Newton, K. A.; McLuckey, S. A. *J. Am. Chem. Soc.* 2003, **125**: 12404.

93. Michelle, M. K.; Chrys, W. *Int. J. Mass Spectrom.* 2003; **227**: 191.

94. Adams, J.; Gross, M. L. *J. Am. Chem. Soc.* 1986, **108**: 6915.

95. Cancilla, M. T.; Penn, S. G.; Carroll, J. A.; Lebrilla, C. B. *J. Am. Chem. Soc.* 1996, **118**: 6736.

96. Liu, D. F.; Seuthe, A. B.; Ehrler, O. T.; Zhang, X. H.; Wyttenbach, T.; Hsu, J. F.; Bowers, M. T. *J. Am. Chem. Soc.* 2005; **127**: 2024.

97. Sheldon, M. W.; Jennifer, S. B. *J. Am. Soc. Mass Spectrom.* 2004; **15**: 1039.

98. Teesch, L. M.; Adams, J. *J. Am. Chem. Soc.* 1991; **113**: 812.

99. Kim, H. I.; Beauchamp, J. L. *J. Am. Chem. Soc.* 2008; **130**: 1245.

100. Lioe, H.; Duan, M.; O'Hair, R. A. J. *Rapid Commun. Mass Spetrom.* 2007; **21**: 2727.

101. Turecek, F. *Mass Spectrom Rev.* 2007; **26**: 563.

102. Chu, I. K.; Rodriquez, C. F.; Lau, T. C.; Hopkinson, A. C.; Siu, K. W. M. *J Phys Chem B.* 2000; **104**: 3393.

103. Lam, C. N. W.; Siu, S. O.; Orlova, G.; Chu, I. K. *Rapid Commun Mass Spectrom.* 2005; **20**: 790.

104. Hopkinson, A. C. *Mass Spectrom Rev.* 2009; **28**: 655.

105. Barlow, C. K.; McFadyen, W. D.; O'Hair, R. A. J. *J Am Chem Soc* 2005; **127**: 6109.

106. Comisarow, M. B.; Marshall, A. G. *Chem. Phys. Lett.* 1974; **25**: 282.

107. Marshall, A. G.; Hendrickson, C.; Jackson, G. S. *Mass Spectrom Rev.* 1998; **17**: 1.

108. Marshall, A. G.; Grosshans, P. B. *Anal. Chem.* 1991; **63**: A215.

109. Caravatti, P.; Allemann, M. *Org. Mass Spectrom.* 1991; **26**: 514.

110. Frisch, M. J.; Trucks, G. W.; Schlegel, H. B.; Scuseria, G. E.; Robb, M. A.; Cheeseman, J. R.; Montgomery, J. A.; Jr. Vreven, T.; Kudin, K. N.; Burant, J. C.;

Millam, J. M.; Iyengar, S. S.; Tomasi, J.; Barone, V.; Mennucci, B.; Cossi, M.; Scalmani, G.; Rega, N.; Petersson, G. A.; Nakatsuji, H.; Hada, M.; Ehara, M.; Toyota, K.; Fukuda, R.; Hasegawa, J.; Ishida, M.; Nakajima, T.; Honda, Y.; Kitao, O.; Nakai, H.; Klene, M.; Li, X.; Knox, J. E.; Hratchian, H. P.; Cross, J. B.; Adamo, C.; Jaramillo, J.; Gomperts, R.; Stratmann, R. E.; Yazyev, O.; Austin, A. J.; Cammi, R.; Pomelli, C.; Ochterski, J. W.; Ayala, P. Y.; Morokuma, K.; Voth, G. A.; Salvador, P.; Dannenberg, J. J.; Zakrzewski, V. G.; Dapprich, S.; Daniels, A. D.; Strain, M. C.; Farkas, O.; Malick, D. K.; Rabuck, A. D.; Raghavachari, K.; Foresman, J. B.; Ortiz, J. V.; Cui, Q.; Baboul, A. G.; Clifford, S.; Cioslowski, J.; Stefanov, B. B.; Liu, G.; Liashenko, A.; Piskorz, P.; Komaromi, I.; Martin, R. L.; Fox, D. J.; Keith, T.; Al-Laham, M. A.; Peng, C. Y.; Nanayakkara, A.; Challacombe, M.; Gill, P. M. W.; Johnson, B.; Chen, W.; Wong, M. W.; Gonzalez, C.; Pople, J. A. *Gaussian 03, Revision D.01*, Gaussian, Inc., Wallingford CT, 2004.

111. Becke, A. D. *J. Chem. Phys.* 1993; **98**: 5648.

112. Becke, A. D. *J. Chem. Phys.* 1993; **98**: 1372.

113. Stephens, P. J.; Delvin, F. J.; Cabalowski, C. F.; Fisch, M. J. *J. Phys. Chem.* 1994; **98**: 11623.

114. Hay, P. J.; Wadt, W. R. *J. Chem. Phys.* 1985; **82**: 299.

115. Hay, P. J.; Wadt, W. R. *J. Chem. Phys.* 1985; **82**: 270.

116. Saunders, M.; Houk, K. N.; Wu, Y. D.; Still, W. C.; Lipton, M.; Chang, G.; Guida, W. C. *J. Am. Chem. Soc.* 1990; **112**: 1419.

117. Zubarev, R. A.; Haselmann, K. F.; Budnik, B.; Kjeldsen, F.; Jensen, F. *Eur. J. Mass Spectrom.* 2002; **8**: 337.

118. Fung, Y. M. E.; Adams, C. M.; Zubarev, R. A. *J. Am. Chem. Soc.* 2009; **131**: 9977.

119. Chan, W. Y. K.; Chan T. W. D. *J. Am. Soc. Mass Spectrom.* 2010; **21**: 1235.

120. Creese, A. J.; Cooper, H. J. *J. Am. Soc. Mass Spectrom.* 2008; **19**: 1263.

121. Jones, A. W.; Mikhailov, V. A.; Iniesta, J.; Cooper, H. J. *J. Am. Soc. Mass Spectrom.* 2010; **21**: 268.

122. Tsybin, Y. O.; Håkansson, P.; Budnik, B. A.; Haselmann, K. F.; Kjeldsen, F.; Gorshkov, M.; Zubarev, R. A. *Rapid Commun. Mass Spectrom.* 2001; **15**: 1849.

123. Tsybin, Y. O.; Quinn, J. P.; Tsybin, O. Y.; Hendrickson, C. L.; Marshall, A. G. *J. Am.*

Soc. Mass Spectrom. 2008; **19**: 762.

124. Tsybin, Y. O.; Witt, M.; Baykut, G.; Håkansson, P. *Rapid Commun. Mass Spectrom.* 2004; **18**: 1607.

125. Gorshkov, M. V.; Masselon, C. D.; Nikolaev, E. N.; Udseth, H. R.; Pasa-Tolic, L.; Smith, R. D. *Int. J. Mass Spectrom.* 2004; **234**: 131.

126. Horn, D. M.; Ge, Y.; McLafferty F. W. *Anal. Chem.* 2000; **72**: 4778.

127. Håkansson, K.; Chalmers, M. J.; Quinn, J. P.; McFarland, M. A.; Hendrickson, C. L.; Marshall, A. G. *Anal. Chem.* 2003; **75**: 3256.

128. Iavarone, A. T.; Paech, K.; Williams, E. R. *Anal. Chem.* 2004; **76**: 2231.

129. Eller, K.; Schwarz, H. *Chem. Rev.* 1991; **91**: 1121.

130. Kleinnijenhuis, A. J.; Mihalca, R.; Heeren, R. M. A.; Heck, A. J. R. *Int. J. Mass Spectrom.* 2006; **253**: 217.

131. Fung, Y. M. E.; Liu, H.; Chan, T. W. D. *J. Am. Soc. Mass Spectrom.* 2006; **17**: 757.

132. Liu, H. C.; Håkansson, K. *J. Am. Soc. Mass Spectrom.* 2006; **17**: 1731.

133. Liu, H. C.; Håkansson, K. *Anal. Chem.* 2006; **78**: 7570.

134. Liu, H. C.; Yoo, H. J.; Håkansson, K.; Lee, J. Y.; Sherman, D. H. *J. Am. Soc. Mass Spectrom.* 2007; **18**: 842.

135. Adamson, J. T.; Håkansson, K. *Anal. Chem.* 2006; **79**: 2901.

136. Liu, H. C.; Yoo, H. J.; Håkansson, K. *J. Am. Soc. Mass Spectrom.* 2008; **19**: 799.

137. Burgt, Y. E. V.; Palmblad, M.; Dallebout, H.; Heeren, R. M. A. *Rapid Commun. Mass Spectrom.* 2009; **23**: 31.

138. Turecek, F.; Jones, J. W.; Holm, A. I. S.; Panja, S.; Nielsen, S. B.; Hvelplund, P. *J. Mass. Spectrom.* 2009; **44**: 707.

139. Turecek, F.; Jones, J. W.; Holm, A. I. S.; Panja, S.; Nielsen, S. B.; Hvelplund, P. *J. Mass. Spectrom.* 2009; **44**: 1518.

140. Feketeová, L.; Ryzhov, V.; O'Hair, R. A. J. *Rapid Commun. Mass Spectrom.* 2009; **23**: 3133.

141. Chan, T. W. D.; Duan, L.; Sze, T. P. *Anal. Chem.* 2002; **74**: 5282.

142. Sovago, I.; Osz, K. *Dalton Trans.* 2006; 3841.

143. Sigel, H.; Martin, R. B. *Chem. Rev.* 1982; **82**: 385.

144. Rulisek, L.; Vondrasek, J. *J. Inorg. Biochem.* 1998; **71**:115.

145. Wong, C. K. L.; Chan, T. W. D. *Rapid Commun. Mass Spectrom.* 1997; **11**: 513.

146. Armentrout, P. B. *Annu. Rev. Phys. Chem.* 1990; **41**: 313.

147. Schröder, D.; Shaik, S.; Schwarz, H. Acc. Chem. Res. 2000; **33**: 139.

148. Schwarz, H. *Int. J. Mass Spectrom.* 2004; **237**: 75.

149. Roithova, J.; Schröder, D. *Chem. Rev.* 2010; **110**: 1170.

150. Hu, P.; Sorensen, C.; Gross, M. L. *J. Am. Soc. Mass Spectrom.* 1995; **6**: 1079.

151. Nemirovskiy, O. V.; Gross, M. L. *J. Am. Soc. Mass Spectrom.* 1996; **7**: 977.

152. Shields, S. J.; Bluhm, B. K.; Russell, D. H. *J. Am. Soc. Mass Spectrom.* 2000; **11**: 626.

153. Cerda, B. A.; Cornett, L.; Wesdemiotis, C. *Int. J. Mass Spectrom.* 1999; **193**: 205.

154. Hu, P.; Loo, J. A. *J. Am. Chem. Soc.* 1995; **117**: 11314.

155. Hu, P.; Loo, J. A.; Smith, R. D. *J. Am. Soc. Mass Spectrom.* 1994; **5**: 959.

156. X. Li; Cournoyer, J. J; C. Lin; O'Connor, P. B. *J. Am. Soc. Mass Spectrom.* 2008; **19**: 1514.

157. James, P. F.; Perugini, M. A.; O'Hair, R. A. J. *J. Am. Soc. Mass Spectrom.* 2008; **19**: 978.

158. Kaczorowska, M. A.; Hotze, A. C. G.; Hannon, M. J.; Cooper, H. J. *J. Am. Soc. Mass Spectrom.* 2010; **21**: 300.

159. Kaczorowska, M. A.; Cooper, H. J. *J. Am. Soc. Mass Spectrom.* 2009; **20**: 674.

160. Deery, M. J.; Summerfield, S. G.; Buzy, A. B.; Jennings, K. R. *J. Am. Soc. Mass Spectrom.* 1997; **8**: 253.

161. Millefiori, S.; Alparone, A.; Millefiori, A.; Vanella, A. *Biophys. Chem.* 2008; **132**: 139.

162. Wesendrup, R.; Schalley, C. A.; Schröder, D.; Schwarz, H. *Chem. – Eur. J.* 1995; **1**: 608.

163. Caraiman, D.; Koyanagi, G. K.; Bohme, D. K. *J. Phys. Chem. A.* 2004; **108**: 978.

164. Koyanagi, G. K.; Bohme, D. K. *Int. J. Mass Spectrom.* 2003; **227**: 563.

165. Zhao, X.; Flaim, E.; Huynh, L.; Jarvis, M. J. Y.; Cheng, P.; Lavrov, V. V.; Blagojevic, V.; Koyanagi, G. K.; Bohme, D. K. *Inorg. Chem.* 2006; **45**: 9646.

166. Ling, S.; Yu, W.; Huang, Z.; Lin, Z.; Haranczyk, M., Gutowski, M. *J. Phys. Chem. A.* 2006; **110**: 12282.

167. Abello, N.; Kerstjens, H. A. M.; Postma D. S.; Bischoff, R. *J. Proteome Res.* 2009; **8**: 3222.

168. Ischiropoulos, H.; Almehdi, A. B. *FEBS Lett.* 1995; **364**: 279.

169. Ischiropoulos. H. *Biochem. Biophys. Res. Commun.* 2003; **305**: 776.

170. Greenacre, S. A. B.; Ischiropoulos, H. *Free Radic. Res.* 2001; **34**: 541.

171. Turko, I.V.; Murad, F. *Pharmacol. Rev.* 2002; **54**: 619.

172. Beckman, J. S. *Chem. Res. Toxicol.* 1996; **9**: 836.

173. Beckman, J. S.; Chen, J.; Ischiropoulos, H.; Crow, J. P. *Methods Enzymol.* 1994; **233**: 229.

174. J.M. Souza, E. Daikhin, M. Yudkoff, C.S. Raman, H. Ischiropoulos, *Arch. Biochem. Biophys.* 1999; **371**: 169.

175. Sarver, A.; Scheffler, K.; Shetlar, M.; Gibson, B. W. *J. Am. Soc. Mass Spectrom.* 2001; **12**: 439.

176. Kuhn, D. M.; Sadidi, M.; Liu, X.; Kreipke, C.; Geddes, T.; Borges, C.; Watson, J. T. *J. Biol. Chem.* 2002; **277**: 14336.

177. Lee, S. J.; Lee, J. R.; Kim, Y. H.; Park, Y. S.; Park, S. I.; Park, H. S.; Kim, K. P. *Rapid Commun. Mass Spectrom.* 2007; **21**: 2797.

178. Park, S. W.; Huq, M. D.; Hu, X.; Wei, L. N. *Mol. Cell. Proteomics.* 2005; **4**: 300.

179. Tedeschi, G.; Cappelletti, G.; Negri, A.; Pagliato, L.; Maggioni, M. G.; Maci, R.; Ronchi, S. *Proteomics.* 2005; **5**: 2422.

180. Sohn, C. H.; Chung, C. K.; Yin, S.; Ramachandran, P.; Loo, J. A.; Beauchamp, J. L. *J. Am. Chem. Soc.* 2009; **131**: 5444.

181. Jones, A. W.; Mikhailov, V. A.; Iniesta, J.; Cooper, H. J. *J. Am. Soc. Mass Spectrom.* 2010; **21**: 268.

182. Mikhailov, V. A.; Iniesta, J.; Cooper, H. J. *Anal. Chem.* 2010; **82**: 7283.

183. Jones, A. W.; Cooper, H. J. *Phys. Chem. Chem. Phys.* 2010; **12**: 13394.

184. Dougherty, D. A. *Science.* 1996; **271**: 163.

185. Ryzhov, V.; Dunbar, R. C. *J. Am. Chem. Soc.* 1999; **121**: 2259.

Appendix I Pulse programs for simple MS experiment

```
;----------------------------------------------------------------
; APEX III Simple ESI Experiment
;----------------------------------------------------------------

;Experiment description
;#XS_label "Static Trapping ESI - APEX III"

;Initialization Block
;#ES_block "Initialization"
;#ES_bitmap "init3.bmp"
;#ES_conditional_pp DM bb       1u setnmr3|30       ; bit 30 hi = unmixed signal to ADC
;#ES_conditional_pp DM hires    1u setnmr3^30       ; bit 30 low = mixed signal to ADC
;#ES_conditional_pp RGAIN high  1u setnmr3^28       ; bit 28 low = Receiver gain high
;#ES_conditional_pp RGAIN low   1u setnmr3|28 ; bit 28 hi = Receiver gain low

;Start Scan Accum Block (NS loop)
;#ES_block "Start Experiment"
;#ES_bitmap "start2.bmp"
;#ES_eventtype user_delay
;#ES_parameter d0
1  ze              ; clear memory buffers in RCU
10 d0 setnmr4|7          ; turn on Ultra RF amp (AGPP_OUT[0])
                  ; NOTE: d0 must be 100ms or greater!
   10u reset:f1           ; reset phase of DDS in FCU 1

;Source Quench Block
;#ES_block "ESI Source Quench" optional
;#ES_bitmap "ESIquench1.bmp"
;#ES_eventtype quench
;#ES_parameter d3
   d3 setnmr3|24; quench the ion guide (DEFLECTION)
   1u setnmr3^24

;Cell Quench Block
;#ES_block "Cell Quench" optional
;#ES_bitmap "quench.bmp"
;#ES_eventtype quench
;#ES_parameter d4
   d4 setnmr3|27; cell quench (QUENCH)
   1u setnmr3^27

;Hexapole Accumulation Block
;#ES_block "Hexapole Accumulation"
;#ES_bitmap "hex_fill.bmp"
;#ES_eventtype user_delay
;#ES_parameter d1
   d1                    ; post quench delay

;Ionization Block
;#ES_block "Ion Generation"
;#ES_bitmap "ion_gen2.bmp"
```

```
;#ES_eventtype user_pulse
;#ES_parameter d2 d5
    d2 setnmr3|24; external ionization pulse (DEFLECTION)
    1u setnmr3^24
    d5                  ; post ionization delay

;=============================================================================
;           EXCITATION AND DETECTION
;=============================================================================

;Excitation Block
;#ES_block "Excitation"
;#ES_bitmap "excite.bmp"
;#ES_eventtype excitation_sweep
;#ES_parameter p3 pl3
    10u pl3:f1          ; set attenuation for excitation (FCU-1)

;#ES_conditional_pp EM shot      (p3 ph1 fq1):f1     ; detection excitation shot
;#ES_conditional_pp EM shot                          ;#FC_ fq1:f1 excitation_shot

;#ES_conditional_pp EM sweep 40 (p3 ph1 fq1):f1     ; detection excitation sweep
;#ES_conditional_pp EM sweep     lo to 40 times l31      ; L[31] steps in sweep
;#ES_conditional_pp EM sweep                         ;#FC_ fq1:f1 excitation_sweep

;Detection Block
;#ES_block "Detection"
;#ES_bitmap "detect.bmp"
;#ES_eventtype detection
;#ES_parameter d30
    1u setnmr4^7        ; turn off Ultra RF amp before detect (AGPP_OUT[0])
    d30                 ; receiver dead time
    go = 10 ph1         ; scan accumulation (loop to 10 times NS)

;Stop Block
;#ES_block "Exit"
;#ES_bitmap "exit.bmp"
    wr #0           ; write data to disk
    exit                ; end acquisition/experiment

; Phase program definitions for FCUs
    ph1=0 0 2 2         ; phase program: 0 0 180 180 (exc/det RF)
```

Appendix II Pulse programs for MS/MS experiments

(a) ESI-CID FT-ICR-MS Experiment

```
;----------------------------------------------------------------------
; APEX III ESI MS/MS Experiment
;----------------------------------------------------------------------

;Experiment description
;#XS_label "ESI MS/MS - APEX III"

;Initialization Block
;#ES_block "Initialization"
;#ES_bitmap "init3.bmp"
;#ES_conditional_pp DM bb      1u setnmr3|30      ; bit 30 hi = unmixed signal to ADC
;#ES_conditional_pp DM hires     1u setnmr3^30    ; bit 30 low = mixed signal to ADC
;#ES_conditional_pp RGAIN high     1u setnmr3^28     ; bit 28 low = Receiver gain high
;#ES_conditional_pp RGAIN low     1u setnmr3|28 ; bit 28 hi = Receiver gain low

;Start Scan Accum Block (NS loop)
;#ES_block "Start Experiment"
;#ES_bitmap "start2.bmp"
;#ES_eventtype user_delay
;#ES_parameter d0
1   ze              ; clear memory buffers in RCU
10 d0 setnmr4|7         ; turn on Ultra RF amp (AGPP_OUT[0])
                    ; NOTE: d0 must be 100ms or greater!
    10u reset:f1        ; reset phase of DDS in FCU 1

;Source Quench Block
;#ES_block "ESI Source Quench" optional on
;#ES_bitmap "ESIquench1.bmp"
;#ES_eventtype quench
;#ES_parameter d3
    d3 setnmr3|24; quench the ion guide (DEFLECTION)
    1u setnmr3^24

;Cell Quench Block
;#ES_block "Cell Quench" optional on
;#ES_bitmap "quench.bmp"
;#ES_eventtype quench
;#ES_parameter d4
    d4 setnmr3|27; cell quench (QUENCH)
    1u setnmr3^27

;Hexapole Accumulation Block
;#ES_block "Hexapole Accumulation"
;#ES_bitmap "hex_fill.bmp"
;#ES_eventtype user_delay
;#ES_parameter d1
    d1                  ; post quench delay

;Ionization Block
;#ES_block "Ion Generation"
;#ES_bitmap "ion_gen2.bmp"
```

```
;#ES_eventtype user_pulse
;#ES_parameter d2 d5
    d2 setnmr3|24; external ionization pulse (DEFLECTION)
    1u setnmr3^24
    d5                  ; post ionization delay

;=============================================================================
;           STAGE 1 OF EXPERIMENT
;=============================================================================

;MS/MS Selection Block
;#ES_block "Isolation (MS-2)" optional off
;#ES_bitmap "msms_sel_a.bmp"
;#ES_eventtype corr_sweep
;#ES_parameter p4 pl4
    10u pl4:f1          ; set attenuation for correlated sweep (FCU-1)
20 (p4 ph2 fq1):f1      ; correlated sweep
    lo to 20 times l0   ; L[0] steps in sweep
;#ES_flag_comment ;#FC_ fq1:f1 corr_sweep 0

;Cleanup Shots Block
;#ES_block "Isolation Shots (MS-2)" optional off
;#ES_bitmap "cl_shots.bmp"
;#ES_eventtype corr_shot
;#ES_parameter p7 pl7
    10u pl7:f1          ; set attenuation for shots (FCU-1)
30 (p7 ph2 fq1):f1      ; high resolution clean-up shots
    lo to 30 times l3   ; L[3] total shots
;#ES_flag_comment ;#FC_ fq1:f1 corr_shot 0

;Pulsed Valve Block
;#ES_block "Pulsed Valve (MS-2)" optional off
;#ES_bitmap "p_valve.bmp"
;#ES_eventtype user_pulse
;#ES_parameter d26
     d26 setnmr3|22     ; Pulsed Valve 1 (VALVE1)
     1u  setnmr3^22

;Parent Ion Activation Block
;#ES_block "Ion Activation (MS-2)" optional off
;#ES_bitmap "activate.bmp"
;#ES_eventtype ion_activation
;#ES_parameter p8 pl8
    10u pl8:f1          ; set attenuation for activation (FCU-1)
    (p8 ph2 fq1):f1     ; activation shot on the parent ion
;#ES_flag_comment ;#FC_ fq1:f1 parent_ion_activation 0

;Reaction Delay Block
;#ES_block "Pumping Delay (MS-2)" optional off
;#ES_bitmap "react_del4.bmp"
;#ES_eventtype user_delay
;#ES_parameter d6
    d6                  ; reaction delay
```

```
;=============================================================================
;              EXCITATION AND DETECTION
;=============================================================================

;Excitation Block
;#ES_block "Excitation"
;#ES_bitmap "excite.bmp"
;#ES_eventtype excitation_sweep
;#ES_parameter p3 pl3
    10u pl3:f1              ; set attenuation for excitation (FCU-1)

;#ES_conditional_pp EM shot      (p3 ph1 fq1):f1     ; detection excitation shot
;#ES_conditional_pp EM shot                          ;#FC_ fq1:f1 excitation_shot

;#ES_conditional_pp EM sweep 40 (p3 ph1 fq1):f1     ; detection excitation sweep
;#ES_conditional_pp EM sweep      lo to 40 times l31       ; L[31] steps in sweep
;#ES_conditional_pp EM sweep                         ;#FC_ fq1:f1 excitation_sweep

;Detection Block
;#ES_block "Detection"
;#ES_bitmap "detect.bmp"
;#ES_eventtype detection
;#ES_parameter d30
    1u setnmr4^7        ; turn off Ultra RF amp before detect (AGPP_OUT[0])
    d30                 ; receiver dead time
    go = 10 ph1         ; scan accumulation (loop to 10 times NS)

;Stop Block
;#ES_block "Exit"
;#ES_bitmap "exit.bmp"
    wr #0           ; write data to disk
    exit                ; end acquisition/experiment

; Phase program definitions for FCUs
    ph1=0 0 2 2         ; phase program: 0 0 180 180 (exc/det RF)
    ph2=0 0 0 0         ; phase program: 0 0 0 0 (all other RF)
```

(b) ESI-ECD FT-ICR-MS Experiment

```
;-----------------------------------------------------------------------
; APEX III ESI-ECD Experiment
;-----------------------------------------------------------------------

;Experiment description
;#XS_label ECD - APEX III"

;Initialization Block
;#ES_block "Initialization"
;#ES_bitmap "init3.bmp"
;#ES_conditional_pp DM bb      1u setnmr3|30       ; bit 30 hi = unmixed signal to ADC
;#ES_conditional_pp DM hires      1u setnmr3^30    ; bit 30 low = mixed signal to ADC
;#ES_conditional_pp RGAIN high      1u setnmr3^28      ; bit 28 low = Receiver gain high
;#ES_conditional_pp RGAIN low      1u setnmr3|28 ; bit 28 hi = Receiver gain low
```

```
;Start Scan Accum Block (NS loop)
;#ES_block "Start Experiment"
;#ES_bitmap "start2.bmp"
;#ES_eventtype user_delay
;#ES_parameter d0
1   ze              ; clear memory buffers in RCU
10 d0 setnmr4|7         ; turn on Ultra RF amp (AGPP_OUT[0])
                    ; NOTE: d0 must be 100ms or greater!
    10u reset:f1        ; reset phase of DDS in FCU 1


;Cell Quench Block
;#ES_block "Cell Quench" optional on
;#ES_bitmap "quench.bmp"
;#ES_eventtype quench
;#ES_parameter d4 d27
    d4 setnmr3|27; cell quench (QUENCH)
    1u setnmr3^27
    d27

;Source Quench Block
;#ES_block "ESI Source Quench" optional on
;#ES_bitmap "ESIquench1.bmp"
;#ES_eventtype quench
;#ES_parameter d3
    d3 setnmr3|24; quench the ion guide (DEFLECTION)
    1u setnmr3^24


;Hexapole Accumulation Block
;#ES_block "Hexapole Accumulation"
;#ES_bitmap "hex_fill.bmp"
;#ES_eventtype user_delay
;#ES_parameter d1
20 d1               ; post quench delay

;Ionization Block
;#ES_block "Ion Generation"
;#ES_bitmap "ion_gen2.bmp"
;#ES_eventtype user_pulse
;#ES_parameter d2
    d2 setnmr3|24; external ionization pulse (DEFLECTION)
    1u setnmr3^24


;=============================================================================
;           STAGE 1 OF EXPERIMENT
;=============================================================================

;MS/MS Selection Block
;#ES_block "Isolation (MS-2)" optional off
```

```
;#ES_bitmap "msms_sel_a.bmp"
;#ES_eventtype corr_sweep
;#ES_parameter p4 pl4
    10u pl4:f1          ; set attenuation for correlated sweep (FCU-1)
30 (p4 ph2 fq1):f1      ; correlated sweep
    lo to 30 times l0   ; L[0] steps in sweep
;#ES_flag_comment ;#FC_ fq1:f1 corr_sweep 0

;Cleanup Shots Block
;#ES_block "Isolation Shots (MS-2)" optional off
;#ES_bitmap "cl_shots.bmp"
;#ES_eventtype corr_shot
;#ES_parameter p7 pl7
    10u pl7:f1          ; set attenuation for shots (FCU-1)
40 (p7 ph2 fq1):f1      ; high resolution clean-up shots
    lo to 40 times l3   ; L[3] total shots
;#ES_flag_comment ;#FC_ fq1:f1 corr_shot 0

;ECD Block
;#ES_block "ECD" optional off
;#ES_bitmap "ECD.bmp"
;#ES_eventtype user_pulse
;#ES_parameter d7
  d7   setnmr3|26       ; ECD pulse (INT_GATE)
  10u setnmr3^26

;Delay Block
;#ES_block "Delay" optional off
;#ES_bitmap "ECD.bmp"
;#ES_eventtype user_pulse
;#ES_parameter d12
  d12

;=============================================================================
;              EXCITATION AND DETECTION
;=============================================================================

;Excitation Block
;#ES_block "Excitation"
;#ES_bitmap "excite.bmp"
;#ES_eventtype excitation_sweep
;#ES_parameter p3 pl3
    10u pl3:f1          ; set attenuation for excitation (FCU-1)

;#ES_conditional_pp EM shot      (p3 ph1 fq1):f1    ; detection excitation shot
;#ES_conditional_pp EM shot                         ;#FC_ fq1:f1 excitation_shot

;#ES_conditional_pp EM sweep 60 (p3 ph1 fq1):f1    ; detection excitation sweep
;#ES_conditional_pp EM sweep     lo to 60 times l31      ; L[31] steps in sweep
;#ES_conditional_pp EM sweep                        ;#FC_ fq1:f1 excitation_sweep

;Detection Block
```

```
;#ES_block "Detection"
;#ES_bitmap "detect.bmp"
;#ES_eventtype detection
;#ES_parameter d30
    1u setnmr4^7        ; turn off Ultra RF amp before detect (AGPP_OUT[0])
    d30                 ; receiver dead time
    go = 10 ph1         ; scan accumulation (loop to 10 times NS)


;Stop Block
;#ES_block "Exit"
;#ES_bitmap "exit.bmp"
    wr #0           ; write data to disk
    exit                ; end of acquisition/experiment

; Phase program definitions for FCUs
    ph1=0 0 2 2         ; phase program: 0 0 180 180 (exc/det RF)
    ph2=0 0 0 0         ; phase program: 0 0 0 0 (all other RF)
```

Appendix III Relative product ion abundances in the ECD of metalated bradykinin.